Signal Extraction and Noise Removal Methods for Multichannel Electroencephalographic Data

Hirokazu Kawaguchi

Graduate School of Engineering, Kyoto University

Acknowledgments

First of all, it is a great pleasure to express my gratitude to my supervisor Professor Tetsuo Kobayashi for his encouragement, guidance and support.

I acknowledge greatly the guidance and encouragement by Professor Yuichi Nakamura and Associate Professor Eiko Furutani. I acknowledge the useful comments and supports by Associate Professor Shoji Hamada, Dr. Takenori Oida, Dr. Jiuk Jung, Dr. Yosuke Ito, Dr. Teruyoshi Sasayama, Dr. Shiho Okuhata and Dr. Hiroaki Natsukawa. I also acknowledge the technical, spiritual supports, and friendly atmosphere by all members of the Kobayashi group, in particular Mr. Tomoaki Iida, Mr. Daisuke Izuoka and Mr. Takahiro Kume.

This work was financially supported by a Grant-in-Aid for Japan Society for the Promotion of Science (JSPS) Fellows (25-4682).

Finally I greatly thank my family for their emotional and financial supports, encouragement, and warm atmosphere.

Contents

List of Figures

List of Tables

Abbreviations

AR	autoregressive
CMS	common mode sense
DRL	driven right leg
ECD	equivalent current dipole
EEG	electroencephalogram
EMD	empirical mode decomposition
EOG	electrooculogram
EPSP	excitatory postsynaptic potential
ERD	event-related desynchronization
ERS	event-related synchronization
ERP	event-related potential
IC	independent component
ICA	independent component analysis
IMF	intrinsic mode function
IPSP	inhibitory postsynaptic potential
ITC	inter-trial coherence
KF	Kalman filter
MEMD	multivariate empirical mode decomposition
PC	principal component
PCA	principal component analysisial
SNR	signal-to-noise ratio
STFT	short time Fourier transfrom
WT	wavelet transform

Chapter 1

Introduction

I do believe that everything happens for a reason. This is my favorite quote. What do you think about this? Leibniz was one of the great thinkers of the seventeenth and eighteenth centuries, and suggested that nothing happens without a sufficient reason, even if the reason cannot be always known to us [1, 2, 3]. This philosophical principle is known as the Principle of Sufficient Reason. The reason why this is my favorite one is that I believe that there is a reason for everything in this world we live.

What is a signal? Or what is a noise? In my research, 'Signal' is a signal of interest, whereas 'Noise' is a signal of uninterest. For others, the 'Signal' could be a 'Noise', and vice versa. Seeing photographs could help us understand this complication. My own camera is good for taking 'attractive' photos. The word 'attractive' to me was merely colorful and noiseless (clear). At first, I took a lot of beautiful amazing pictures by using the mirrorless camera. Then, I got involved in the photo editing, I found that the 'beautiful' I had thought was only one kind of the esthetic concept. If you read photo magazines, you can find variety of amazing photos not only colorful and noiseless but also monochromes, analog-like, antique-like and so on. Those photos contain certain noise, e.g. color-dulling, distorted etc. I had always thought an 'attractive picture' as a colorful and noiseless one. However, I realized that was not always the case through this research. Others may take the photos the opposite way from my view. This issue of photos could be transferred into various fields, e.g. art, food, news etc. It is appropriate to think that 'Signal' and 'Noise' are the same in a way. This means that 'Signal extraction' is the same processing as 'Noise reduction', and vice versa. In other words, 'Signal extraction' and 'Noise reduction' are inextricably linked together.

We live in the information society and 'Signal extraction' and 'Noise reduction' are important research topic in various fields [4, 5, 6, 7, 8]. 'Signal extraction' and 'Noise reduction' have become important to clinical diagnosis in the recent years [9, 10, 11, 12, 13, 14]. Novel techniques, which reveal unknown brain function from biosignals, are attracting attention to contribute to clinical diagnosis. Understanding the spatiotemporal characteristics of brain activities has been the longstanding aim over the decades [14]. During the time, there has been

a growing interest in studying and discovering specific prognostic and predictive biomarkers that tackle a wide variety of brain related pathologies and cognitive functions by means of both imaging and signal acquisition modalities. Functional magnetic resonance imaging (fMRI), Near-infrared spectroscopy (NIRS) and Electroencephalogram (EEG), Magnetoencephalogram (MEG) devices are capable of recording hemodynamic and/or neuronal signals, respectively. In the view of spatiotemporal resolution, these modalities are often compared with one another. Imaging acquisition modalities (fMRI and NIRS) have good spatial resolution that could potentially be down to the scale of cortical columns and different cortical layers, and have poor temporal resolution in the range of seconds. In contrast to imaging acquisition modalities, signal acquisition modalities (EEG and MEG) measure neuronal currents or magnetic fields directly from the subject's scalp with high temporal resolutions in the range of milliseconds. However, theses spatial resolutions are poor due to the limited number of EEG and MEG channels.

Signal based modalities are able to record events in a millisecond timeframe, which is a strong advantage considering that an action potential takes millisecond resolution to propagate across a single neuron. Hence, EEG and MEG are perfect candidates for extracting signal-based biomarkers targeting brain diseases. these biomarkers can be potentially applied in diagnosis and disease progression monitoring. An important advantage of EEG measurement is that similar measurement techniques can be used in both preclinical and clinical studies. Moreover, the measurement can be performed in a relatively non-invasive, stress-free, and pain-free manner. EEG measurement can be performed in daily activities or while sleeping through the use of telemetric or ambulatory methods, which cannot be done in MEG measurement. Finding biomarkers that are predictive, translational and accessible which is both preclinically and clinically is a critical step in development of novel therapeutics. This could have significant impact on early cost-benefit decision making of compound development, reducing economic burden on the health-care system, and improving patient quality of life [15].

The EEG reflects the electrical activity of large populations of synchronized neurons, mostly cortical pyramidal neurons. Therefore, some diseases can be identified with an EEG easier than the ones with imaging modalities [16]. Indeed, EEG measurements have been successfully used in cognitive brain research and clinical diagnosis, e.g. attention-deficit hyperactivity disorder (ADHD) [17, 18, 19], schizophrenia [20, 21, 22], Alzheimer's disease [23, 24, 25], and so on. Researchers have focused on brain signals since the beginning of the last century and tended to develop methods of detection, purification, and classification of EEGs that enabled them to diagnose abnormal signals [26]. Analysis of EEG signals started during the early days of EEG measurements. Berger assisted by Dietch applied Fourier analysis to short EEG sequences [11], which was rapidly developed during the 1950s. Subsequently, English physician Walter developed EEG topography, that allowed for the mapping of electrical activity across the surface of the brain and this topography was used in psychiatry until the 1980s [26]. From 1990s to present, many techniques were developed to process EEG signal [11] such as time-domain

analysis [27, 28, 29], frequency-domain analysis [30, 31, 32, 33], blind source separations (BSS) [34, 35, 36, 37] and so on.

It is well known that scalp-measured EEG signals consist a mixture of an unknown number of brain and non-brain contributions. In other words, the EEG 'Signal' suffer from the presence of various 'Noise', which renders the identification and analysis of EEG activity difficult [38], and have certain drawbacks as a result of their low signal-to-noise ratio (SNR). SNR generically means the dimensionless ratio of the 'Signal' power to the 'Noise' power contained in a recording [39]. In order to improve low SNR of EEGs, there have been various 'Signal extraction' or 'Noise reduction' techniques of which SNR definitions are classified according to the types of 'Signal' and/or 'Noise' [34, 40, 41, 42, 43].

The objective of our present study is to increase SNR of the interested EEG 'Signal' to uninterested EEG 'Noise' by use of the signal processing techniques. In EEG measurement, ocular artifacts, e.g. electrooculograms (EOGs) and eye blinks, affect the EEG signals. The most commonly used method for dealing with artifacts in EEG analysis is to reject EEG trials with ocular artifacts larger than an arbitrarily preset value. However, when limited data are available, or ocular artifacts occur too frequently, the amount of data lost to artifact rejection may be unacceptable [34]. Hence, several methods have been proposed to remove ocular artifacts [34, 44, 45, 46]. In Chapter 3, 'Signal' is an uncontaminated EEG and 'Noise' is an ocular artifact. Few studies have focused on 'Signal' loss, i.e. the loss of EEGs derived from brain concurrently removed by artifacts reduction. In addition, there have been few obvious quantitative assessment methods for validation, this is partly because there is no access to the uncontaminated EEGs in experimental data [47]. We propose a novel ocular artifact removal method which focuses mainly on the extent to which the uncontaminated EEGs are retained. The novel method attempts to remove the ocular artifacts locally and reduce information loss of uncontaminated EEGs.

In Chapter 4, we develop a novel signal noise separation method for the Event-related potential (ERP). In this chapter, 'Signal' is the ERP and 'Noise' is the background EEGs which are intrinsic artifacts, e.g. alpha rhythms and beta rhythms. We attempt to remove the background EEGs to increase SNR of the ERP while we remove ocular artifacts which are extrinsic artifacts in Chapter 3. The amplitude of the ERP, is usually much lower than that of the background EEGs, and is hard to be seen in a raw EEG tracing. Because of this low SNR, a number of single trials that are time-locked to a specific event are required to be averaged to enhance the ERP. Although the SNR of the ERP increases with increase in the number of trials, a long recording time is required, and fatigue is likely to be experienced by its subjects [48]. The fatigue should be avoided in clinical situation. Therefore, we propose a novel method to reduce background rhythmic oscillatory activities from single-trial EEGs to enhance the ERP.

The analysis of the brain rhythmic oscillatory activities has become an important branch of neuroscience [16] whereas 'Noise' for the ERP. Researches on the functional correlates of

brain oscillations are increasing significantly. Publications on oscillatory responses in pathology are still rare, whereas a large number of other studies have been published concerning brain rhythmic oscillatory activities in the cognitive processes of healthy subjects [16]. The event-related power changes of oscillatory responses occur within specific frequency bands that may correspond to a decrease (event-related desynchronization: ERD) or an increase (event-related synchronization: ERS) in synchrony of certain activated neurons in the underlying neuronal population [49, 50]. Several clinical studies reported the abnormality of ERD and ERS in patients [51, 52, 53, 54].

In Chapter 5, we propose a novel method to extract and visualize ERD/ERS within an alpha frequency band. In ERD/ERS analysis, the short-time Fourier transform (STFT) and the wavelet transform (WT) are often employed to extract them. However, because of uncertainty principle, the STFT and the WT tends to obscure intrawave frequency fluctuations and smear the energy over a much wider frequency range [55, 56]. Therefore, the proposed method attempts to extract rhythmic oscillatory activities more precisely and to visualize them more clearly than the STFT and the WT.

In Chapter 6, we apply the proposed method in Chapter 3 to the clinical EEG data. These EEGs are recorded from both healthy subjects and schizophrenia patients. It is well known that patients with schizophrenia have deficits in many domains ranging from abnormalities in basic sensory registration and processing [57]. The abnormality of synchrony within a gamma frequency band was recorded by EEG measurements. Recently, it was revealed in chronic phase schizophrenia patients whereas that in not-chronic phase schizophrenia patients, i.e. ultra-high risk or first-episode schizophrenia patients, are still poorly understood. Therefore, we seek to reveal the difference in abnormality of synchrony within a gamma frequency band among the severity of schizophrenia. In this study, the proposed method is available to ocular artifacts without information loss of gamma band activities and is expected to expand the number of analyzable trials.

References

[1] Leibniz, G. W. (1976). The principles of nature and of grace, based on reason. Philosophical Papers and Letters, 2, 636–642.

[2] Chaitin, G. (2006). The limits of reason. Scientific American, 294(3), 74–81.

[3] Look, B. C. (2007). Gottfried Wilhelm Leibniz. The Stanford Encyclopedia of Philosophy (Fall 2013 Edition), URL = ⟨http://plato.stanford.edu/archives/fall2013/entries/leibniz/⟩.

[4] Landgrebe, D. (1999). Information extraction principles and methods for multispectral and hyperspectral image data. Information processing for remote sensing, 82, 3–38.

[5] Kitagawa, G., Takanami, T., & Matsumoto, N. (2001). Signal Extraction Problems in Seismology. International statistical review, 69(1), 129–152.

[6] Zhang, R. R., Ma, S., Safak, E., & Hartzell, S. (2003). Hilbert-Huang transform analysis of dynamic and earthquake motion recordings. Journal of engineering mechanics, 129(8), 861–875.

[7] Matsuo, Y., & Ishizuka, M. (2004). Keyword extraction from a single document using word co-occurrence statistical information. International Journal on Artificial Intelligence Tools, 13(01), 157–169.

[8] Stumme, G., Hotho, A., & Berendt, B. (2006). Semantic web mining: State of the art and future directions. Web Semantics: Science, Services and Agents on the World Wide Web, 4(2), 124–143.

[9] Soltanian-Zadeh, H., Windham, J. P., & Peck, D. J. (1996). Optimal linear transformation for MRI feature extraction. Medical Imaging, IEEE Transactions on, 15(6), 749–767.

[10] Kim, J. K., & Park, H. W. (1999). Statistical textural features for detection of microcalcifications in digitized mammograms. Medical Imaging, IEEE Transactions on, 18(3), 231–238.

[11] Sanei, S., & Chambers, J. A. (2008). EEG signal processing. John Wiley & Sons, Inc.

[12] Magnin, B., Mesrob, L., Kinkingnehun, S., Pelegrini-Issac, M., Colliot, O., Sarazin, M., ... & Benali, H. (2009). Support vector machine-based classification of Alzheimer ’s disease from whole-brain anatomical MRI. Neuroradiology, 51(2), 73–83.

[13] Luck, S. J., Mathalon, D. H., O’Donnell, B. F., Hamalainen, M. S., Spencer, K. M., Javitt, D. C., & Uhlhaas, P. J. (2011). A roadmap for the development and validation of event-related potential biomarkers in schizophrenia research. Biological psychiatry, 70(1), 28–34.

[14] Sakkalis, V., & Marias, K. (2012). EEG Based Biomarker Identification Using Graph-Theoretic Concepts: Case Study in Alcoholism. Optimization and Data Analysis in Biomedical Informatics, 63, 71–189.

[15] Leiser, S. C., Dunlop, J., Bowlby, M. R., & Devilbiss, D. M. (2011). Aligning strategies for using EEG as a surrogate biomarker: a review of preclinical and clinical research. Biochemical pharmacology, 81(12), 1408–1421.

[16] Başar, E., & Güntekin, B. (2008). A review of brain oscillations in cognitive disorders and the role of neurotransmitters. Brain research, 1235(15), 172–193.

[17] Matousek, M., Rasmussen, P., & Gillberg, C. (1984). EEG frequency analysis in children with so-called minimal brain dysfunction and related disorders. Advances in biological psychiatry, 15, 102–108.

[18] Snyder, S. M., & Hall, J. R. (2006). A meta-analysis of quantitative EEG power associated with attention-deficit hyperactivity disorder. Journal of Clinical Neurophysiology, 23(5), 441–456.

[19] Clarke, A. R., Barry, R. J., McCarthy, R., & Selikowitz, M. (2001). Electroencephalogram differences in two subtypes of Attention ‐ Deficit/Hyperactivity Disorder. Psychophysiology, 38(2), 212–221.

[20] Kwon, J. S., O'Donnell, B. F., Wallenstein, G. V., Greene, R. W., Hirayasu, Y., Nestor, P. G., ... & McCarley, R. W. (1999). Gamma frequency-range abnormalities to auditory stimulation in schizophrenia. Archives of General Psychiatry, 56(11), 1001–1005.

[21] Krishnan, G. P., Vohs, J. L., Hetrick, W. P., Carroll, C. A., Shekhar, A., Bockbrader, M. A., & O'Donnell, B. F. (2005). Steady state visual evoked potential abnormalities in schizophrenia. Clinical neurophysiology, 116(3), 614–624.

[22] Spencer, K. M. (2011). Baseline gamma power during auditory steady-state stimulation in schizophrenia. Frontiers in human neuroscience, 5, 1–7.

[23] Polich, J., Ladish, C., & Bloom, F. E. (1990). P300 assessment of early Alzheimer's disease. Electroencephalography and Clinical Neurophysiology/Evoked Potentials Section, 77(3), 179–189.

[24] Stam, C. J., Van Der Made, Y., Pijnenburg, Y. A. L., & Scheltens, P. H. (2003). EEG synchronization in mild cognitive impairment and Alzheimer's disease. Acta Neurologica Scandinavica, 108(2), 90–96.

[25] Montez, T., Poil, S. S., Jones, B. F., Manshanden, I., Verbunt, J. P., van Dijk, B. W., ... & Linkenkaer-Hansen, K. (2009). Altered temporal correlations in parietal alpha and prefrontal theta oscillations in early-stage Alzheimer disease. Proceedings of the National Academy of Sciences, 106(5), 1614–1619.

[26] Al-Kadi, M. I., Reaz, M. B. I., & Ali, M. A. M. (2013). Evolution of Electroencephalogram Signal Analysis Techniques during Anesthesia. Sensors, 13(5), 6605–6635.

[27] Arnold, M., Milner, X. H. R., Witte, H., Bauer, R., & Braun, C. (1998). Adaptive AR modeling of nonstationary time series by means of Kalman filtering. Biomedical Engineering, IEEE Transactions on, 45(5), 553–562.

[28] Tarvainen, M. P., Hiltunen, J. K., Ranta-aho, P. O., & Karjalainen, P. A. (2004). Estimation of nonstationary EEG with Kalman smoother approach: an application to event-related synchronization (ERS). Biomedical Engineering, IEEE Transactions on, 51(3), 516–524.

[29] Georgiadis, S. D., Ranta-aho, P. O., Tarvainen, M. P., & Karjalainen, P. A. (2005). Single-trial dynamical estimation of event-related potentials: a Kalman filter-based approach. Biomedical Engineering, IEEE Transactions on, 52(8), 1397–1406.

[30] Tobimatsu, S., Zhang, Y. M., & Kato, M. (1999). Steady-state vibration somatosensory evoked potentials: physiological characteristics and tuning function. Clinical neurophysiology, 110(11), 1953–1958.

[31] Quian Quiroga, R., Sakowitz, O. W., Basar, E., & Schurmann, M. (2001). Wavelet transform in the analysis of the frequency composition of evoked potentials. Brain Research Protocols, 8(1), 16–24.

[32] Giabbiconi, C. M., Dancer, C., Zopf, R., Gruber, T., & Muller, M. M. (2004). Selective spatial attention to left or right hand flutter sensation modulates the steady-state somatosensory evoked potential. Cognitive brain research, 20(1), 58–66.

[33] Muthukumaraswamy, S. D., & Johnson, B. W. (2004). Primary motor cortex activation during action observation revealed by wavelet analysis of the EEG. Clinical Neurophysiology, 115(8), 1760–1766.

[34] Jung, T. P., Makeig, S., Humphries, C., Lee, T. W., Mckeown, M. J., Iragui, V., & Sejnowski, T. J. (2000). Removing electroencephalographic artifacts by blind source separation. Psychophysiology, 37(2), 163–178.

[35] Davies, M. E., & James, C. J. (2007). Source separation using single channel ICA. Signal Processing, 87(8), 1819–1832.

[36] Klemm, M., Haueisen, J., & Ivanova, G. (2009). Independent component analysis: comparison of algorithms for the investigation of surface electrical brain activity. Medical & biological engineering & computing, 47(4), 413–423.

[37] De Lucia, M., Michel, C. M., & Murray, M. M. (2010). Comparing ICA-based and single-trial topographic ERP analyses. Brain topography, 23(2), 119–127.

[38] Campos Viola, F., Thorne, J., Edmonds, B., Schneider, T., Eichele, T., & Debener, S. (2009). Semi-automatic identification of independent components representing EEG artifact. Clinical Neurophysiology, 120(5), 868–877.

[39] Johnson, D. H. (2006). Signal-to-noise ratio. Scholarpedia, 1(12), 2088.

[40] . Quiroga, R. Q., & Garcia, H. (2003). Single-trial event-related potentials with wavelet denoising. Clinical Neurophysiology, 114(2), 376–390.

[41] Kierkels, J. J., van Boxtel, G. J., & Vogten, L. L. (2006). A model-based objective evaluation of eye movement correction in EEG recordings. Biomedical Engineering, IEEE Transactions on, 53(2), 246–253.

[42] Lemm, S., Curio, G., Hlushchuk, Y., & Muller, K. R. (2006). Enhancing the signal-to-noise ratio of ICA-based extracted ERPs. Biomedical Engineering, IEEE Transactions on, 53(4), 601–607.

[43] De Vos, M., Vergult, A., De Lathauwer, L., De Clercq, W., Van Huffel, S., Dupont, P., ... & Van Paesschen, W. (2007). Canonical decomposition of ictal scalp EEG reliably detects the seizure onset zone. NeuroImage, 37(3), 844–854.

[44] Jung, T. P., Humphries, C., Lee, T. W., Makeig, S., McKeown, M. J., Iragui, V., & Sejnowski, T. J. (1998). Extended ICA removes artifacts from electroencephalographic recordings. Advances in neural information processing systems, 894–900.

[45] Croft, R. J., & Barry, R. J. (2000). Removal of ocular artifact from the EEG: a review. Neurophysiologie Clinique/Clinical Neurophysiology, 30(1), 5–19.

[46] De Vos, M., De Lathauwer, L., & Van Huffel, S. (2011). Spatially constrained ICA algorithm with an application in EEG processing. Signal Processing, 91(8), 1963–1972.

[47] Lindsen, J. P., & Bhattacharya, J. (2010). Correction of blink artifacts using independent component analysis and empirical mode decomposition. Psychophysiology, 47(5), 955–960.

[48] SJ, Nasuto., & JD, S. (2011). Evaluation of empirical mode decomposition for event-related potential analysis. EURASIP Journal on Advances in Signal Processing, 2011, 11 pages.

[49] Pfurtscheller, G., & Neuper, C. (1997). Motor imagery activates primary sensorimotor area in humans. Neuroscience letters, 239(2), 65–68.

[50] Pfurtscheller, G., & Lopes da Silva, F. H. (1999). Event-related EEG/MEG synchronization and desynchronization: basic principles. Clinical neurophysiology, 110(11), 1842–1857.

[51] Sauseng, P., Klimesch, W., Schabus, M., & Doppelmayr, M. (2005). Fronto-parietal EEG coherence in theta and upper alpha reflect central executive functions of working memory. International Journal of Psychophysiology, 57(2), 97–103.

[52] Gomarus, H. K., Althaus, M., Wijers, A. A., & Minderaa, R. B. (2006). The effects of memory load and stimulus relevance on the EEG during a visual selective memory search task: an ERP and ERD/ERS study. Clinical Neurophysiology, 117(4), 871–884.

[53] Koh, Y., Shin, K. S., Kim, J. S., Choi, J. S., Kang, D. H., Jang, J. H., ... & Kwon, J. S. (2011). An MEG study of alpha modulation in patients with schizophrenia and in subjects at high risk of developing psychosis. Schizophrenia research, 126(1), 36–42.

[54] Kurimoto, R., Ishii, R., Canuet, L., Ikezawa, K., Iwase, M., Azechi, M., ... & Takeda, M. (2012). Induced oscillatory responses during the Sternberg's visual memory task in patients with Alzheimer's disease and mild cognitive impairment. Neuroimage, 59(4), 4132–4140.

[55] Huang, N. E., Shen, Z., Long, S. R., Wu, M. C., Shih, H. H., Zheng, Q., ... & Liu, H. H. (1998). The empirical mode decomposition and the Hilbert spectrum for nonlinear and non-stationary time series analysis. Proceedings of the Royal Society of London. Series A: Mathematical, Physical and Engineering Sciences, 454(1971), 903–995.

[56] Pigorini, A., Casali, A. G., Casarotto, S., Ferrarelli, F., Baselli, G., Mariotti, M., ... & Rosanova, M. (2011). Time–frequency spectral analysis of TMS-evoked EEG oscillations by means of Hilbert–Huang transform. Journal of neuroscience methods, 198(2), 236–245.

[57] Light, G. A., Hsu, J. L., Hsieh, M. H., Meyer-Gomes, K., Sprock, J., Swerdlow, N. R., & Braff, D. L. (2006). Gamma band oscillations reveal neural network cortical coherence dysfunction in schizophrenia patients. Biological psychiatry, 60(11), 1231–1240.

Chapter 2

Background

In this chapter, we describe basic principles of EEGs and some signal processing techniques related to method proposed in this study. The physiological principles were provided from perspectives of SNR of EEGs, i.e. ocular artifacts, ERPs and rhythmic activities. In addition, we describe about three signal processing technique: Time domain analysis; Time–frequency analysis; Multivariate analysis.

2.1 Electroencephalogram (EEG)

2.1.1 Basis of EEG [1, 2, 3, 4]

The birth of the EEG is generally in 1875 when Caton [5] presented the first recording of brain electrical activity from some animals by using a galvanometer. However Caton observed lots of electrical activity, e.g. strongly marked electrical current changes by light stimulation and modifications associated with the rabbits awoke from sleep, he could not record these results because he did not have a camera. The year of the first publication which illustrated the stimulation effects in dog EEG was 1913 by Russian physiologist, Prawdicz-Neminski [6]. The human EEG was first recorded by Berger and published in 1929 [7]. He had reported human EEGs for long time and concluded that the EEG represented the material concomitants of mental processed and the cerebrum functioned as an undivided whole. From the era down to the present date, EEG becomes one of the major techniques for studying the human brain function.

The EEG represents a set of field potentials, the synchronized activity of large numbers of cells, as recorded by multichannel on the surface of the scalp (Figure 2.1). However, not all cells contribute equally to the surface EEG, and the deep structures do not contribute directly to it because the surface EEG mainly reflects the activity of cortical neurons close to the EEG electrode. Pyramidal neurons are the major projection neurons in the cortex, and is the principle source of EEG activities. the surface EEG is hypothesized to be generated by the summation of excitatory and inhibitory postsynaptic potentials (EPSP and IPSP) in pyramidal neurons (Figure 2.2). If an action potential travels along a fiber ending in an excitatory synapse, it leads a

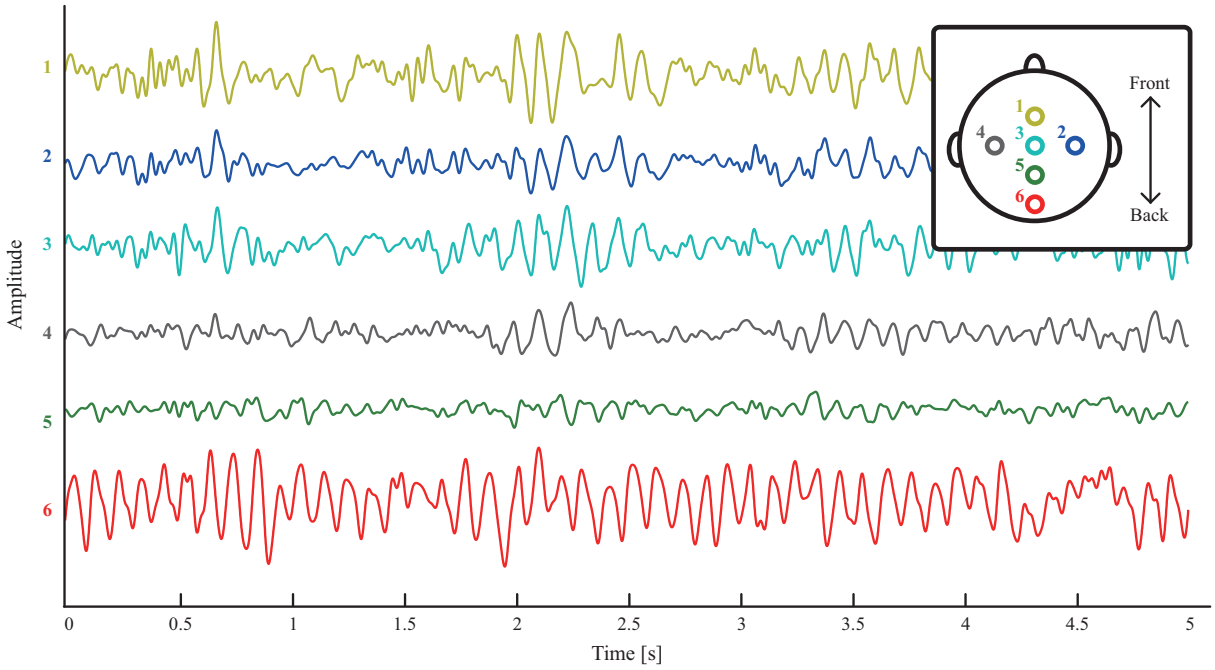

Figure 2.1: Representative EEG waveforms measured some electrodes (1–6) on the surface of the scalp.

membrane depolarization, which is called an excitatory postsynaptic potential (EPSP). An action potential is a discrete voltage from the beginning of the axon at the cell body to the axon terminals. If multiple action potentials travel along the same fiber with a short interval, there will be a summation of EPSP which reaches the membrane threshold and triggers an action potential on the postsynaptic neuron. If an action potential travels along a fiber ending in an inhibitory synapse, then a membrane hyperpolarization, which is called an inhibitory postsynaptic potential (IPSP), will occur.

A net inflow of cations across the subsynaptic membrane accompanies EPSP, and elicits a potential gradient along the nerve cell membrane in the intra- and extracellular spaces. Because of the potential gradient, cations flows across the cell membrane through the extracellular space in direction of the subsynaptic region. The current then flows down the intracellular space and completes the loop by exiting through the membrane (2.3). On the other hand, with IPSP, there is an inflow of anions into the nerve cell (and/or an outflow of cations from the nerve cell), and the current flow will have a direction opposite to that in the case of EPSP. If EPSPs arise at superficial cortical layer or IPSPs arise at deeper layer, the negativity at superficial layer and the positivity at deeper layer create a tiny dipole. As a result, surface EEGs have negative potentials. A dipole is simply a pair of positive and negative electrical charges. Conversely, surface EEGs have positive potentials if EPSPs arise at deeper layer or IPSPs arise at superficial layer.

Because the electrical activity originates in neurons in the underlying brain tissue, scalp

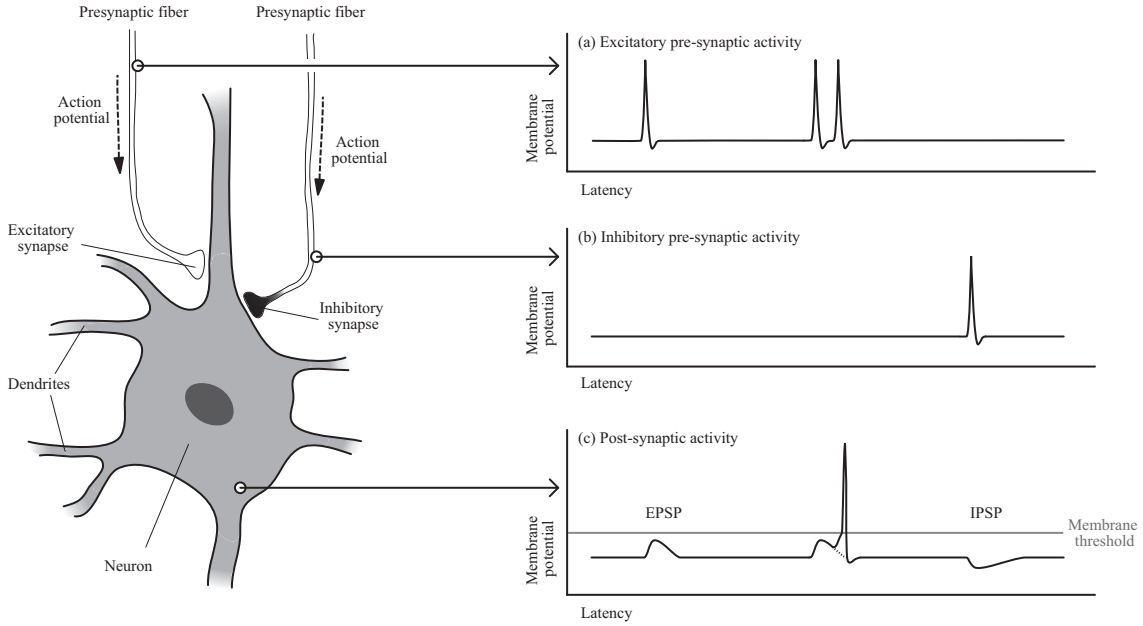

Figure 2.2: Action potentials in the excitatory and inhibitory presynaptic fibers lead to excitatory postsynaptic potential (EPSP) and inhibitory postsynaptic potential (IPSP), respectively, in the postsynaptic neuron. Two EPSPs sum up to a superthreshold potential, triggering an action potential in the postsynaptic neuron. (Modified from [3])

EEGs depend on the directions and distances of the electrical sources with respect to the electrodes. Scalp EEGs are inevitably distorted by the filtering and attenuation produced by many layers of brain tissue and bone, which is called volume conduction. Therefore, the amplitude of a scalp EEG (microvolts) is much smaller than that of a single neuron.

2.1.2 Event-related potential (ERP) [8, 9, 10]

The EEGs consist of the neural responses related to specific sensory, cognitive and motor events and it is possible to extract these responses from the overall EEG by means of a simple averaging technique. These specific responses are treated globally under the common term, ERPs.

The first unambiguous sensory ERP recordings from awake humans were performed in 1935–1936 by Puline and Hallowell Davis, and published a few years later [12]. The modern era of the ERP research began in 1964, when Walter et al. reported the first cognitive ERP component [13]. They found a large negative voltage, which seemed to reflect the motor preparation, at a frontal electrode. This study led many researchers to begin exploring cognitive ERP components. The next major advance was the discovery of the P300 component by Sutton et al. [14]. They found that when subjects could not predict whether the next stimulus would be auditory or visual, the stimulus elicited a large positive P300 components that peaked around 300 ms post stimulus; this component was much smaller when the modality of the stimulus was

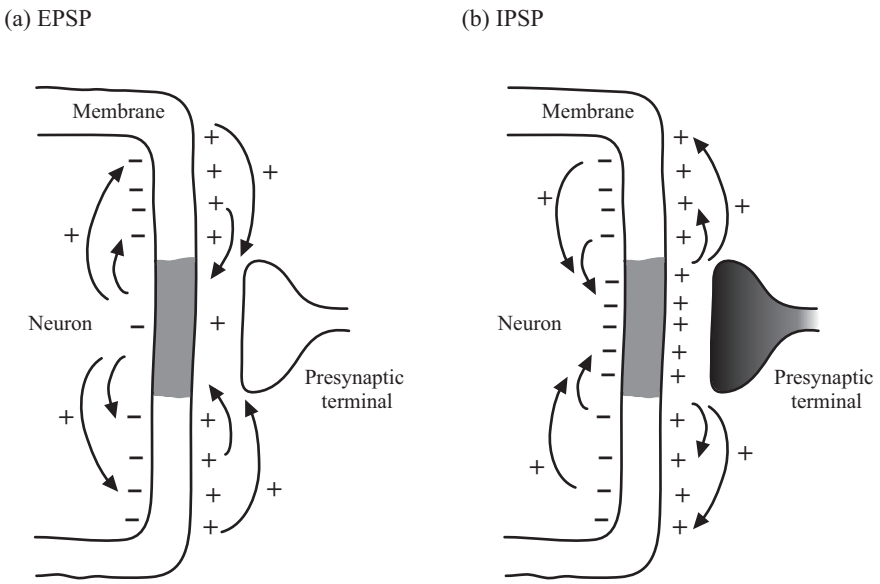

Figure 2.3: During EPSP and IPSP, ionic current flows occur through as well as along the neuronal membrane, as shown by arrows. The density of + and − signs indicate the polarization of the subsynaptic (gray area) as well as that of the postsynaptic membrane during synaptic activation. (Modified from [3])

perfectly predictable. This result was then a very hot topic in cognitive psychology. Over the ensuing fifteen years, a great deal of research focused on identifying various cognitive ERPs in cognitive experiments. The term 'event related potentials' (ERPs) is proposed to designate the general class of potentials that display stable time relationships to a definable reference event [15].

ERPs generally reflect postsynaptic potentials, and can be recorded at surface electrodes under certain conditions. However little research has examined the biophysical events that give rise scalp ERPs, it seems that huge number of dipoles from corresponding neurons summate under certain conditions, making it possible to measure the summated voltages at the scalp electrodes. For the summated voltages to be recordable at the scalp electrodes, they must occur at approximately the same time across thousands or millions of neurons. In addition, the dipoles from individual neurons must be spatially aligned to avoid cancelation of the summated voltages. The summation of the dipoles is complicated because the cortex is not flat but folded. However, the summation of many dipoles is essentially equivalent to a single dipole formed by averaging the directions of the individual dipoles, which is called an equivalent current dipole (ECD). The position and directions of ECD determine the distribution of ERP at the scalp.

There is a need for several signal processing steps to extract ERPs at the scalp because of the low SNR of ERP. Various artifacts, e.g. eye-blinks, may contaminate the EEG, and this problem can be addressed by identifying and removing trials with artifacts or by subtracting an estimate

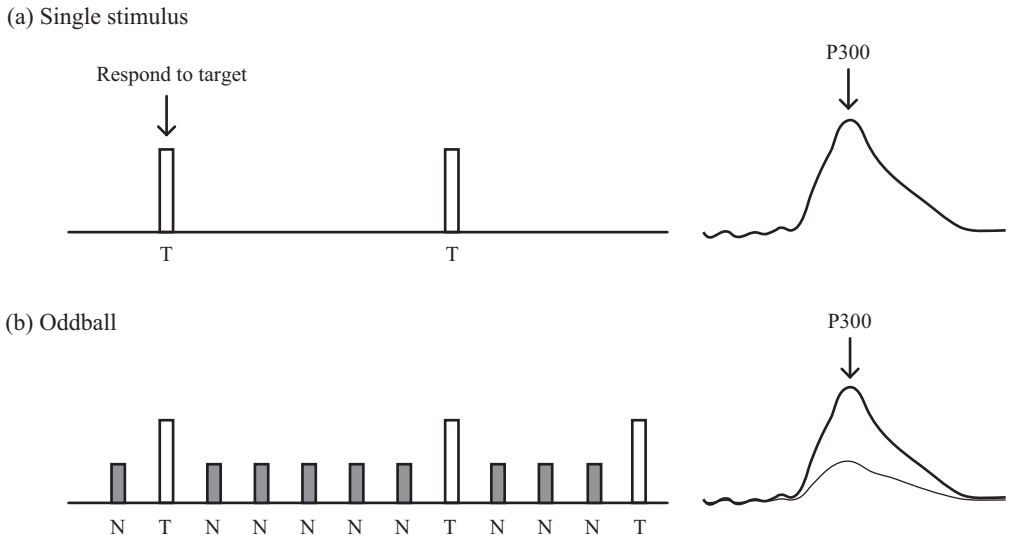

Figure 2.4: Schematic illustration of (a) the single-stimulus, and (b) oddball (lower) paradigms, with the elicited ERPs from the stimuli of each task. The single-stimulus task presents only an infrequent target (T). The oddball task presents two different stimuli in a random sequence, with target stimuli occurring less frequently than non-target stimuli (target = 'T', non-target = 'N'). In each task, the subject is instructed to respond to the target and otherwise to refrain from responding. The target elicits the P300 (Modified from [16]).

of the artifactual activity from the EEG. Once artifacts have been eliminated, averaging of some sort is usually necessary to extract ERPs from the overall EEG. Various signal processing techniques are then applied to the data to remove noise and isolate specific ERP components. These processing lead to positive and negative deflections of ERP waveform. The polarity of a component is denoted by the letters "N", i.e. negative, or "P", i.e. positive. The different positive and negative deflections are then labeled in the order of their appearance, e.g. P1, N1, etc., by their characteristic peak latencies, e.g. N100, P300, etc.

Among these components, P300 is one of the most prominent ERPs and is considered to reflect cognitive brain activities. However there have been the thousands of P300 researches, there is still no clear consensus view on what neural or cognitive process the P300 wave reflects. Nevertheless, the factors which influence its amplitude and latency is revealed. The "oddball" paradigm is often used to obtain the P300. The traditional two-stimulus oddball presents two different stimuli in a random sequence (Figure 2.4), with one (Target stimulus) occurring less frequently than the other (Non-target stimulus). In the case of oddball paradigm, P300 amplitude is small for relatively rapid stimulus presentations whereas its amplitude is large for stimulus occurring at longer intervals. P300 peak latency is proportional to stimulus evaluation timing, is sensitive to task processing demands, and varies with individual differences in cognitive capability [11].

Recently, the P300 is attracting clinical attention. Some studies suggested that the P300 is valuable to distinguish between subcortical, e.g. Parkinson's disease, and cortical dementias, e.g. Alzheimer's disease [17], and between patients with dementia and those with pseudo-dementia in the course of depression [18]. Other studies have reported the availability of the P300 to explore information processing in a variety of neurological disorders, e.g. schizophrenia, alcoholism, etc. Therefore, the P300 is considered to have characteristics of biomarker.

2.1.3 Rhythmic activities [10]

EEG oscillations reflect rhythmic changes in the (relative) level of depolarization in the membrane potentials of a huge number of neurons. Consequently,they reflect phases of low versus high excitability. The EEG oscillations contain a fairly wide frequency spectrum, but it is not simply a patchwork of frequencies and its frequency range does not have a fully defined. Generally, lower frequencies (e.g. delta and theta) show large synchronized amplitude, whereas higher frequencies (e.g. beta and gamma) show small desynchronized amplitude. These frequencies are often categorized as the following bands or ranges: Delta (1–3 Hz); Theta (4–7 Hz); Alpha (8–13 Hz); Beta (16–30 Hz); Gamma (36–44 Hz). This is the old-fashioned breakdown of the EEG frequencies.

The alpha wave is the most prominent rhythm among the brain rhythms and can be visually observed in raw signal. Most subjects produce some alpha waves with their eyes closed in the posterior half of the head. It is reduced or eliminated by opening the eyes, by hearing unfamiliar sounds, by anxiety, or mental concentration or attention. However the generators of alpha rhythms are not known yet, they are considered to stem from rhythmic fluctuations of inhibitory neurons in theory and play an important role during synchronized rhythmic activity.

The alpha suppression due to sensory processing or motor behavior is well known as ERD. Alpha band ERD has been thought to reflect a decrease of oscillatory activity related to an internally or externally paced event. Recent basic researches showed that ERD (in the extended alpha frequency range of about 7–13.5 Hz) can be observed in response to a various tasks [19], and classified into lower alpha ERD (7–10 Hz) and upper alpha ERD (10–13.5 Hz). Lower alpha band ERD is probably related to attentional demands and upper alpha band ERD showed a clear relation to semantic processing. These findings demonstrated that it is functionally closely related to active information processing in the sense of excitatory brain process [20].

In contrast to ERD, the increase of rhythmic activity is known as ERS, and alpha band ERS has been considered to reflect a brain state of reduced information processing [21] consistent with the concept of idling [22]. On the other hand, Klimesch et al. [20] argued that alpha band ERS reflects a state of inhibitory brain process because alpha band ERS can be observed selectively in tasks where a learned response must be withhold and over brain areas that are not task-relevant.

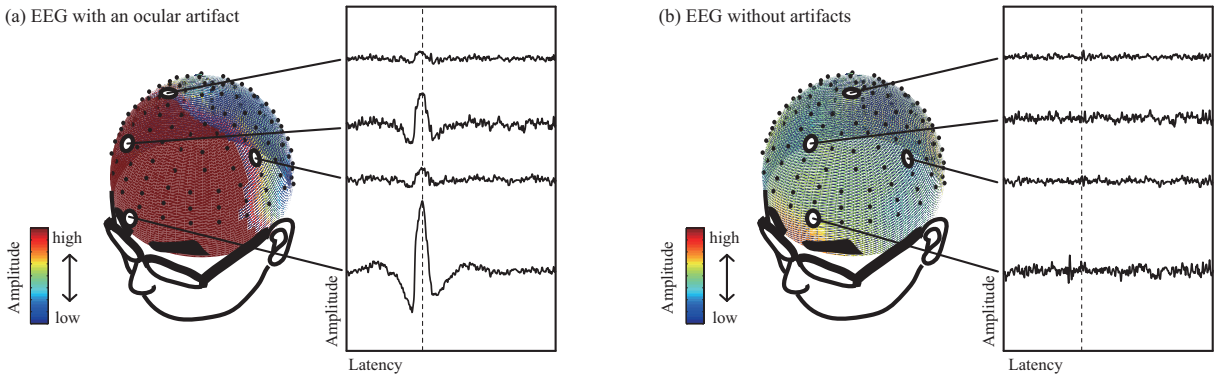

Figure 2.5: Illustrations of a typical ocular artifact. The scalp distributions and waveforms of (a) contaminated EEGs with an ocular artifact, and (b) EEGs without artifacts.

2.1.4 Artifacts

The raw EEG signal is always contaminated by various artifacts. These artifacts are roughly classified into biological and non-biological artifacts. Non-biological artifacts primarily derived from power lines (50/60 Hz), additional electrical noise, etc. The non-biological artifacts can be greatly reduced by using 50/60 Hz notch filters, proper subject grounding, and shield of the recording system. Biological artifacts are further distinguished into artifacts derived from non-brain regions, e.g. EOG, electrocardiogram, and electromyogram, and those derived from brain regions. Here, we introduce the details of ocular artifacts and background EEGs noted in Chapters 3 and 4.

Ocular artifacts [8]

When measuring ERP and ERS/ERD using visual stimuli, ocular artifacts such as eye-blinks and eye movements, are inevitable. The amplitudes of ocular artifacts are several dozens or hundreds times larger than those of EEG signals derived from a brain, and those frequencies are often up to alpha band (and to a lesser extent the beta band). Within each eye, there is an electrical gradient with positive at the front of the eye and negative at the back of the eye, and the voltage deflections recorded near the eye are mainly caused by the movement of the eyelids across the eyes. In eye-blinks, the movement modulates the conduction of the electrical potentials of the eyes to the surrounding regions mainly in anterior sites. Similar to eye-blinks, eye-movements are thought to be a movement of a dipole with its positive and pointing toward the front of the eye. This dipole creates a constant DC voltage across the scalp if the eyes are stationary, whereas the voltage becomes more positive at sites where the eyes move toward. Figure 2.5 shows the typical scalp distributions and waveforms of the ocular artifacts at several electrodes on the scalp.

The conventional technique to avoid using trials including ocular artifacts is excluding trials

in which these maximal voltage exceed a threshold, such as ±100 μV. However, the process reduces the number of trials to be available for analyses, thereby decreases the SNR of ERP and ERD/ERS. For this reason, a variety of methods have been reported for the removal of ocular artifacts from measured EEGs as a pre-processing analysis. The simplest way is to calculate the propagation factor between the eyes and each of the scalp electrodes and subtract a corresponding proportion of the recorded EOG activity from the EEG waveform at each scalp site. However, this approach has a major fault that the EOG recorded brain activity along with true ocular activity, thus it subtracts parts of brain activities as well as ocular artifacts.

In recent years, ICA has been increasingly used for removal of ocular artifacts [23, 24]. In view of the fact that ocular artifacts typically do not occur time-locked to a given event or an evoked response, ICA is ideally suited to remove such interfering signals. The following section explains the principle of ICA and its application for ocular artifacts. In addition, Chapters 3 and 6 demonstrate that ICA is useful to remove ocular artifacts by using simulated and real-recorded EEGs.

Background EEGs

In the ERP analysis, the EEGs collected on a single trial is assumed to consist of an ERP and random artifacts. The ERP waveform is assumed to be identical on each trial, whereas the artifacts are assumed to be completely unrelated to the time-locking event. The artifacts are generally background EEGs, e.g. alpha waves, beta waves, etc. For example, the alpha wave is observed when subjects are drowsy or tired and its amplitude is much higher than ERP. The traditional approach to reduce the influence of the background EEGs is a trial averaging technique. First, EEG trials following an event are extracted from the continuous EEG. These trials are aligned with respect to the time-locking event and then simply averaged together. By using the trial averaging technique, the background EEGs are suppressed and the ERP waveform is emphasized [8] (Figure 2.6).

However, achieving a substantial increase in SNR requires a very large increase in the number of trials. It is said that it is usually much easier to improve the quality of data by decreasing sources of background EEGs than by increasing the number of trials. Large background EEGs might be a particular problem when there are limited numbers of trials. For example, in a typical oddball studies which induce the P300 (Figure 2.4), subjects are required to respond to an infrequent number of target stimuli. Because targets are infrequent, the P300 corresponding to the targets are composed of low number of trials and are generally more difficult to interpret [8]. Therefore, efficient methods to increase SNR of the P300 has been expected. In the meanwhile, there is no consistent view about the relationship between the P300 and background EEGs. Basar et al. [25] argued that the background EEG is not merely “noise” but also support the hypothesis for the P300. Intriligator and Polich [26] suggested that alpha band spectral power co-varies with the P300, and Basar et al. [25] indicated that the P300 includes more low

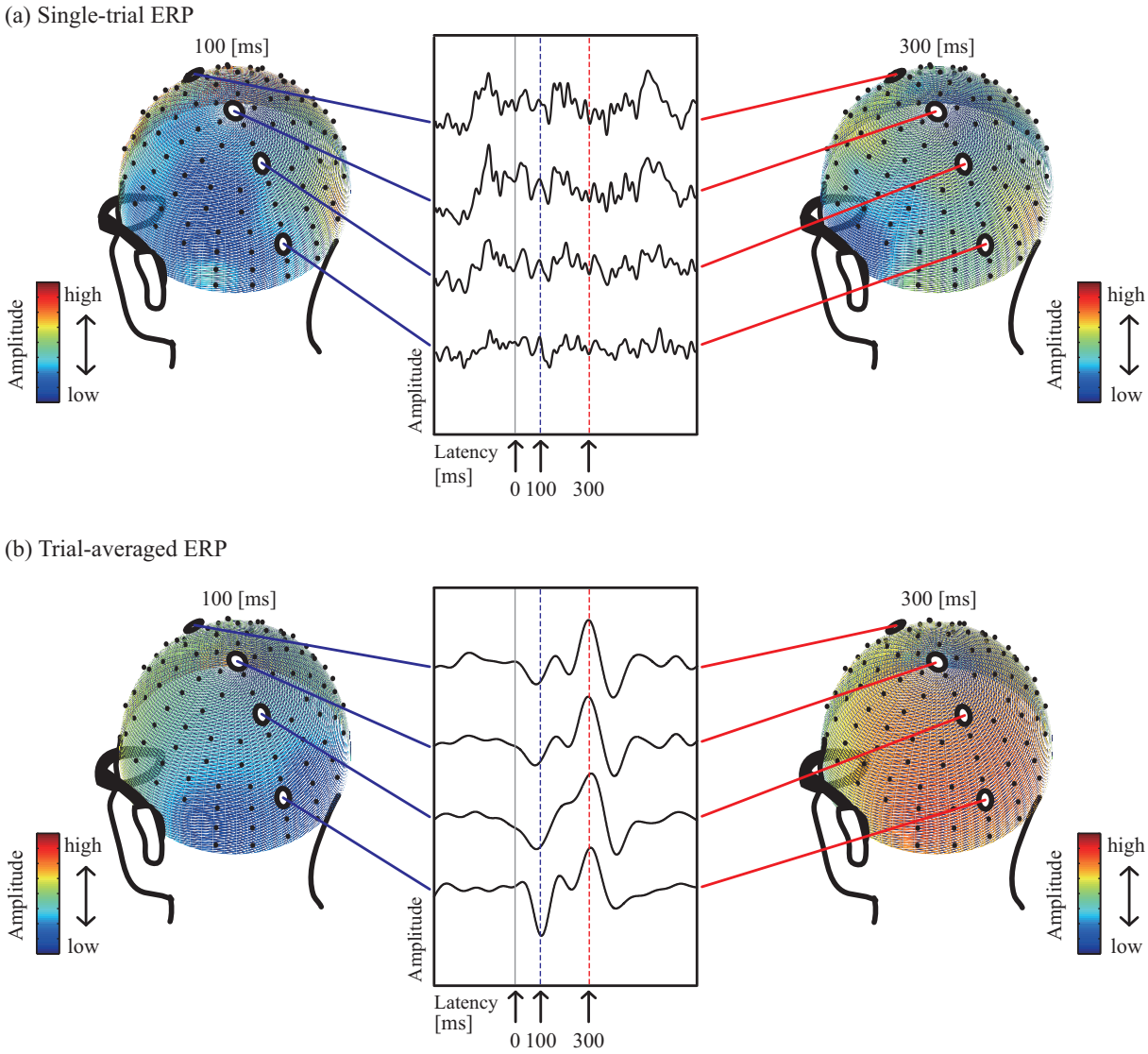

Figure 2.6: Schematic illustrations of ERPs with and without trial averaging. The scalp distributions and waveforms of (a) a single-trial ERP, and (b) trial-averaged ERP in 100ms and 300ms after a certain visual stimulus at 0 ms.

frequencies (delta frequency range) than the other sensory ERPs and its theta components are accompanied by increased focused attention.

Even under a state where the physiological basis of the P300 remains obscure as noted above, several methods have been proposed to increase its SNR, assuming some hypothetical situation for P300 [27, 28]. We also proposed a novel technique to do so in Chapter 4 by assuming that the P300 mainly consists of some components whose frequencies are lower than the alpha band.

2.2 Time domain analysis

2.2.1 Auto regressive model (AR model) [29]

An autoregressive (AR) model is a common model for linear time series model. Characterization of various physiological systems by auto regression techniques has become widely applied to EEG data for long decades [30, 31]. Linear time series models are designed to model the covariance structure in the time series.

Consider a time series $x(1), x(2), ..., x(n)$, an AR model of order n states that $x(t)$ is the linear function of the previous n values of the series as

$$x(t) = a_1 x(t-1) + a_2 x(t-2) + \cdots a_n x(t-n) + \epsilon(t), \tag{2.1}$$

where a_n is the AR parameters and $\epsilon(t)$ is the white noise process with zero mean and variance σ^2. Using the lag operator L ($Lx(t) = x(t-1)$), the AR model is rewritten by

$$x(t) = a_1 Lx(t) + a_2 L^2 x(t) + \cdots a_n L^n x(t) + \epsilon(t). \tag{2.2}$$

If the solutions of the lag polynomial

$$1 - a_1 L - a_2 L^2 - \cdots - a_n L^n = 0 \tag{2.3}$$

only have roots with absolute values larger than one, the AR process is stable. Then, autocovariances are calculated as

$$\gamma(\tau) = E[x(t-\tau)x(t)] = E[x(t-\tau)(a_1 Lx(t) + a_2 L^2 x(t) + \cdots + a_n L^n x(t) + \epsilon(t))]. \tag{2.4}$$

For $\tau = 0, 1, ..., n$, it holds that

$$\begin{aligned}
\gamma(0) &= a_1\gamma(1) + a_1\gamma(2) + \cdots + a_n\gamma(n) + \sigma^2, \\
\gamma(1) &= a_1\gamma(0) + a_2\gamma(1) + \cdots + a_n\gamma(n-1), \\
&\vdots \\
\gamma(n) &= a_1\gamma(n-1) + a_2\gamma(n-2) + \cdots + a_n\gamma(0).
\end{aligned} \tag{2.5}$$

If Equation (2.5) is divided by $\gamma(0)$, the initial conditions ($\tau = 1, ..., n$) can be derived from the so-called Yule-Walker equations as

$$\begin{aligned} \rho(1) = &\quad a_1 + a_2\rho(1) + \cdots + a_n\rho(n-1), \\ \rho(2) = &\quad a_1\rho(1) + a_2 + \cdots + a_n\rho(n-2), \\ &\vdots \\ \rho(n) = &\quad a_1\rho(n-1) + a_2\rho(n-2) + \cdots + a_n, \end{aligned} \tag{2.6}$$

where $\rho(n) = \gamma(n)/\gamma(0)$. Then, the Yule-Walker equations can be rewritten in matrix form as

$$\boldsymbol{\rho} = \mathbf{R}\mathbf{a} \tag{2.7}$$

where

$$\boldsymbol{\rho} = [\rho(1), \rho(2), ..., \rho(n)]^{\mathrm{T}}, \tag{2.8}$$

$$\mathbf{a} = [a_1, a_2, ..., a_n]^{\mathrm{T}}, \tag{2.9}$$

$$\mathbf{R} = \begin{bmatrix} 1 & \rho(1) & \rho(2) & \cdots & \rho(n-1) \\ \rho(1) & 1 & \rho(1) & \cdots & \rho(n-2) \\ \rho(2) & \rho(1) & 1 & \cdots & \rho(n-3) \\ \vdots & \vdots & \vdots & \ddots & \vdots \\ \rho(n-1) & \rho(n-2) & \rho(n-3) & \cdots & 1 \end{bmatrix}. \tag{2.10}$$

Finally, if the first p autocorrelation coefficients are given, the coefficients of the AR process can be calculated as

$$\mathbf{a} = \mathbf{R}^{-1}\boldsymbol{\rho}. \tag{2.11}$$

If the order of the AR process n is unknown, it can be estimated with the help of information criteria. In this dissertation, the Akaike information criterion (AIC) [32] is employed and calculated as

$$\mathrm{AIC} = \ln\frac{1}{T}\sum_{1}^{T} u^2(t) + m\frac{2}{T}, \tag{2.12}$$

where $u(t)$ is estimated residuals of the AR process, m is the number of estimated parameters and T is a signal length. The first term decreases when the number of estimated parameters increases whereas the second term increases when the number of estimated parameters increases. AR processes with successively increasing orders $n = 1, 2, ..., n_{\max}$ ($n_{\max}$ is an arbitrary cut off point) are estimated. Finally, the optimal order n is chosen which minimizes the respective criterion.

2.2.2 Klaman filter (KF) [33, 34, 35]

The Kalman filter (KF) is one of the most common optimal estimators for one-dimensional linear systems with Gaussian error statistics. The solution is recursive in that each updated

estimate of the state is computed from the previous estimate and the new input data. Typical uses of the KF include smoothing noisy data and providing estimates of parameters of interest and is widely used on various EEG analyses [36, 37]. The optimization criterion used in this dissertation is minimization of the mean-square estimation error of the process state vector $\mathbf{x}(k)$ (k denotes discrete time) defined as the minimal set of data which is sufficient to uniquely describe the unforced dynamical behavior of the system. In other words, the state is the least amount of data on the past behavior of the system that is needed to predict its future behavior. To estimate it, we use the observation vector $\mathbf{y}(k)$. The KF model assumes that the state of a system at a time $k+1$ evolved from the prior state at time k , and the AR model described in 2.2.1 is often employed for this model.

At first, we assume that the random process and its observation can be defined as follows

$$\mathbf{x}(k+1) = \boldsymbol{\varphi}(k+1|k)\mathbf{x}(k) + \mathbf{w}(k), \tag{2.13}$$

$$\mathbf{y}(k) = \mathbf{H}(k)\mathbf{x}(k) + \mathbf{v}(k), \tag{2.14}$$

where $\boldsymbol{\varphi}(k+1|k)$ is a transition matrix taking the state $\mathbf{x}(k)$ from time k to time $k+1$. $\mathbf{w}(k)$ is an input white noise contribution to the state vector at time k, $\mathbf{y}(k)$ is an observable at time k, $\mathbf{H}(k)$ is a measurement matrix and $\mathbf{v}(k)$ is an observation noise with a white sequence and having zero cross correlation with the $\mathbf{w}(k)$. The covariance matrices for the $\mathbf{w}(k)$ and $\mathbf{v}(k)$ vectors are given by

$$\begin{aligned} E[\mathbf{w}(k)\mathbf{w}^{\mathrm{T}}(i)] &= \begin{cases} \mathbf{Q}(k), & (i=k) \\ \mathbf{0}, & (i \neq k) \end{cases} \\ E[\mathbf{v}(k)\mathbf{v}^{\mathrm{T}}(i)] &= \begin{cases} \mathbf{R}(k), & (i=k) \\ \mathbf{0}, & (i \neq k) \end{cases} \\ E[\mathbf{w}(k)\mathbf{v}^{\mathrm{T}}(i)] &= \mathbf{0}, \text{ for all } k \text{ and } i \end{aligned} \tag{2.15}$$

The KF problem can be formally stated as follows: Use the entire observed data $\mathbf{y}(k) = [y(1)\ y(2)\ \cdots\ y(k)]$ to find for each $k \geq 1$ the minimum mean-square error estimate of the state $\mathbf{x}(i)$. The problem is called 'Filtering' if $i = k$, 'Prediction' if $i > k$, and 'Smoothing' if $i < k$. In Chapter 3, we handle the KF ('Filtering' and 'Smoothing') with the AR model to estimate observations of EEG data.

Filtering

We assume that we have an initial estimate of the process at time k, denoted as $\hat{\mathbf{x}}(k|k-1)$ based on all our knowledge about the process prior to k. The estimation error at time k is defined by

$$\mathbf{e}(k|k-1) = \mathbf{x}(k) - \hat{\mathbf{x}}(k|k-1), \tag{2.16}$$

and the associate error covariance matrix is

$$\begin{aligned}\mathbf{P}(k|k-1) &= E[\mathbf{e}(k|k-1)\mathbf{e}^{\mathrm{T}}(k|k-1)] \\ &= E[(\mathbf{x}(k)-\hat{\mathbf{x}}(k|k-1))(\mathbf{x}(k)-\hat{\mathbf{x}}(k|k-1))^{\mathrm{T}}].\end{aligned} \tag{2.17}$$

With the assumption of prior estimate $\hat{\mathbf{x}}(k|k-1)$, the measurement $y(k)$ is employed to improve the prior estimate. An update estimate $\hat{\mathbf{x}}(k|k)$ consists of a linear blending of the noisy measurement and the prior estimate in accordance with the equation

$$\hat{\mathbf{x}}(k|k) = \hat{\mathbf{x}}(k|k-1) + \mathbf{K}(k)(\mathbf{y}(k) - \mathbf{H}\hat{\mathbf{x}}(k|k-1)), \tag{2.18}$$

where $\mathbf{K}(k)$ is a blending factor. To find the particular blending factor $\mathbf{K}(k)$ that yields an update estimate, we use minimum mean square error as the performance criterion. Using Equation (2.14) and Equation (2.18), the error covariance matrix associated with the update estimate is expressed by

$$\mathbf{P}(k|k) = (\mathbf{I} - \mathbf{K}(k)\mathbf{H})\mathbf{P}(k|k-1)(\mathbf{I} - \mathbf{K}(k)\mathbf{H})^{\mathrm{T}} + \mathbf{K}(k)\mathbf{R}(k)\mathbf{K}^{\mathrm{T}}(k). \tag{2.19}$$

It is only necessary to minimize the trace of $\mathbf{P}(k|k)$ because it is the sum of the mean-square errors in the estimates of all the elements of the state vector. Therefore, the trace of $\mathbf{P}(k|k)$ is differentiated with respect to $\mathbf{K}(k)$, and the result is

$$\frac{\mathrm{d}(\mathrm{trace}\mathbf{P}(k|k))}{\mathrm{d}\mathbf{K}(k)} = -2(\mathbf{H}\mathbf{P}(k|k-1))^{\mathrm{T}} + 2\mathbf{K}(k)(\mathbf{H}\mathbf{P}(k|k-1)\mathbf{H}^{\mathrm{T}} + \mathbf{R}(k)). \tag{2.20}$$

The optimal gain is calculated by setting the derivative equal to zero, and the result is

$$\mathbf{K}(k) = \mathbf{P}(k|k-1)\mathbf{H}^{\mathrm{T}}(\mathbf{H}\mathbf{P}(k|k-1)\mathbf{H}^{\mathrm{T}} + \mathbf{R}(k))^{-1}. \tag{2.21}$$

This particular $\mathbf{K}(k)$ is called the Kalman gain which minimizes the mean-square estimation error. Routine substitution of the optimal gain expression, Equation (2.21), into Equation (2.19) leads to

$$\mathbf{P}(k|k) = (\mathbf{I} - \mathbf{K}(k)\mathbf{H})\mathbf{P}(k|k-1). \tag{2.22}$$

Because $\mathbf{w}(k)$ has zero mean and not correlated with any of the previous $\mathbf{w}$'s, the updated estimate $\hat{\mathbf{x}}(k|k)$ is easily projected ahead via the transition matrix as

$$\hat{\mathbf{x}}(k+1|k) = \boldsymbol{\varphi}(k+1|k)\hat{\mathbf{x}}(k|k). \tag{2.23}$$

The error covariance matrix associated with $\hat{\mathbf{x}}(k+1|k)$ is obtained by

$$\mathbf{e}(k+1|k) = \mathbf{x}(k+1) - \hat{\mathbf{x}}(k+1|k) = \boldsymbol{\varphi}(k+1|k)\mathbf{e}(k|k-1) + \mathbf{w}(k). \tag{2.24}$$

$\mathbf{w}(k)$ and $\mathbf{e}(k)$ have zero cross correlation, thus $\mathbf{P}(k+1|k)$ is calculated as

$$\mathbf{P}(k+1|k) = E[\mathbf{e}(k+1|k)\mathbf{e}^{\mathrm{T}}(k+1|k)] = \boldsymbol{\varphi}(k+1|k)\mathbf{P}(k|k-1)\boldsymbol{\varphi}^{\mathrm{T}}(k+1|k) + \mathbf{Q}(k). \tag{2.25}$$

Equations (2.18), (2.21), (2.22), (2.23), and (2.25) comprise the KF recursive equations. It should be clear that once the loop is entered, it can be continued ad infinitum.

Prediction

Extension of the KF to prediction is straightforward. The prediction step in the filter loop is one step prediction. We can use the same identical argument for predicting N steps ahead of the current measurement. The obvious equations for n-step prediction are defined by

$$\hat{\mathbf{x}}(k+n|k) = \boldsymbol{\varphi}(k+n|k)\hat{\mathbf{x}}(k|k), \tag{2.26}$$

$$\mathbf{P}(k+n|k) = \boldsymbol{\varphi}(k+n|k)\mathbf{P}(k|k)\boldsymbol{\varphi}^{\mathrm{T}}(k+n|k) + \mathbf{Q}(k+n), \tag{2.27}$$

where $\hat{\mathbf{x}}(k+n|k)$ is the predivtive estimate of $\mathbf{x}$ at time $k+n$ and $\mathbf{P}(k+n|k)$ is its error covariance. $\hat{\mathbf{x}}(k+n|k)$ and $\mathbf{P}(k+n|k)$ are calculated for ever-increasing prediction times, that is, $n = 1, 2, ..., N$.

Smoothing

'Filtering' and 'Prediction' use past and current observations to predict the current and the future states. While these seem to be sufficient to compute the likelihood of the system, these are suboptimal for estimating the states. In addition to 'Filtering' and 'Prediction', all available data should be employed to estimate the states in the past as well as the future.

Here, we express the fixed-interval smoothing, one of the common smoothing algorithms, which we employ in Chapter 3. The computational procedure for the fixed-interval smoothing consists of a forward recursive sweep followed by a backward sweep. We enter the algorithm as usual at $k = 0$ with the initial conditions $\hat{\mathbf{x}}(0|0)$ and $\mathbf{P}(0|0)$. We then sweep forward using the 'Filtering' and/or 'Prediction'. After completing the forward sweep, backward sweep starts with initial conditions $\hat{\mathbf{x}}(N|N)$ and $\mathbf{P}(N|N)$ obtained as the final computation in the forward sweep. With each step of the backward sweep, the old filter estimate is updated to yield an improved smoothed estimate, which is based on all the measurement data. The recursive equations for the backward sweep are

$$\hat{\mathbf{x}}(k|N) = \hat{\mathbf{x}}(k|k) + \mathbf{A}(k)(\hat{\mathbf{x}}(k+1|N) - \hat{\mathbf{x}}(k+1|k)), \tag{2.28}$$

where the smoothing gain $\mathbf{A}(k)$ is given by

$$\mathbf{A}(k) = \mathbf{P}(k|k)\boldsymbol{\varphi}^{\mathrm{T}}(k+1|k)\mathbf{P}^{-1}(k+1|k), \quad (k = N-1, N-2, ..., 0) \tag{2.29}$$

The error covariance matrix for the smoothed estimates is given by the recursive equation as

$$\mathbf{P}(k|N) = \mathbf{P}(k|k) + \mathbf{A}(k)(\mathbf{P}(k+1|k) - \mathbf{P}(k+1|N))\mathbf{A}^{\mathrm{T}}(k). \tag{2.30}$$

2.2.3 Empirical mode decomposition (EMD) [38, 39]

The empirical mode decomposition (EMD) is a relatively new tool for univariate signal analysis. It is a data-driven method with which any complicated data set, e.g. nonlinear and nonstationary data, can be decomposed into a finite and often small number of 'intrinsic mode functions

(IMFs)' which represent the oscillatory modes contained in the data. The EMD has recently attracted attention from a biosignal processing viewpoint in terms of source separation, detecting EEG synchronization [41], estimating event related potentials (ERPs) [40], and using brain-computer interfaces [42]. In Chapter 3, we apply the EMD to EEG data to extract alpha and beta oscillations.

EMD decomposes a univariate signal $x(t)$ into N IMFs $c_i(t)$ ($i = 1, ..., N$) and a residual signal $r(t)$ as follows:

$$x(t) = \sum_{i=1}^{N} c_i(t) + r(t). \tag{2.31}$$

The IMFs satisfy following two criteria: 1) the number of extrema and the number of zero crossings must either equal or differ at most by one; 2) at any point, the mean values of the envelopes defined by the local maxima and the local minima is zero, and are obtained using the following method:

Step 1 Let $x'(t) = x(t)$.

Step 2 At $x'(t)$, estimate the envelopes: $e_{\mathrm{MAX}}(t)$ for the interpolation between local maxima and $e_{\mathrm{MIN}}(t)$ for the interpolation between local minima.

Step 3 Subtract the mean of the two envelopes from $x'(t)$ as follows:

$$d(t) = x'(t) - \frac{e_{\mathrm{MAX}}(t) + e_{\mathrm{MIN}}(t)}{2}. \tag{2.32}$$

Step 4 If $d(t)$ satisfies the condition of an IMF, $d(t)$ is identified as the IMF $c_i(t)$. If the condition is not satisfied, we set $x'(t) = d(t)$ and repeat the process from **Step 2** until the IMF $c_i(t)$ is found.

Once the IMF $c_i(t)$ is obtained, the same procedure is applied iteratively to the residual $x'(t) = x(t) - \sum_i c_i(t)$ to extract the next IMF $c_{i+1}(t)$. These IMFs are aligned in the order of decreasing frequency, and the last signal is considered to be a residual signal $r(t)$ becomes a monotonic function.

2.3 Time–frequency analysis

2.3.1 Short time Fourier transfrom (STFT) [44, 45, 46]

The STFT is a traditional time–frequency analysis for EEG data [43]. In the analysis, univariate signal is divided into small sequential or overlapping data frames and fast Fourier transform

applied to each one.

The STFT of the univariate signal $x(i)$ (i is a discrete time) is defined as [19-20]:

$$X(i', \omega_k) = e^{-j\omega_k i' R} \sum_{i=-D/2}^{D/2-1} v_n(i + i'R) w(i) e^{-j\omega_k i}, \tag{2.33}$$

where $w(i)$ is a window function, R is a hop size between successive window functions, D is the number of discrete Fourier transform samples (typically a power of 2), $\omega_k = 2\pi k/D$ ($k = 0, 1, ..., D-1$), and k is a discrete index of frequencies. There are various window functions, e.g. the Rectangular window, the Triangular window, the Hamming window, etc. In Chapter 5, we employed the Gaussian window defined as

$$w(i) = \frac{1}{\sqrt{\sigma}\pi^{1/4}} \cdot \exp\left(-\frac{i^2}{2\sigma^2}\right), \tag{2.34}$$

where σ is a fixed parameter which sets the width of the Gaussian window. The main problem with the STFT is that the fixed-duration window function is accompanied by a fixed frequency resolution. Thus, this transform allows only a fixed time–frequency resolution. It is important to note that the frequency resolution of the STFT is defined by the number of samples, not by the number of discrete Fourier transform samples. Increasing the number of discrete Fourier transform samples interpolates the frequency data to provide more details on the spectrum but it does not improve the frequency resolution [46].

2.3.2 Wavelet transform (WT) [47, 48, 49]

The WT has become common time–frequency analysis for EEG data in recent years [50, 51]. The time-frequency resolution obtained by the WT makes it as a good candidate for the extraction of details as well as approximations of the signal which cannot be obtained by the STFT described in 2.3.1. The WT decomposes a signal into a family of wavelets based on a set of basis functions formed by dilation and translation of a prototype mother wavelet $\psi(t)$. The family contains the dilated and translated versions of a mother wavelet, and the dilation of the mother wavelet produces short-duration, high-frequency and long-duration, low-frequency functions.

The complex Morlet wavelet is a good example of a mother wavelet for the construction of the WT and is given by the following function

$$\psi(t) = \frac{1}{\pi^{1/4}} \cdot \exp\left(-\frac{t^2}{2}\right) \cdot \exp(2\pi j f_0 t), \tag{2.35}$$

where f_0 is a central frequency of the mother wavelet, and we set $2\pi f_0 = 7$. To construct dilated Morlet wavelet we replaced t with t/σ_t and normalized Equation (2.35) as

$$\psi(t, f) = \frac{1}{\sqrt{\sigma_t}\pi^{1/4}} \cdot \exp\left(-\frac{t^2}{2{\sigma_t}^2}\right) \cdot \exp(2\pi j f t), \tag{2.36}$$

where σ_t is a scaling parameter, and $f = f_0/\sigma_t$. To compute the WT of the univariate signal $x(t)$, $x(t)$ is convolved with the corresponding complex wavelet as

$$X_n(t, f) = \psi(t, f) * x(t). \tag{2.37}$$

2.3.3 Hilbert-Huang transformation (HHT) [38, 39]

The Hilbert-Huang transform (HHT) consists of the EMD and the Hilbert transform (HT) and is a relatively new time–frequency analysis to catch nonlinear and nonstationary distorted waves in detail. It is well known that the neural signal is mostly nonlinear and nonstationary. However the available methods, e.g. the Fourier based analysis, are not for both nonlinear and nonstationary, their methods have been employed for a long period. The definition of the the traditional Fourier based analysis, the whole signal consists of the sine or cosine function with constant amplitude, would not make sense for non-stationary data. Therefore, the application of conventional approach to nonlinear signals is just not adequate. One of the typical characteristics of nonlinear signals is their intra-wave frequency modulation which indicates the instantaneous frequency changes within one oscillation cycle. Therefore, the HHT attracts attention as an alternative to conventional Fourier based analysis because the HHT seems to extract such instantaneous frequency changes from IMFs $c_i(t)$ decomposed by EMD in 2.2.3. Recently, the applications of the HHT gradually increase in EEG analysis [52, 53].

The Hilbert transform of univariate signal $c_i(t)$, $y(t)$, is given as:

$$y(t) = \frac{1}{\pi} P \int_{-\infty}^{\infty} \frac{c_i(\tau)}{t - \tau} \mathrm{d}\tau, \tag{2.38}$$

where P indicates the Cauchy principal value. The analytic signal is defined as:

$$z(t) = c_i(t) + iy(t) = a(t)e^{i\theta(t)}, \tag{2.39}$$

where

$$a(t) = \sqrt{c_i(t)^2 + y(t)^2}, \quad \text{and} \quad \theta(t) = \arctan\left(\frac{y}{c_i(t)}\right). \tag{2.40}$$

$a(t)$ is the instantaneous amplitude, and $\theta(t)$ is the phase function. Finally, the instantaneous frequency of $c_i(t)$ is calculated as:

$$\omega(t) = \frac{\mathrm{d}\theta}{\mathrm{d}t}. \tag{2.41}$$

2.4 Multivariate analysis

2.4.1 Principal component analysis (PCA) [54]

The central idea of principle component analysis (PCA) is to reduce the dimension of a data set consisting of a large number of interrelated variables, while retaining as much as possible of the

variation present in the data set. An alternative approach of PCA is to seek a few derived components, representing most of information given by these variances, from multivariate signals. PCA is universally used process for feature extraction, dimension reduction, data compression, etc., and sometimes used for a signal noise separation in EEG analysis. In Chapters 3 and 4, we use PCA to reduce dimension of EEG data as a preprocessing.

When $v_n(t)$ denotes one of multivariate ($n = 1, ..., N$, N is the number of variates) signal, the multivariate signal is defined as a following vector:

$$\mathbf{v}(t) = \begin{bmatrix} v_1(t) \\ v_2(t) \\ \vdots \\ v_N(t) \end{bmatrix}. \tag{2.42}$$

The first step to derive PCs is to seek a linear function $\mathbf{u}_1\mathbf{v}(t)$, and the vector $\mathbf{u}_1$ maximizes variance of $\mathbf{u}_1\mathbf{v}(t)$. Using a known covariance matrix $\mathbf{C}$ of $\mathbf{v}(t)$, the variance of $\mathbf{u}_1\mathbf{v}(t)$ is given as $\mathbf{u}_1^{\mathrm{T}}\mathbf{C}\mathbf{u}_1$. Assuming $\langle \mathbf{v}(t) \rangle_t \approx 0$ ($\langle\ \rangle_t$ denotes a time average), the covariance matrix $\mathbf{C}$ is defined as:

$$\mathbf{C} = \langle \mathbf{v}(t)\mathbf{v}^{\mathrm{T}}(t) \rangle_t = \begin{bmatrix} \langle v_1^2(t) \rangle_t & \langle v_1(t)v_2(t) \rangle_t & \cdots & \langle v_1(t)v_N(t) \rangle_t \\ \langle v_2(t)v_1(t) \rangle_t & \langle v_2^2(t) \rangle_t & \cdots & \langle v_2(t)v_N(t) \rangle_t \\ \vdots & \vdots & \ddots & \vdots \\ \langle v_N(t)v_1(t) \rangle_t & \langle v_N(t)v_2(t) \rangle_t & \cdots & \langle v_N^2(t) \rangle_t \end{bmatrix}. \tag{2.43}$$

To avoid $|\mathbf{u}_1| \to 0$, a normalization constraint, $\mathbf{u}_1^{\mathrm{T}}\mathbf{u}_1 = 1$, must be imposed. To maximize $\mathbf{u}_1^{\mathrm{T}}\mathbf{C}\mathbf{u}_1$ constrained to $\mathbf{u}_1^{\mathrm{T}}\mathbf{u}_1 = 1$, the technique of Lagrange's method of undetermined multipliers is employed. Then, maximize

$$\mathbf{u}_1^{\mathrm{T}}\mathbf{C}\mathbf{u}_1 + \lambda_1 \left(\mathbf{u}_1^{\mathrm{T}}\mathbf{u}_1 \right), \tag{2.44}$$

where λ_1 is a Largrange multiplier. Set differentiation with respect to $\mathbf{u}_1$ to zero,

$$\mathbf{C}\mathbf{u}_1 = \lambda_1\mathbf{u}_1. \tag{2.45}$$

This equation means $\mathbf{u}_1$ is an eigenvector of $\mathbf{C}$ and λ_1 is the corresponding eigenvalue. Moreover, $\mathbf{u}_1^{\mathrm{T}}$ is multiplied with the left side of Equation (2.45), given as:

$$\mathbf{u}_1^{\mathrm{T}}\mathbf{C}\mathbf{u}_1 = \mathbf{u}_1^{\mathrm{T}}\lambda_1\mathbf{u}_1 = \lambda_1. \tag{2.46}$$

As a results, $\mathbf{u}_1$ is the eigenvector corresponding to the largest eigenvalue of $\mathbf{C}$ and λ_1 is the largest eigenvalue. In addition, the kth PC of $\mathbf{v}(t)$ is $\mathbf{u}_k^{\mathrm{T}}\mathbf{C}$, $\mathbf{u}_k$ is the eigenvector corresponding to λ_k which is the variance of $\mathbf{u}_k^{\mathrm{T}}\mathbf{C}$ and the kth largest eigenvalue of $\mathbf{C}$.

There is an index which shows the proportion of the mth PC in $\mathbf{v}(t)$ shown as:

$$P_m = \frac{\lambda_m}{\sum_{j=1}^{M} \lambda_j}. \tag{2.47}$$

Furthermore, there is the other index which shows the proportion of total variation accounted for by the first mth PCs as:

$$\mathrm{CP}_m = \sum_{j=1}^{m} P_j. \tag{2.48}$$

CP_m is called a cumulative proportion. In general, most obvious criterion for choosing m is to select the cumulative proportion as 80% or 90%.

2.4.2 Independent component analysis (ICA) [55, 56]

PCA described in 2.4.1 is an only decorrelation method, and incapable of separating independent sources. On the other hand, independent component analysis (ICA) not only decorrelates the signals but also reduces higher order statistical dependence to recover independent sources. ICA is known to be effective in performing source separation under a certain condition that the time courses of the sources are independent. In Chapter 3, we utilize ICA as a means to separate EEG data contaminated by ocular artifacts to clean and contaminated independent components (ICs) because the source of ocular activities are not generally time locked to the sources of cortical neurons activities.

Assuming that there is an M-variate zero-mean signals $\mathbf{s}(t) = [s_1(t), ..., s_M(t)]^{\mathrm{T}}$ where $s_i(t)$ are mutually independent ($i = 1, ..., M$), the multivariate probability density function (PDF) of $s_i(t)$ is given as the product of marginal independent distributions.

$$p(\mathbf{s}(t)) = \prod_{i=1}^{M} p_i(s_i(t)). \tag{2.49}$$

An N-variate signal $\mathbf{v}(t)$ is observed, such that

$$\mathbf{v}(t) = \mathbf{A}\mathbf{s}(t), \tag{2.50}$$

where $\mathbf{A}$ is a full rank $N \times M$ matrix. The goal of ICA is to find a linear transformation matrix $\mathbf{W}$ of the dependent observed signal $\mathbf{x}(t)$. $\mathbf{W}$ makes the estimate of the source $\mathbf{s}(t)$, $\hat{\mathbf{s}}(t)$, as independent as possible

$$\hat{\mathbf{s}}(t) = \mathbf{W}\mathbf{v}(t). \tag{2.51}$$

In this case, we summarized the derivation of the infomax approach for ICA which was employed in the proposed ocular artifacts removal method in Chapter 3. From here, we abbreviate time denotation t to simplify following descriptions. Consider monotonically transformed output vector such as $\mathbf{y} = g(\mathbf{u})$, $\mathbf{u} = \mathbf{W}\mathbf{v} + \mathbf{w}_0$ where $g(\ )$ is a nonlinear transfer function, $\mathbf{w}_0$ is a

bias vector. The nonlinear mapping between the output density $p(\mathbf{y})$ and input density $p(\mathbf{v})$ can be described by the Jacobian

$$p(\mathbf{y}) = \frac{p(\mathbf{v})}{|\mathbf{J}(\mathbf{v})|}. \tag{2.52}$$

The Jacobian $\mathbf{J}(\mathbf{v})$ is the determinant of the matrix of partial derivatives:

$$\mathbf{J}(\mathbf{v}) = \det \begin{bmatrix} \frac{\partial y_1}{\partial v_1} & \cdots & \frac{\partial y_1}{\partial v_n} \\ \vdots & \ddots & \vdots \\ \frac{\partial y_n}{\partial v_1} & \cdots & \frac{\partial y_n}{\partial v_n} \end{bmatrix}, \tag{2.53}$$

where y_i $(i = 1, ..., N)$ is a component of $\mathbf{y} = [y_1(t), ..., y_N(t)]^{\mathrm{T}}$. Each partial derivative has the following form

$$\frac{\partial y_i}{\partial v_j} = w_{ij} \frac{\partial y_i}{\partial u_j}. \tag{2.54}$$

Because there is no connections between the outputs of the source, $\frac{\partial y_i}{\partial u_j}$ is non-zero for $i = j$ only. Therefore,

$$\mathbf{J}(\mathbf{v}) = \det(\mathbf{W}) \prod_{i=1}^{N} \left| \frac{\partial y_i}{\partial u_i} \right|. \tag{2.55}$$

The learning rule of Infomax can be derived by maximizing the output entropy $H(\mathbf{y})$. $H(\mathbf{y})$ is written as:

$$H(\mathbf{y}) = -E\left[\ln p(\mathbf{y})\right] = E\left[\ln \mathbf{J}(\mathbf{v})\right] - E\left[\ln p(\mathbf{v})\right], \tag{2.56}$$

where $E[\ ]$ calculates an expectation. Then, the stochastic learning rule can be approximated without the expectation termas follows.

$$\frac{\partial H(\mathbf{y})}{\partial \mathbf{W}} = \frac{\partial}{\partial \mathbf{W}} \ln |\mathbf{J}(\mathbf{v})| = \frac{\partial}{\partial \mathbf{W}} \left| \det(\mathbf{W}) \right| + \frac{\partial}{\partial \mathbf{W}} \ln \prod_{i=1}^{N} \left| \frac{\partial y_i}{\partial u_i} \right|. \tag{2.57}$$

In addition,

$$\frac{\partial}{\partial \mathbf{W}} \left| \det(\mathbf{W}) \right| = \frac{(\mathrm{adj}\mathbf{W})^{\mathrm{T}}}{\det(\mathbf{W})} = \left(\mathbf{W}^{\mathrm{T}}\right)^{-1}, \tag{2.58}$$

where adj means an adjugate matrix, and

$$\frac{\partial}{\partial \mathbf{W}} \prod_{i=1}^{N} \left| \frac{\partial y_i}{\partial u_i} \right| = \sum_{i=1}^{N} \frac{\partial}{\partial \mathbf{W}} \ln \left| \frac{\partial y_i}{\partial u_i} \right| = \frac{\frac{\partial p(\mathbf{u})}{\partial \mathbf{u}}}{p(\mathbf{u})} \mathbf{v}^{\mathrm{T}}. \tag{2.59}$$

Finally, Equation (2.57) are computed and the learning infomax rule is

$$\frac{\partial H(\mathbf{y})}{\partial \mathbf{W}} = \left(\mathbf{W}^{\mathrm{T}}\right)^{-1} + \frac{\frac{\partial p(\mathbf{u})}{\partial \mathbf{u}}}{p(\mathbf{u})} \mathbf{v}^{\mathrm{T}}. \tag{2.60}$$

This learning rule is a result of the gradient of the entropy function and involves a computationally intensive matrix inversion.

2.4.3 Multivariate Empirical mode decomposition (MEMD) [57]

In EMD described in 2.2.3, the oscillatory mode (IMF) is obtained by subtracting the average of the upper and lower envelopes from the original signal. However, the upper and lower envelopes are calculated by interpolating between the local maxima and minima in EMD, and the local maxima and minima may not be defined directly for multivariate signals. Therefore, Rehman and Mandic [57] proposed a method for calculating the local means for multivariate signals which can be considered to be an approximation of the integral of all the envelopes along multiple directions in the *n*-dimensional space. We applied MEMD to multi-channel recorded EEG data to extract alpha band ERD/ERS in Chapter 5.

When $b = (b_1, ..., b_n, ..., b_N)$ is the first N prime sets, where N is the number of variables of the original signals denoted by $\mathbf{u}(t) = [u_1(t), ..., u_n(t), ..., u_N(t)]$, the ith sample of a one-dimensional Halton sequence denoted by r_i^b is given by

$$r_i^b = \frac{a_0}{b} + \frac{a_1}{b^2} + \frac{a_2}{b^3} + \cdots + \frac{a_s}{b^{s+1}}, \tag{2.61}$$

where the base-b representation of i is given by

$$i = a_0 + a_1 \times b + a_2 \times b^2 + \cdots + a_s \times b^s. \tag{2.62}$$

Then, the ith sample of the Halton sequence $\mathbf{r}_i$ becomes

$$\mathbf{r}_i = \left[r_i^{b_1}, \ldots, r_i^{b_n}, \ldots, r_i^{b_N} \right]. \tag{2.63}$$

Therefore, the ith direction vector in n-dimensional spaces is given by normalization of Equation (2.63) as

$$\hat{\mathbf{r}}_i = \frac{\mathbf{r}_i}{|\mathbf{r}_i|}. \tag{2.64}$$

After the direction vectors are obtained, n-variate original signals are projected onto the direction vectors. Then, the n-variate IMFs of original signals are calculated by the iterative process (called sifting process) of MEMD as follows:

Step 1 Calculate the direction vectors $\hat{\mathbf{r}}_i$ in n-dimensional spaces for all i (the whole I set of direction vectors) of the Halton sequence.

Step 2 Calculate projected signals denoted by $\tilde{\mathbf{u}}_i(t)$ of the original signal $\mathbf{u}(\mathbf{t})$ along the direction vector $\hat{\mathbf{r}}_i$ for all i.

Step 3 Find the time instants $\{t_i^l\}$ corresponding to the local maxima of the set of projected signals $\tilde{\mathbf{u}}_i(t)$ for all i. The number of obtained time instants l is varied, depending on the direction vectors $\hat{\mathbf{r}}_i$.

Step 4 Interpolate $\left[t_i^l, \mathbf{u}(t_i^l)\right]$ to obtain multivariate envelopes $\mathbf{e}_i(t)$ for all i.

Step 5 Calculate the mean envelope $\mathbf{m}(t)$ as

$$\mathbf{m}(t) = \frac{1}{I}\sum_{i=1}^{I} \mathbf{e}_i(t) \tag{2.65}$$

Step 6 Extract the detail $\mathbf{d}(t) = \mathbf{u}(t) - \mathbf{m}(t)$. If $\mathbf{d}(t)$ fulfils both conditions of IMF described in 2.2.3, $\mathbf{d}(t)$ is the multivariate IMF set, and apply the above procedure to $\mathbf{u}(t) = \mathbf{u}(t) - \mathbf{d}(t)$. Otherwise, apply it to $\mathbf{d}(t)$ again.

References

[1] Kandel, E. R., Schwartz, J. H., & Jessell, T. M. (2000). Principles of neural science, 4th, McGraw-Hill.

[2] Steriade, M. (2001). The intact and sliced brain. MIT press.

[3] Schomer, D. L., & Da Silva, F. L. (2012). Niedermeyer's electroencephalography: basic principles, clinical applications, and related fields. Lippincott Williams & Wilkins.

[4] Cacioppo, J. T., Tassinary, L. G., & Berntson, G. (2007). Handbook of psychophysiology. Cambridge University Press.

[5] Caton, R. (1875). Electrical currents of the brain. The Journal of Nervous and Mental Disease, 2(4), 610.

[6] Prawdicz-Neminski, N.W. (1913) Elektrische Gehirnerscheinungen. Zentralbl Physiol, 18, 951–960.

[7] Berger, H. (1929). Über das Elektrenkephalogramm des Menschen. Archiv fur Psychiatrie und Nervenkrankheiten , 87, 527–570.

[8] Luck, S. J. (2005). An introduction to the event-related potential technique. MIT press.

[9] Binder, M. D., & Hirokawa, N. (2009). Encyclopedia of neuroscience. Springer.

[10] Niedermeyer, E., & da Silva, F. L. (2005). Electroencephalography: basic principles, clinical applications, and related fields. Lippincott Williams & Wilkins.

[11] Polich, J. (2007). Updating P300: an integrative theory of P3a and P3b. Clinical Neurophysiology, 118(10), 2128–2148.

[12] Davis, H., Davis, P.A., Loomis, A.L., Harvey, N., & Hobart, G.A. (1939) Electrical reactions of the brain to auditory stimulation during sleep. Journal of Neurophysiology, 2, 500–514.

[13] Walter, W. G., Cooper R., Aldridge, V. J., McCallum, W. C., & Winter, A. L. (1964). Contingent negative variation: An electric sign of sensorimotor association and expectancy in the human brain. Nature, 203, 380–384.

[14] Sutton, S., Braren, M., Zubin, J., & John, E. R. (1965). Evoked-potential correlates of stimulus uncertainty. Science, 150(3700), 1187–1188.

[15] Ritter, W., & Vaughan, H. G. (1969). Averaged evoked responses in vigilance and discrimination: A reassessment. Science, 164(3877), 326–328.

[16] Polich, J., & Criado, J. R. (2006). Neuropsychology and neuropharmacology of P3a and P3b. International Journal of Psychophysiology, 60(2), 172–185.

[17] Polich, J., & Kok, A. (1995). Cognitive and biological determinants of P300: an integrative review. Biological Psychology, 41(2), 103–146.

[18] Patterson, J. V., Michalewski, H. J., & Starr, A. (1988). Latency variability of the components of auditory event-related potentials to infrequent stimuli in aging, Alzheimer-type dementia, and depression. Electroencephalography and Clinical Neurophysiology/Evoked Potentials Section, 71(6), 450–460.

[19] Pfurtscheller, G., & Lopes da Silva, F. H. (1999). Event-related EEG/MEG synchronization and desynchronization: basic principles. Clinical Neurophysiology, 110(11), 1842–1857.

[20] Klimesch, W., Sauseng, P., & Hanslmayr, S. (2007). EEG alpha oscillations: the inhibition-timing hypothesis. Brain Research Reviews, 53(1), 63–88.

[21] Pfurtscheller, G. (2001). Functional brain imaging based on ERD/ERS. Vision Research, 41(10), 1257–1260.

[22] Adrian, E.D., & Matthews B.H.C. (1934). The Berger rhythm: Potential changes from the occipital lobes in man. Brain, 57, 355–385.

[23] Jung, T. P., Makeig, S., WesterReld, M., Townsend, M. J., Courchesne. E., & Sejnowski, T. J. (2000). Removal of eye activity artifacts from visual event-related potentials in normal and clinical subjects. Clinical Neurophysiology, 111, 1745–1758

[24] Jung, T. P., Makeig, S., Humphries, C., Lee, T. W., Mckeown, M. J., Iragui, V., & Sejnowski, T. J (2000). Removing electroencephalographic artifacts by blind source separation. Psychophysiology, 37, 163–178

[25] Başar, E., Demiralp, T., Schürmann, M., Başar-Eroglu, C., & Ademoglu, A. (1999). Oscillatory brain dynamics, wavelet analysis, and cognition. Brain and language, 66(1), 146–183.

[26] Intriligator, J., & Polich, J. (1994). On the relationship between background EEG and the P300 event-related potential. Biological psychology, 37(3), 207–218.

[27] Kobayashi, T., & Kuriki, S. (1999). Principal component elimination method for the improvement of S/N in evoked neuromagnetic field measurements. Biomedical Engineering, IEEE Transactions on, 46(8), 951–958.

[28] Hu, L., Mouraux, A., Hu, Y., & Iannetti, G. D. (2010). A novel approach for enhancing the signal-to-noise ratio and detecting automatically event-related potentials (ERPs) in single trials. Neuroimage, 50(1), 99–111.

[29] Kirchgässner, G., Wolters, J., & Hassler, U. (2012). Introduction to modern time series analysis. Springer.

[30] Jansen, B. H., Bourne, J. R., & Ward, J. W. (1981). Autoregressive estimation of short segment spectra for computerized EEG analysis. Biomedical Engineering, IEEE Transactions on, 28(9), 630–638.

[31] Wright, J. J., Kydd, R. R., & Sergejew, A. A. (1990). Autoregression models of EEG. Biological cybernetics, 62(3), 201–210.

[32] Akaike, H. (1969). Fitting autoregressive models for prediction. Annals of the Institute of Statistical Mathematics, 21, 243–247.

[33] Haykin, S. (2001). Kalman filtering and neural networks. John Wiley & Sons, Inc.

[34] Moreno, V. M., & Pigazo, A. (2009). Kalman filter: recent advances and applications. InTech.

[35] Brown, R. G., & Hwang, P. Y. C. (2012). Introduction to random signals and applied Kalman filtering: with MATLAB exercises. 4th ed. John Wiley & Sons, Inc.

[36] Tarvainen, M. P., Hiltunen, J. K., Ranta-aho, P. O., & Karjalainen, P. A. (2004). Estimation of nonstationary EEG with Kalman smoother approach: an application to event-related synchronization (ERS). Biomedical Engineering, IEEE Transactions on, 51(3), 516–524.

[37] Georgiadis, S. D., Ranta-aho, P. O., Tarvainen, M. P., & Karjalainen, P. A. (2005). Single-trial dynamical estimation of event-related potentials: a Kalman filter-based approach. Biomedical Engineering, IEEE Transactions on, 52(8), 1397–1406.

[38] Huang, N. E., Shen, Z., Long, S. R., Wu, M. C., Shih, H. H., Zheng, Q., ... & Liu, H. H. (1998). The empirical mode decomposition and the Hilbert spectrum for nonlinear and non-stationary time series analysis. Proceedings of the Royal Society of London. Series A: Mathematical, Physical and Engineering Sciences, 454(1971), 903–995.

[39] Huang, N. E., Shen, Z., & Long, S. R. (1999). A new view of nonlinear water waves: The Hilbert Spectrum 1. Annual Review of Fluid Mechanics, 31(1), 417–457.

[40] Williams, N., Nasuto, S. J., & Saddy, J. D. (2011). Evaluation of empirical mode decomposition for event-related potential analysis. EURASIP Journal on Advances in Signal Processing, 2011, 11 pages.

[41] Sweeney-Reed, C. M., & Nasuto, S. J. (2007). A novel approach to the detection of synchronisation in EEG based on empirical mode decomposition. Journal of Computational Neuroscience, 23(1), 79–111.

[42] Shi, Q., Zhou, W., Cao, J., Tanaka, T., & Wang, R. (2010). Brain-computer interface system using approximate entropy and EMD techniques. In Advances in Swarm Intelligence, 6146, 204–212.

[43] Sanei, S., & Chanbers, J. A. (2008). EEG signal processing. John Wiley & Sons, Ltd.

[44] Smith, J. O. (2011). Spectral audio signal processing. W3K Publishing.

[45] Oppenheim, A. V., Schafer, R. W., & Buck, J. R. (1989). Discrete-time signal processing (Vol. 2). Prentice-Hall.

[46] Proakis, J. G., & Manolakis, D. G. (1995). Digital Signal Processing: Principles, Algorithms and Applications. Prentice-Hall .

[47] Addison, P. S. (2002). The illustrated wavelet transform handbook: introductory theory and applications in science, engineering, medicine and finance. CRC Press.

[48] Najmi, A. H., & Sadowsky, J. (1997). The continuous wavelet transform and variable resolution time-frequency analysis. Johns Hopkins APL Technical Digest, 18(1), 134–140.

[49] Tse, N. C., & Lai, L. L. (2007). Wavelet-based algorithm for signal analysis. EURASIP Journal on Applied Signal Processing, 2007(1), 169–169.

[50] Neuper, C., & Pfurtscheller, G. (2001). Evidence for distinct beta resonance frequencies in human EEG related to specific sensorimotor cortical areas. Clinical Neurophysiology, 112(11), 2084–2097.

[51] Muthukumaraswamy, S. D., & Johnson, B. W. (2004). Primary motor cortex activation during action observation revealed by wavelet analysis of the EEG. Clinical Neurophysiology, 115(8), 1760–1766.

[52] Oweis, R. J., & Abdulhay, E. W. (2011). Seizure classification in EEG signals utilizing Hilbert-Huang transform. BioMedical Engineering OnLine, 10(38), 15 pages.

[53] Pigorini, A., Casali, A. G., Casarotto, S., Ferrarelli, F., Baselli, G., Mariotti, M., ... & Rosanova, M. (2011). Time–frequency spectral analysis of TMS-evoked EEG oscillations by means of Hilbert-Huang transform. Journal of neuroscience methods, 198(2), 236–245.

[54] Jolliffe, I. T. (2005). Principal component analysis. John Wiley & Sons, Ltd.

[55] Lee, T. W. (1998). Independent component analysis. Springer.

[56] Bell, A. J., & Sejnowski, T. J. (1995). An information-maximization approach to blind separation and blind deconvolution. Neural computation, 7(6), 1129–1159.

[57] Rehman, N., & Mandic, D. P. (2010). Multivariate empirical mode decomposition. Proceedings of the Royal Society A: Mathematical, Physical and Engineering Science, 466(2117), 1291–1302.

Chapter 3

Ocular artifacts removal for EEG

In EEG analysis, removal of ocular artifacts is important to reduce measurement time and increase SNR of ERPs and ERS/ERD. Although various methods for removing the ocular artifacts had been reported, they removed a part of the original EEGs together with ocular artifacts. In this chapter, we focused mainly on the extent to which the true EEGs are retained and proposed a localized removal method for ocular artifacts. The method is based on a combination of EMD with ICA and the Kalman filter. To validate the performance of the proposed method, we assessed information loss using pseudo-EEGs consisting of the ideal artifacts-free EEGs and five types of ocular artifacts (an eye-blink and four eye-movements: up, down, left, and right) simulated by two equivalent current dipoles with a single-sphere head model. The results confirmed that the proposed method successfully removed the ocular artifacts and reduced information loss of ideal EEGs. Here, 'true and/or ideal' represents 'not include any artifacts'.

3.1 Background

One of the most popular methods used to remove ocular artifacts is based on ICA, which assumes that several ICs reflect ocular artifacts [1, 2, 3, 4, 5, 6]. The ICA algorithm is highly effective at performing source separation. The previous studies using ICA were mainly intended to identify ICs reflecting ocular artifacts [4, 5, 7], whereas some of the ideal EEGs may also be concurrently removed. Additionally, with an increase in the number and type of ocular artifacts in a single trial, the number of ICs representing those ocular artifacts that may be extracted by the previous methods based on ICA also increases [4, 8]. Nevertheless, little attention has been given to these issue.

In the study on the removal of ocular artifacts, there are few quantitative assessment methods for validation because there is no access to the ideal EEGs in experimental data. There is, therefore, no quantitative criterion against which the performance of a removal method [6, 9, 10, 11] can be based. Hence, Lindsen and Bhattacharya [6] attempted to simulate signals both with and without an eye-blink artifact, and assessed the removal method using the correlation

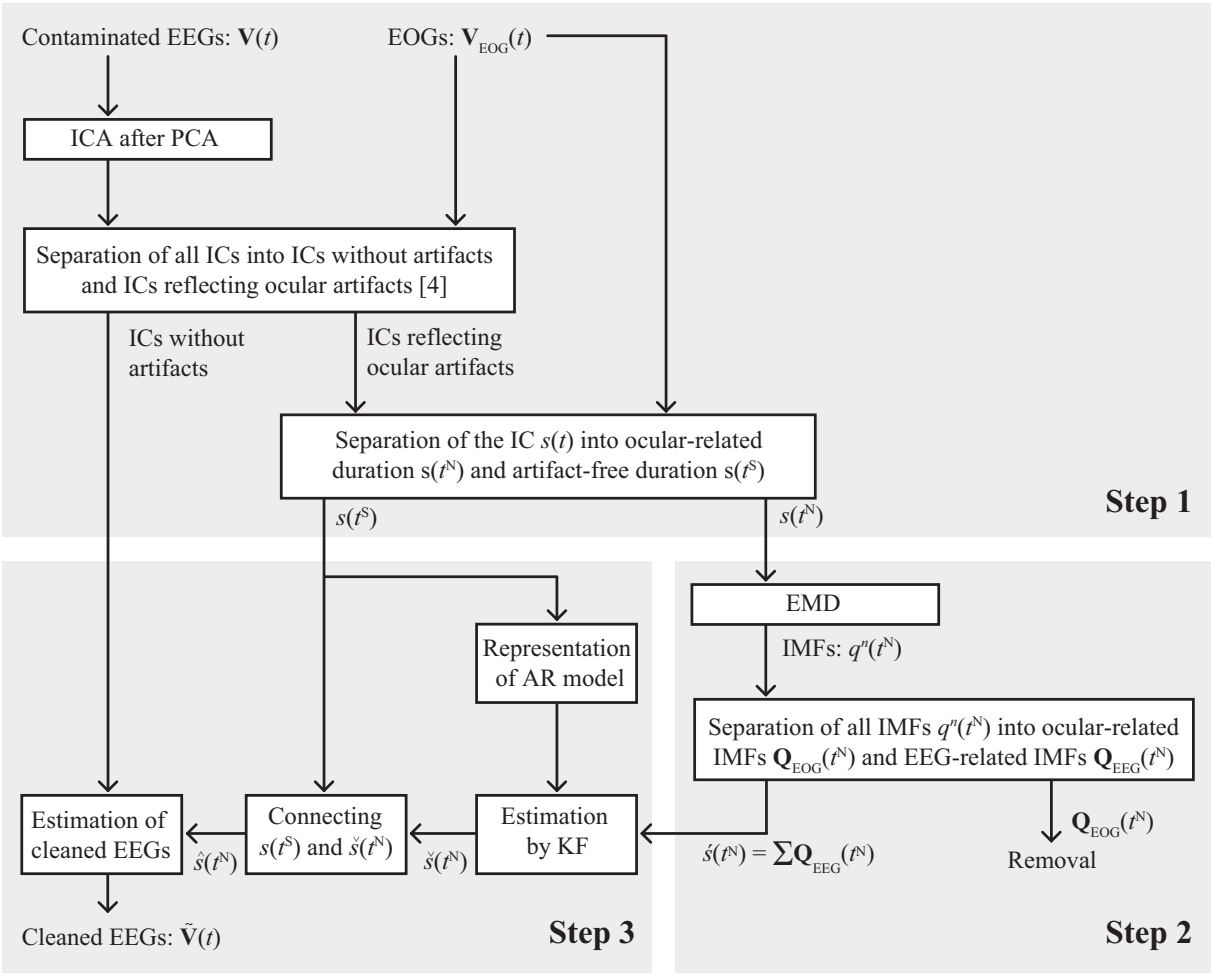

Figure 3.1: Flow chart of the proposed method.

coefficient (CC) between the ideal and cleaned signals. However, their assessment method targeted only on ICA-based removal methods, and the CC assessed the similarity but not the coincidence between the two signals.

3.2 A locally restricted ocular artifact removal method

We focused mainly on the extent to which the true EEGs are retained and proposed a localized removal method for ocular artifacts. The proposed method consists of the following three steps (Figure 3.1).

Step 1 Using ICA (Infomax algorithm) after reducing the dimensions by applying PCA, the measured EEGs $\mathbf{V}(t)$ ($t = 0 - T$ ms) were decomposed into ICs, and the time courses of J ICs ($s^j(t)$, $j = 1, 2, \cdots J$) were identified, reflecting ocular artifacts [4]. Here, we

employed PCA to prevent the estimation error of ICs known as the overlearning and the minimum number of PCs whose cumulative contribution exceeded 90%, which seemed to adequately explain the original data, were extracted. $s^j(t)$ was calculated as follows:

$$s^j(t) = \mathbf{w}^j \mathbf{V}(t) \tag{3.1}$$

where $\mathbf{w}^j$ was a vector corresponding to the jth IC. Hereafter, $s^j(t)$ is abbreviated as $s(t)$ because all $s^j(t)$ are processed in the same way. The correlation between $s(t)$ and the measured EOGs $\mathbf{V}_{\mathrm{EOG}}(t)$ was assessed. Then, for $s(t)$, the duration for which the correlation is greater than 0.6 is considered to be an ocular duration t^{N}, whereas the remaining duration is considered to be a noise-free duration t^{S}. Here, the threshold of 0.6 was determined by trial and error. If the threshold was smaller than 0.6, $s(t^{\mathrm{N}})$ seemed to include much noise-free signal.

Step 2 Using EMD, $s(t^{\mathrm{N}})$ was decomposed into a set of N intrinsic mode functions (IMFs) $q^n(t^{\mathrm{N}})$ ($n = 1, 2, \cdots, N$) and the residual signal $r(t^{\mathrm{N}})$, as follows:

$$s(t^{\mathrm{N}}) = \sum_{n=1}^{N} q^n(t^{\mathrm{N}}) + r(t^{\mathrm{N}}) \tag{3.2}$$

The IMFs satisfy following two criteria [12]: 1) the number of extrema and the number of zero crossings must either equal or differ at most by one; 2) at any point, the mean values of the envelopes defined by the local maxima and the local minima is zero, and are obtained using the following method:

1. Let $s'(t^{\mathrm{N}}) = s(t^{\mathrm{N}})$.
2. At $s'(t^{\mathrm{N}})$, estimate the envelopes: $e_{\mathrm{MAX}}(t^{\mathrm{N}})$ for the interpolation between local maxima and $e_{\mathrm{MIN}}(t^{\mathrm{N}})$ for the interpolation between local minima.
3. Subtract the mean of the two envelopes from $s'(t^{\mathrm{N}})$ as follows:

$$d(t^{\mathrm{N}}) = s'(t^{\mathrm{N}}) - \frac{[e_{\mathrm{MAX}}(t^{\mathrm{N}}) + e_{\mathrm{MIN}}(t^{\mathrm{N}})]}{2}. \tag{3.3}$$

4. If $d(t^{\mathrm{N}})$ satisfies the condition of an IMF, $d(t^{\mathrm{N}})$ is identified as the IMF $q^n(t^{\mathrm{N}})$. If the condition is not satisfied, we set $s'(t^{\mathrm{N}}) = d(t^{\mathrm{N}})$ and repeat the process from 2. until the IMF $q^n(t^{\mathrm{N}})$ is found.

Once the IMF $q^n(t^{\mathrm{N}})$ is obtained, the same procedure is applied iteratively to the residual $s'(t^{\mathrm{N}}) = s(t^{\mathrm{N}}) - \sum_n q^n(t_{\mathrm{N}})$ to extract the next IMF $q^{n+1}(t^{\mathrm{N}})$. These IMFs are aligned in the order of decreasing frequency, and the last signal is considered to be a residual signal $r(t_{\mathrm{N}})$ becomes a monotonic function. Next, the ocular-related IMFs that reflected ocular

artifacts were identified from the set of IMFs $\mathbf{Q}(t^{\mathrm{N}}) = \{q^1(t^{\mathrm{N}}), q^2(t^{\mathrm{N}}), \cdots, q^N(t^{\mathrm{N}})\}$ by comparing standard deviations (std) of $q^n(t^{\mathrm{N}})$ and $s(t^{\mathrm{S}})$. Here, if $q^n(t^{\mathrm{N}})$ satisfies the following condition:

$$\mathrm{std}[q^n(t^{\mathrm{N}})] > u \cdot \mathrm{std}[s(t^{\mathrm{S}})], \tag{3.4}$$

where std [ ] calculates the standard deviation, $q^n(t^{\mathrm{N}})$ is treated as a ocular-related IMF, if not, a EEG-related IMF. u is a multiplication factor that determines the upper limit of acceptable standard deviations in the classification of the IMF. Therefore, the set of IMFs $\mathbf{Q}(t^{\mathrm{N}})$ is divided into two groups: the set of ocular-related IMFs $\mathbf{Q}_{\mathrm{EOG}}(t^{\mathrm{N}})$; and the set of EEG-related IMFs $\mathbf{Q}_{\mathrm{EEG}}(t^{\mathrm{N}})$. Then, the term $\acute{s}(t^{\mathrm{N}})$ which is an artifact-free $s(t^{\mathrm{N}})$ is reconstructed by summing all EEG-related IMFs $\mathbf{Q}_{\mathrm{EEG}}(t^{\mathrm{N}})$ as follows:

$$\acute{s}(t^{\mathrm{N}}) = \sum \mathbf{Q}_{\mathrm{EEG}}(t^{\mathrm{N}}) \tag{3.5}$$

Step 3 This step attempts to make $\hat{s}(t)$, which is the time courses of cleaned ICs by connecting $s(t^{\mathrm{S}})$ and $\acute{s}(t^{\mathrm{N}})$. However, $s(t^{\mathrm{S}})$ and $\acute{s}(t^{\mathrm{N}})$ cannot be directly connected because a part of information in $\acute{s}(t^{\mathrm{N}})$ is lost by the removal of the IMFs in **Step 2**. Therefore, we adopted the KF to connect $s(t^{\mathrm{S}})$ and $\acute{s}(t^{\mathrm{N}})$ smoothly.

After representing the AR model of $s(t^{\mathrm{S}})$ in the state-space model, $\check{s}(t)$ obeying the AR model of $s(t^{\mathrm{S}})$ was estimated by both the KF and the fixed-interval smoothing [13, 14, 15]. The order of the AR model was determined by the minimization of Akaike's information criteria (AIC) [16]. It is assumed that changes in the AR parameters of $s(t^{\mathrm{S}})$ were sufficiently smaller than those of $s(t^{\mathrm{S}})$ and $\acute{s}(t^{\mathrm{N}})$, i.e., the AR model of $s(t^{\mathrm{S}})$ was a time-invariant system. The AR model of $s(t^{\mathrm{S}})$ is given as follows [17]:

$$s(t^{\mathrm{S}} + 1) = \sum_{i=1}^{I} a_i s(t^{\mathrm{S}} - i) + v(t^{\mathrm{S}}) \tag{3.6}$$

where I is the order of the model, a_i is the the time-invariant AR parameter, and $v(t^{\mathrm{S}})$ is the state noise at time t^{S} with zero mean and variance q_{s}. By denoting

$$\mathbf{x}(t^{\mathrm{S}}) = \left[s(t^{\mathrm{S}} - 1), \ldots, s(t^{\mathrm{S}} - I)\right]^{\mathrm{T}} \tag{3.7}$$

the state-space model based on the AR model is given as follows [13, 14]:

$$\mathbf{x}(t^{\mathrm{S}}) = \boldsymbol{\phi}\mathbf{x}(t^{\mathrm{S}} - 1) + \mathbf{g}w(t^{\mathrm{S}}) \tag{3.8}$$

$$s(t^{\mathrm{S}}) = \mathbf{h}\mathbf{x}(t^{\mathrm{S}}) + v(t^{\mathrm{S}}) \tag{3.9}$$

where

$$\boldsymbol{\phi} = \begin{bmatrix} a_1 & a_2 & \cdots & a_I \\ 1 & & & \\ & \ddots & & \\ & & 1 & 0 \end{bmatrix}, \quad \mathbf{g} = \begin{bmatrix} 1 \\ 0 \\ \vdots \\ 0 \end{bmatrix}, \quad \mathbf{h} = \begin{bmatrix} 1 & 0 & \cdots & 0 \end{bmatrix}, \tag{3.10}$$

$\mathbf{x}(t^{\mathrm{S}})$ is a process state vector at time t^{S}, and $w(t^{\mathrm{S}})$ is the measurement noise at time t^{S} with zero mean and variance q_{o} and having zero cross correlation with the $v(t^{\mathrm{S}})$ sequence.

Next, $\mathbf{x}(t)$ was estimated from the observations, $s(t_{\mathrm{S}})$ and $\acute{s}(t_{\mathrm{N}})$ using the KF. The priori estimate of $\mathbf{x}(t)$ will be denoted as $\hat{\mathbf{x}}(t|t-1)$. The KF used in this step was performed by the following recursive equations [13, 14]:

$$\hat{\mathbf{x}}(t|t-1) = \boldsymbol{\phi}\hat{\mathbf{x}}(t-1|t-1) \tag{3.11}$$

$$\mathbf{P}(t|t-1) = \boldsymbol{\phi}\mathbf{P}(t-1|t-1)\boldsymbol{\phi}^{\mathrm{T}} + \mathbf{g}q_{\mathrm{s}}\mathbf{g}^{\mathrm{T}} \tag{3.12}$$

$$\mathbf{k}(t) = \mathbf{P}(t|t-1)\mathbf{h}^{\mathrm{T}}\left(\mathbf{h}\mathbf{P}(t|t-1)\mathbf{h}^{\mathrm{T}} + q_{\mathrm{o}}\right)^{-1} \tag{3.13}$$

$$\hat{\mathbf{x}}(t|t) = \hat{\mathbf{x}}(t|t-1) + \mathbf{k}(t)\Big(s(t) - \mathbf{h}\hat{\mathbf{x}}(t|t-1)\Big) \tag{3.14}$$

$$\mathbf{P}(t|t) = \Big(\mathbf{I} - \mathbf{k}(t)\mathbf{h}\Big)\mathbf{P}(t|t-1) \tag{3.15}$$

where $\hat{\mathbf{x}}(t|t)$ is an update estimate at time t and $\mathbf{k}(t)$ is the Kalman gain which is a blending factor of the noisy measurement and the prior estimate in accordance with Equation (3.13). $\mathbf{P}(t|t-1)$ and $\mathbf{P}(t|t)$ are the error covariance matrices associated with $\hat{\mathbf{x}}(t|t-1)$ and $\hat{\mathbf{x}}(t|t)$.

After completing the forward KF, the smoothed estimates were obtained by the backward estimation, the fixed-interval smoothing, in time taking $t = T-1, T-2, \cdots, 1$ with $\hat{\mathbf{x}}(T|T)$ and $\mathbf{P}(T|T)$. In the fixed-interval smoothing, the old estimate is updated to yield an improvement estimate which is based on all the measurement data. The recursive equations for the fixed-interval smoothing are given as follows [13, 14]:

$$\hat{\mathbf{x}}(t|T) = \hat{\mathbf{x}}(t|t) + \mathbf{A}(t)\Big(\hat{\mathbf{x}}(t+1|T) - \hat{\mathbf{x}}(t+1|t)\Big) \tag{3.16}$$

$$\mathbf{A}(t) = \mathbf{P}(t|t)\boldsymbol{\phi}^{\mathrm{T}}\mathbf{P}^{-1}(t+1|t) \tag{3.17}$$

$$\mathbf{P}(t|T) = \mathbf{P}(t|t) + \mathbf{A}(t)\Big(\mathbf{P}(t+1|T) - \mathbf{P}(t+1|t)\Big)\mathbf{A}^{\mathrm{T}}(t) \tag{3.18}$$

where $\mathbf{A}(t)$ is the smoothing gain. Finally, the smoothed observation was estimated as $\check{s}(t) = \mathbf{h}\hat{\mathbf{x}}(t|T)$. The term $\hat{s}(t)$ without the ocular artifacts was then estimated by directly connecting $\check{s}(t^{\mathrm{N}})$ and $s(t^{\mathrm{S}})$, and cleaned EEGs $\tilde{\mathbf{V}}(t)$ were obtained using $\hat{s}(t)$ and the time courses of other ICs.

In addition, the variances of the state noise and observation noise were also determined by trial and error as $q_{\mathrm{s}} = 1.0$ and $q_{\mathrm{o}} =$ (variance of $s(t^{\mathrm{S}})$), respectively.

3.3 Application to pseudo-EEG

To validate the performance of the proposed method, we made pseudo-EEGs consisting of the ideal EEGs recorded from a subject and five types of simulated ocular artifacts (an eyeblink and four eye-movements: up, down, left, and right) to compare any removal method. In addition, we employed not only CC but also the root mean square error (RMSE) as quantitative criterions. As will hereinafter be described in detail of pseudo-EEGs and the quantitative assessment methods.

3.3.1 Subject

One healthy male subject (24 years, right-handed) participated in EEG measurement. This study was approved by the Ethical Committee, Graduate School of Engineering, Kyoto University, and informed consent was obtained from the subject after he was given a complete explanation of the study.

3.3.2 EEG measurement

The subject seated in a comfortable armchair in a bright room and EEGs were recorded from 128 electrodes scattered over the entire head (according to the modified international 10–20system [18]) using a 128-channel digital EEG system (BioSemi Inc., the Netherlands). The 128 electrode locations are shown in Figure 3.2. Each channel was referenced to the Common Mode Sense (CMS) electrode and grounded to the Driven Right Leg (DRL) electrode. The EEGs were sampled at 512 Hz. EOGs were simultaneously recorded at C7, C29, and D7 (Figure 3.2).

Experiment 1 The subject was instructed to blink or move his eyes after receiving a visual cue (Figure 3.3). There were five types of cues: 'Blink,' 'Up,' 'Down,' 'Left,' and 'Right.' One of five cues was randomly presented for 200 ms with 3.0 s inter stimulus interval and each cue was repeated 25 times.

Experiment 2 EEGs with eyes open were recorded for about 2 min for a healthy male subject who participated in **Experiment 1**. The EEGs were used as artifacts-free ideal EEGs superimposed on ocular artifacts to make pseudo-measured simulated EEGs.

3.3.3 EEG pre-processing

First, EEGs measured in 3.3.2 were digitally filtered with a zero-phase shift band-pass filter from 0.1 to 55 Hz. Subsequently, the filtered EEGs in **Experiment 1** were segmented into 2.0 s epochs of which centers are at the peak of an ocular artifact.

3.3.4 Creation of pseudo-EEGs with ocular artifacts

To compare performances of the proposed and previous methods with respect to the estimation of ideal EEGs and the removal of ocular artifacts, ocular artifacts measured by a 128-channel EEG system were simulated by two equivalent current dipoles (ECDs) with a single-sphere head model (center: [0 cm, 0 cm, 0 cm], radius: 8.0 cm, and electroconductivity: 0.35 S/m; Figure 3.4) utilizing the equivalent multipole moment method [19]. The two dipole sources located near the right and left eyes had the same activities.

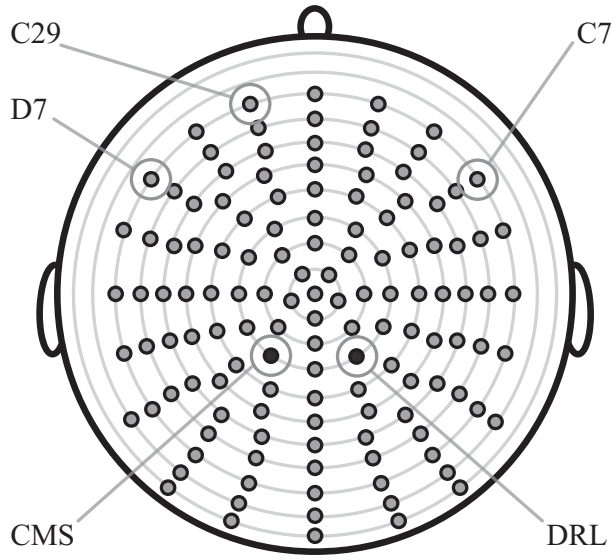

Figure 3.2: 128-ch EEG electrodes, CMS and DRL locations on the scalp (top view)

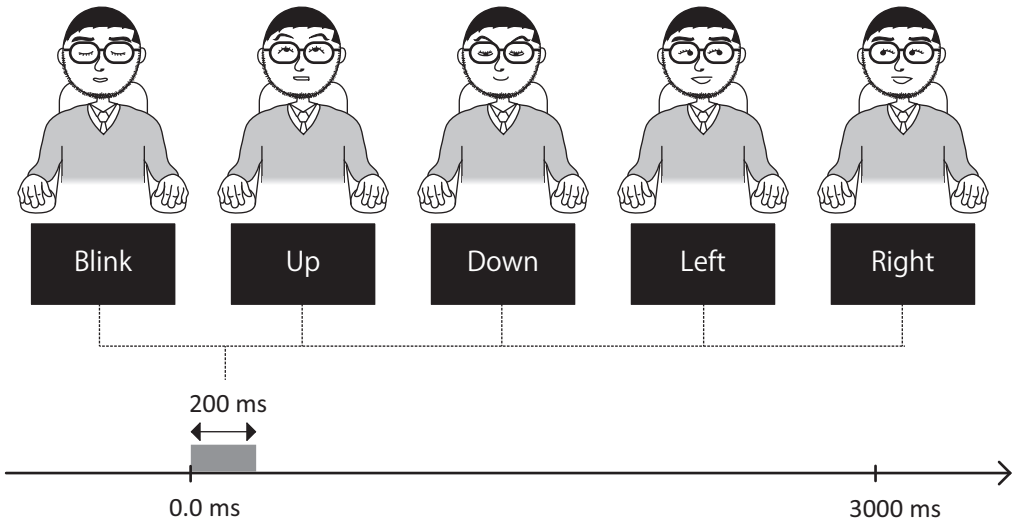

Figure 3.3: Ocular motional paradigm in **Experiment 1**.

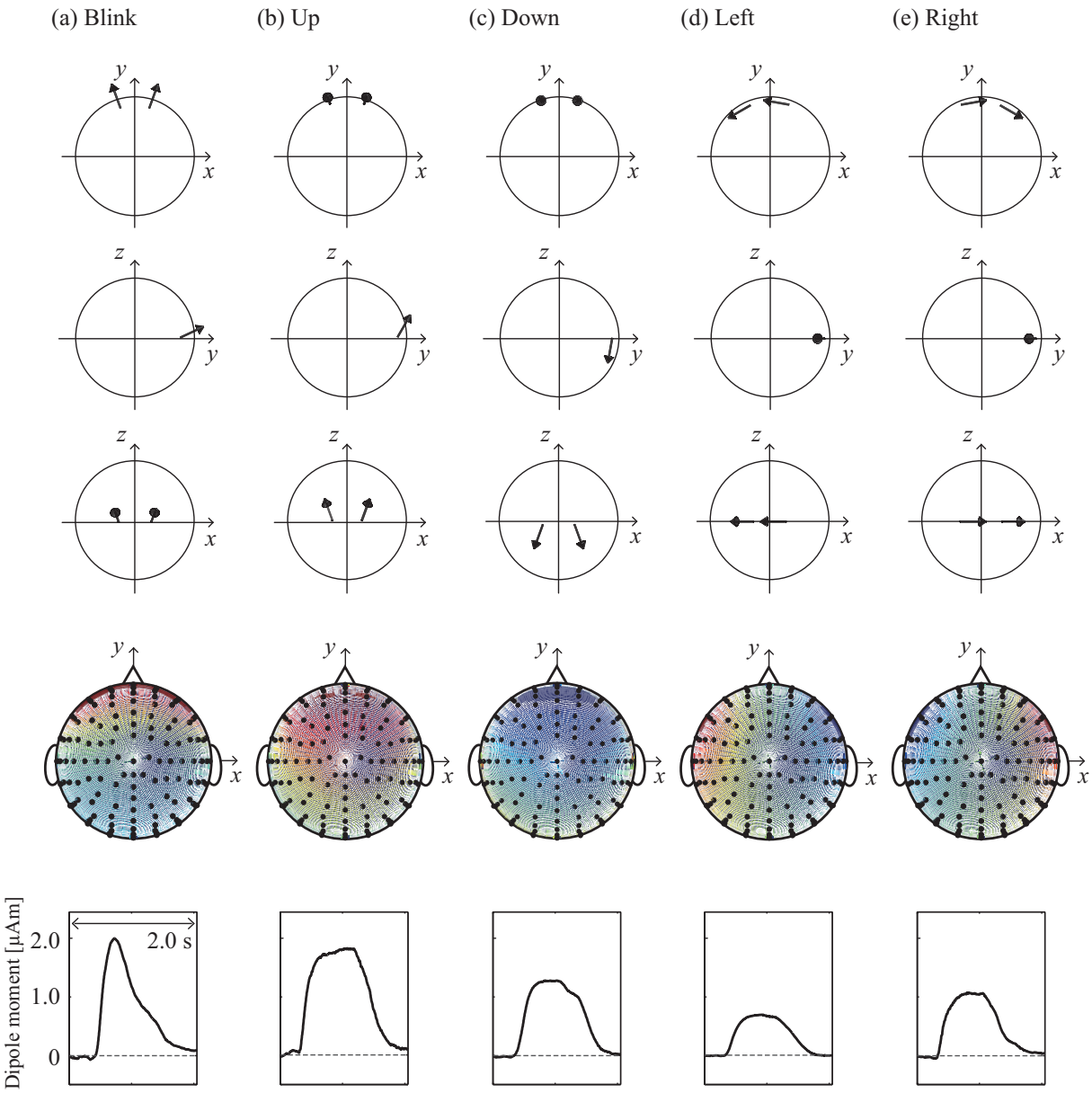

Figure 3.4: Locations of two dipoles, a single-sphere head model, and scalp distribution obtained by solving forward problems and template waveforms with 2 s duration for five types of ocular artifacts: (a) 'Blink,' (b) 'Up,' (c) 'Down,' (d) 'Left,' and (e) 'Right'.

We prepared five dipole sets for five types of ocular activities ('Blink,' 'Up,' 'Down,' 'Left,' and 'Right'), as shown in Figure 3.4. Each orientation of the five dipole sets was determined with reference to a previous study [20]: 'Blink:' [±1.5, 4.0, 1.0]; 'Up:' [±1.0, 1.0, 4.0]; 'Down:' [±1.0, −2.0, −4.0]; 'Left:' [−4.0, −2.0, 0] and [−4.0, 1.0, 0]; 'Right:' [4.0, 1.0, 0] and [4.0, −2.0, 0]. Each dipole set had a wave pattern along with each artifact template in Figure 3.4 for 2 s duration. In Figure 3.4, the five types of templates were obtained by averaging each 25 peak-aligned ocular artifact at C29 (for 'Blink,' 'Up,' 'Down'), D7 (for 'Left'), and C7 (for 'Right'). Then, we calculated the five sets of 128-channel scalp potentials for a 2.0 s duration: $\mathbf{V}_{\mathrm{EYE}}(t)$ ['Blink:' $\mathbf{V}_{\mathrm{BL}}(t)$; 'Up:' $\mathbf{V}_{\mathrm{UP}}(t)$; 'Down:' $\mathbf{V}_{\mathrm{DO}}(t)$; 'Left:' $\mathbf{V}_{\mathrm{LE}}(t)$; 'Right:' $\mathbf{V}_{\mathrm{RI}}(t)$] was obtained from the five dipole sets by solving forward problems. Distribution of the calculated scalp potentials are shown in Figure 3.4.

In addition, $\mathbf{V}^{m}_{\mathrm{EEG}}(t)$, in 100 trials ($m = 1, ..., M$, $M = 100$) for duration of 8.0 s, was randomly extracted from measured ideal (artifact-free) EEGs and $\mathbf{V}_{\mathrm{EYE}}(t)$ was superimposed onto $\mathbf{V}^{m}_{\mathrm{EEG}}(t)$ over a random period of time. Here, C29 was a criterial electrode location of $\mathbf{V}_{\mathrm{BL}}(t)$, $\mathbf{V}_{\mathrm{UP}}(t)$, and $\mathbf{V}_{\mathrm{DO}}(t)$; D7 was that of $\mathbf{V}_{\mathrm{LE}}(t)$; and C7 was that of $\mathbf{V}_{\mathrm{RI}}(t)$. The peak amplitude of $\mathbf{V}_{\mathrm{EYE}}(t)$ was normally distributed across trials with mean and standard deviation calculated from 25 peaks of measured ocular artifacts at a criterion electrode for each type of ocular artifact: $\mathbf{V}_{\mathrm{BL}}(t)$: 471.0 ± 81.6 μV; $\mathbf{V}_{\mathrm{UP}}(t)$: 439.2 ± 135.3 μV; $\mathbf{V}_{\mathrm{DO}}(t)$: 312.6 ± 47.4 μV; $\mathbf{V}_{\mathrm{LE}}(t)$: 143.4 ± 32.9 μV; $\mathbf{V}_{\mathrm{RI}}(t)$: 214.4 ± 27.8 μV. Then, we prepared six different datasets (Types 1–6) representing 100 trials, and there were 600 trials in total, which were distinguished by the number and type of ocular artifacts. Each trial had one ocular artifact in Type 1, two similar ocular artifacts in Type 2, two different ocular artifacts in Type 3, three similar ocular artifacts in Type 4, three ocular artifacts of which two were the same and one was different in Type 5, and three different ocular artifacts in Type 6. When multiple values of $\mathbf{V}_{\mathrm{EYE}}(t)$ were superimposed onto $\mathbf{V}^{m}_{\mathrm{EEG}}(t)$, each ocular artifact avoided overlapping with the others. Figure 3.5 (a) shows the example waveforms for all six types of simulated EEGs.

3.3.5 Evaluation of removal methods

To validate the performance of the proposed method, we compared the ability with previously reported two ICA-based removal methods: 1) ICA-only [4] that employed only ICA, in which ICA is applied to EEGs and the ICs containing ocular artifacts are removed; 2) ICA + EMD [6] that applied EMD to the ICs reflecting ocular artifacts. The three removal methods were applied to 600 trials of the pseudo-EEGs, and the cleaned EEGs $\tilde{\mathbf{V}}^{m}_{\mathrm{EEG}}(t)$ were calculated. CC and RMSE between $\tilde{\mathbf{V}}^{m}_{\mathrm{EEG}}(t)$ and $\mathbf{V}^{m}_{\mathrm{EEG}}(t)$, at C29, C7, and D7 were calculated at three intervals: (i) 'Entire interval,' $t_{\mathrm{i}} = t$, which corresponded to the entire interval (8 s) of the EEGs; (ii) 'Artifact interval,' $t_{\mathrm{ii}} \subseteq t$, which corresponded to the interval (2.0–6.0 s) in which $\mathbf{V}_{\mathrm{EYE}}(t)$ was superimposed; (iii) 'No artifact interval,' $t_{\mathrm{iii}} \subseteq t$, which corresponded to the interval (2.0–6.0 s) in which $\mathbf{V}_{\mathrm{EYE}}(t)$ was not superimposed. In each interval, CC and RMSE at each channel were

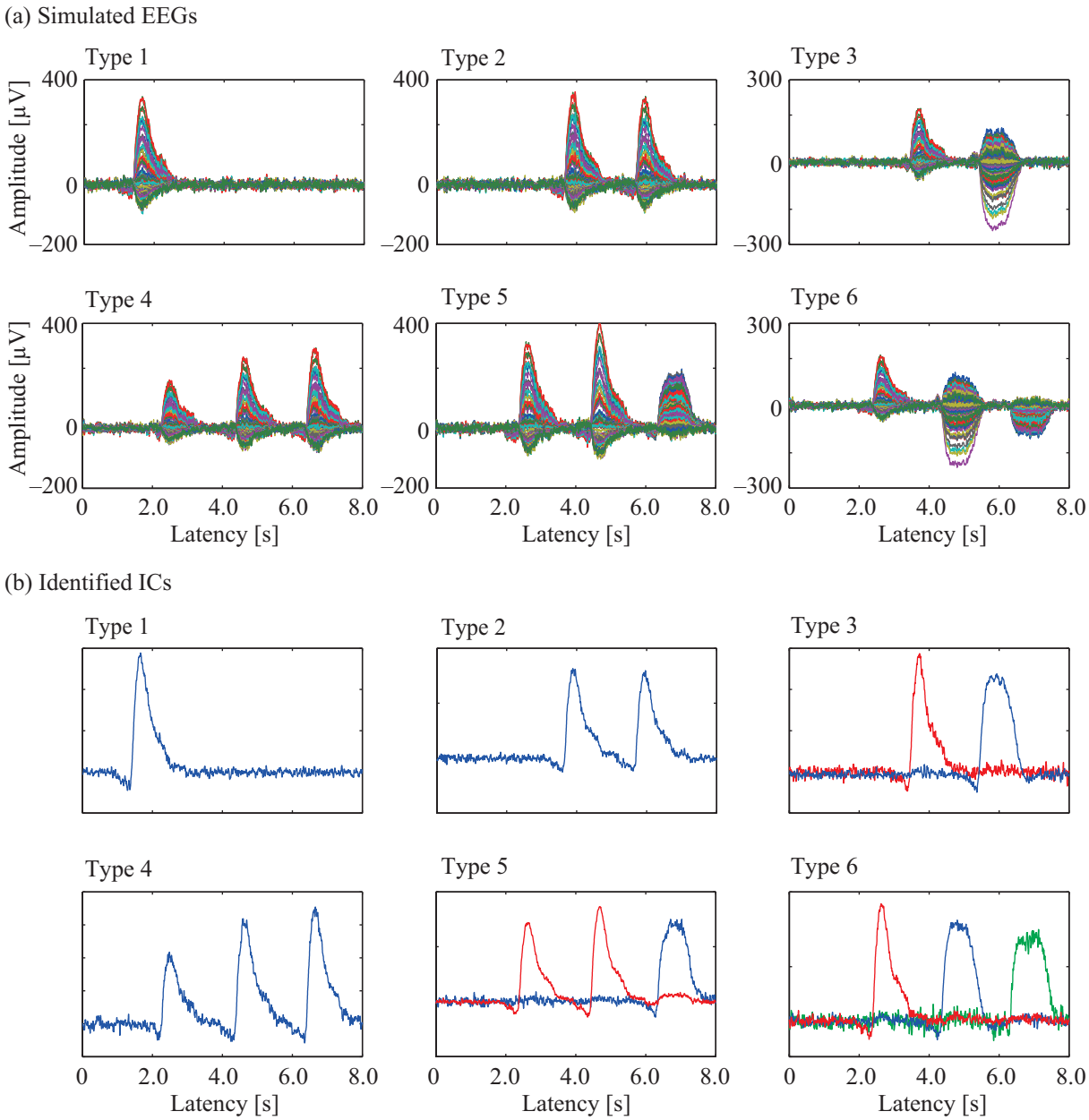

Figure 3.5: Example waveforms of single trials in all six types of (a) the simulated EEGs at 128 electrodes and (b) identified ICs reflecting ocular artifacts. Each trial had one ocular artifact in Type 1, two similar ocular artifacts in Type 2, two different ocular artifacts in Type 3, three similar ocular artifacts in Type 4, three ocular artifacts of which two were the same and one was different in Type 5, and three different ocular artifacts in Type 6

given as

RMSE:

$$\psi^m_{t_l/Ch} = \sqrt{\frac{1}{L}\sum_{t\in t_l}\left(\tilde{v}^m_{Ch}(t) - v^m_{Ch}(t)\right)^2} \tag{3.19}$$

CC:

$$r^m_{t_l/Ch} = \frac{\sum_{t\in t_l}\left(\tilde{v}^m_{Ch}(t) - \overline{\tilde{v}^m_{Ch}(t)}\right)\left(v^m_{Ch}(t) - \overline{v^m_{Ch}(t)}\right)}{\sqrt{\sum_{t\in t_l}\left(\tilde{v}^m_{Ch}(t) - \overline{\tilde{v}^m_{Ch}(t)}\right)^2}\sqrt{\sum_{t\in t_l}\left(v^m_{Ch}(t) - \overline{v^m_{Ch}(t)}\right)^2}} \tag{3.20}$$

where l (l refers to i, ii or iii) is a interval index, L is the number of samples among t_l, $\tilde{v}^m_{Ch}(t)$ and $v^m_{Ch}(t)$ denote the scalp potential at the channel Ch (C29, C7 or D7) of $\tilde{\mathbf{V}}^m_{\mathrm{EEG}}(t)$ and $\mathbf{V}^m_{\mathrm{EEG}}(t)$ each other, the overbar represents the trial averaging. As a result, 300 pairs of CC and RMSE (100 trials × 3 electrodes) were calculated for each simulated dataset at each interval. Distributions of RMSE and CC obtained by the proposed method were compared to those obtained by ICA-only and ICA + EMD using the Wilcoxon signed-rank test because not all RMSE and CC were Gaussian distributions. A higher CC and lower RMSE indicate a better estimation of ideal EEGs.

In this study, u, which is a multiplication factor that determines the upper limit of acceptable standard deviations in the classification of IMFs with the EMD in Equation (3.4) in **Step 2**, had a rule-of-thumb value of 1.25 for the proposed method. Note that ICA + EMD also needed a similar multiplication factor p (See [6]), and the value of p that was employed was 2.00, which was one of the recommended thresholds in the previous study [6]. ICA-only did not use u or p.

3.4 Results

In Figure 3.6, density distributions of RMSE–CC pairs were visualized by RMSE–CC plots for six datasets, three different intervals, and three different removal methods. In Figure 3.6, density distributions of RMSE–CC pairs obtained by ICA-only appeared to spread more widely, and was worse than that obtained by the proposed method and ICA + EMD at all three intervals. Whereas density distributions of RMSE–CC pairs obtained by the proposed method appeared to be similar to those obtained by ICA + EMD at the ‘Entire interval’ and ‘Artifact interval’, those obtained by the proposed method appeared to be narrower and better than those obtained by ICA + EMD at the ‘No artifact interval.’

The results of the Wilcoxon signed-rank test (p-values) of RMSE and CC for six datasets, and three different intervals are shown in Table 3.1. The asterisks indicate significant differences

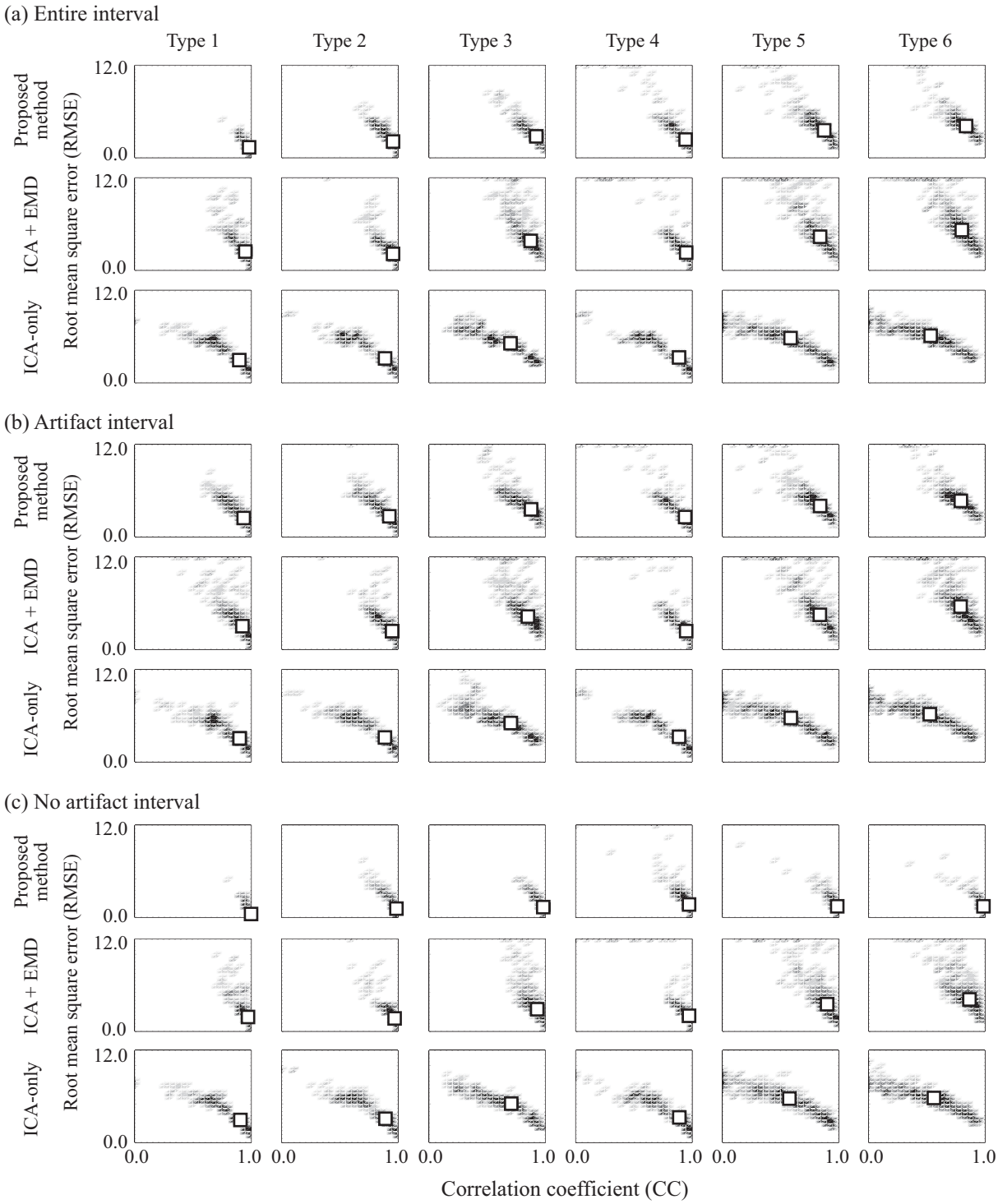

Figure 3.6: Density distributions of RMSE–CC pairs for six types of dataset (Type 1 – 6) and three different removal methods calculated at three different intervals: (a) 'Entire interval,' (b) 'Artifact interval,' and (c) 'No artifact interval'. Density is represented by darkness and an open square indicates median value in each plot.

Table 3.1: *p*-values of Wilcoxon test comparing CC and RMSE of the proposed method with ICA + EMD and ICA-only

	Entire Interval		Artifact interval		No-artifact interval	
	ICA + EMD	ICA-only	ICA + EMD	ICA-only	ICA + EMD	ICA-only
CC						
Type 1	*	*	0.051	*	*	*
Type 2	0.931	*	0.013	*	0.931	*
Type 3	*	*	0.091	*	*	*
Type 4	0.751	*	0.409	*	0.751	*
Type 5	0.029	*	0.802	*	0.029	*
Type 6	*	*	0.675	*	*	*
RMSE						
Type 1	*	*	*	*	*	*
Type 2	0.962	*	0.110	*	*	*
Type 3	*	*	*	*	*	*
Type 4	0.750	*	0.466	*	0.001	*
Type 5	*	*	0.006	*	*	*
Type 6	*	*	*	*	*	*

* the significance with $p < 0.001$.

with $p < 0.001$. Statistical analysis showed that performance of the proposed method was significantly better than those of both ICA-only for RMSE and CC at all three intervals and ICA + EMD at 'No artifact interval' in all types of dataset. On the other hand, at the 'Artifact interval,' the performance of the proposed method was not significantly better than that of ICA + EMD for RMSE and CC in Types 2, 4, and 5. For the 'Entire interval,' the proposed method did not perform significantly better than ICA + EMD for CC in Types 2, 4, and 5, and for RMSE in Types 2 and 4.

Figure 3.5 (b) shows the example waveforms of identified ICs reflecting ocular artifacts, which were obtained from EEGs shown in Figure 3.5 (a), and mean number of those identified ICs for each dataset was 1.1 for Type 1, 2 and 4; 1.8 for Type 3; 2.7 for Type 5; and 3.2 for Type 6. As the number of or types of ocular artifacts increased, more ICs were identified as reflecting ocular artifacts. The mean numbers of those ICs identified in Types 2 and 4 were fewer than those in Types 3, 5, and 6. Nevertheless, the number of ocular artifacts in Types 2 and 4 were the same as or larger than those in Types 3, 5, and 6.

Figure 3.7 shows a typical example waveforms of identified ICs reflecting ocular artifacts, which were obtained from Types 1 and 6, as shown in Figure 3.5 (b), and which were cleaned by the proposed method and ICA + EMD. While the proposed method removed ocular artifacts as well as ICA + EMD, the proposed method retained EEGs at the 'No artifact interval' for both Types 1 and 6. In addition, Figure 3.8 shows a typical example of cleaned waveforms of Types 1 and 6 that were obtained from EEGs (shown in Figure 3.5 (a)) using three different removal

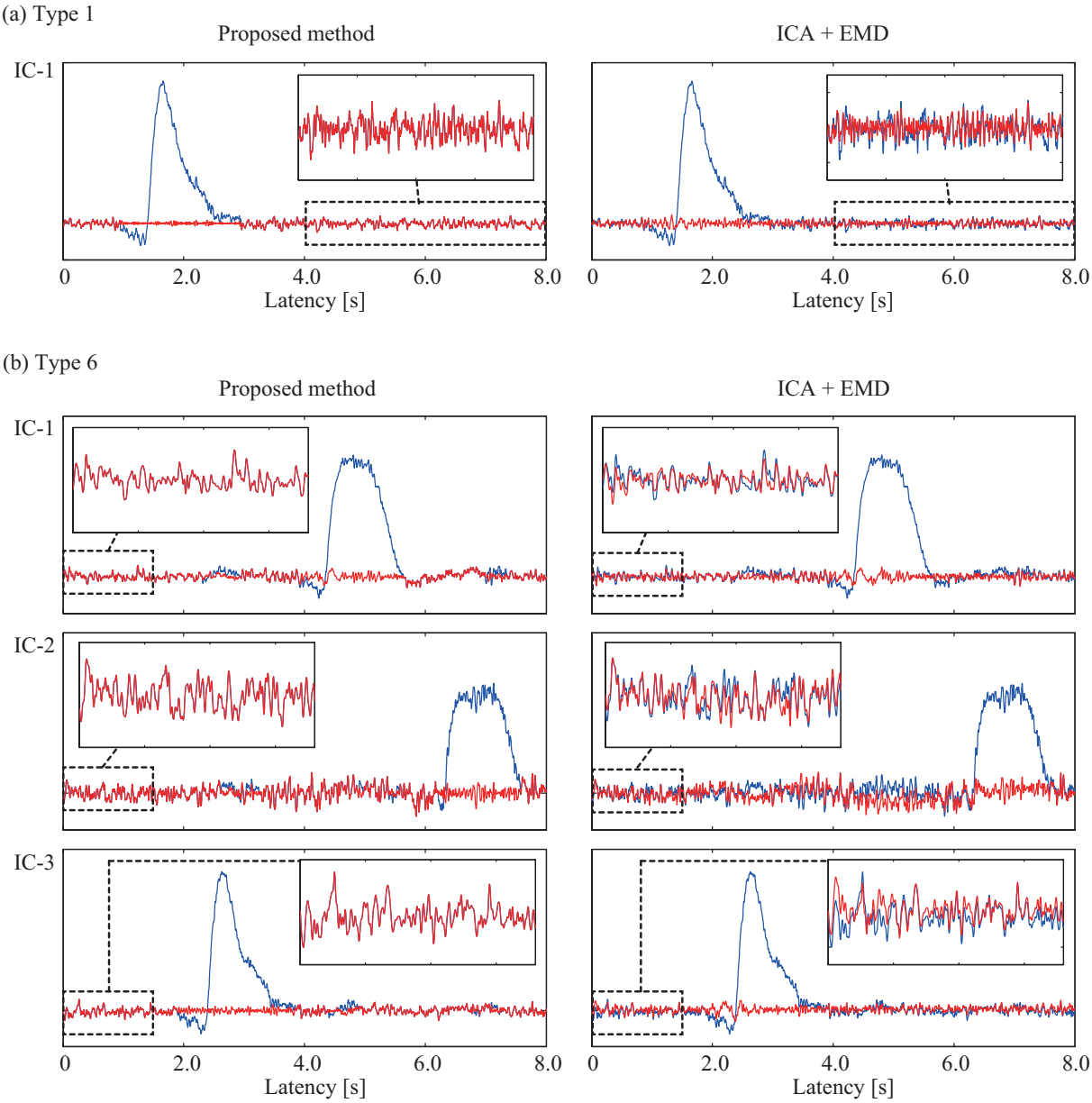

Figure 3.7: Example waveforms of identified ICs that reflect ocular artifacts and are cleaned by the proposed method and ICA + EMD for (a) Type 1 and (b) Type 6. Blue and red lines indicate identified and cleaned ICs, respectively.

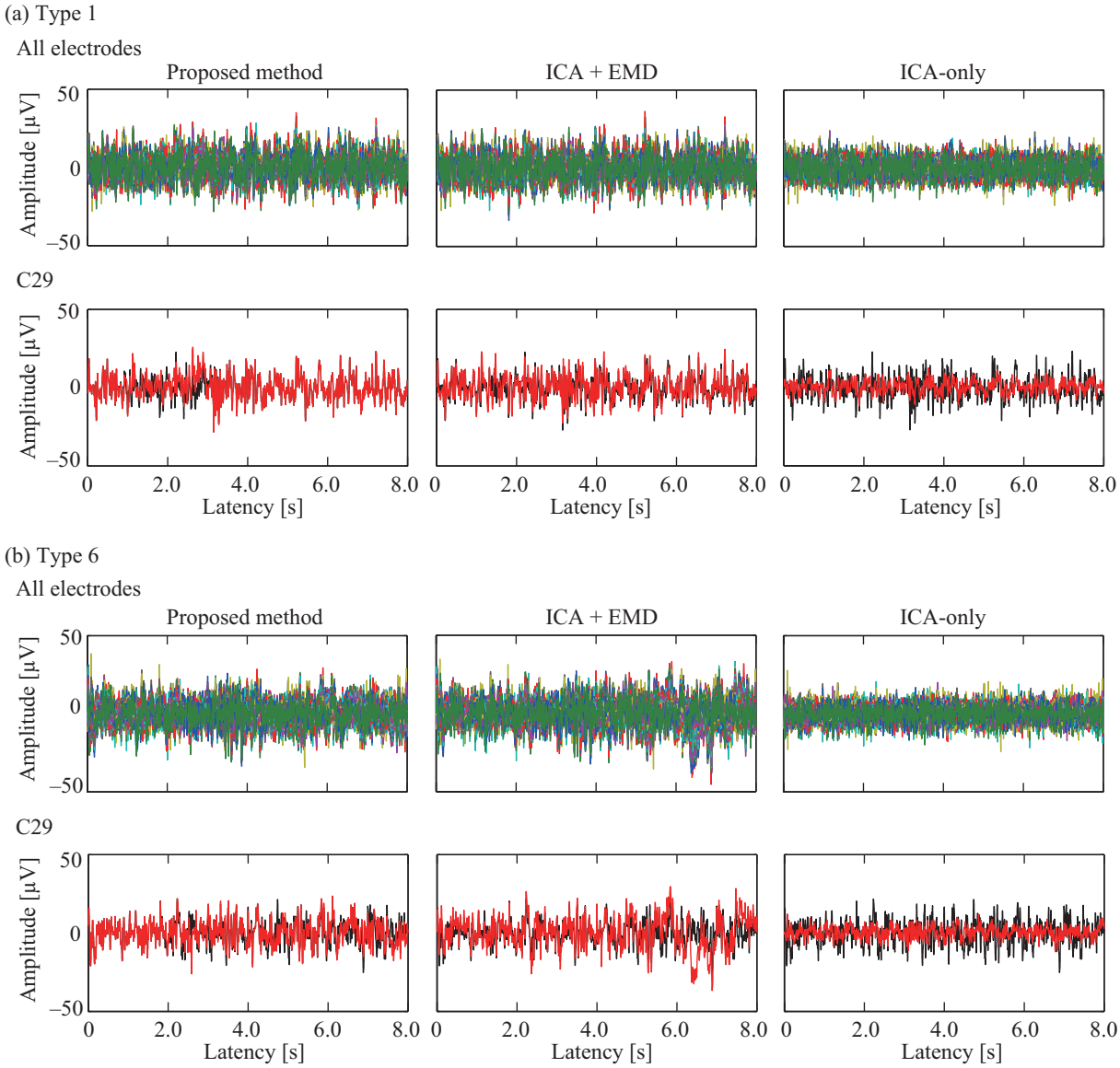

Figure 3.8: Cleaned EEG waveforms at all 128 electrodes, and simulated ideal EEG waveforms at C29, and estimated ideal EEG waveforms using three different methods for (a) Type 1 and (b) Type 6. At C29, black and red lines indicate ideal and cleaned EEG waveforms, respectively.

methods at all 128 electrodes and C29, respectively. ICA-only obviously removed ideal EEGs, and ICA + EMD removed some part of the ideal EEGs at the 'No artifact interval.' On the other hand, the proposed method appeared to remove ocular artifacts, but retained ideal EEGs at the 'No artifact interval.'

3.5 Discussion

In this study, a novel method based on the combination of ICA, EMD, and the KF was proposed to remove ocular artifacts automatically. Whereas ICA provided a spatial filter that conveniently captured wide-spread ocular activity in a small set of ICs, locally restricted EMD provided a frequency filter [21] to selectively and locally exclude artifacts from these ICs, and the KF estimated ideal EEGs.

In Figure 3.6, a higher CC and lower RMSE indicated that cleaned waveforms were correlated and identical with ideal waveforms, respectively. Density distributions of RMSE–CC pairs indicated that the proposed method consistently retained ideal EEGs at the 'No artifact interval' for all datasets, unlike other methods. At the 'Entire interval' and 'Artifact interval,' density distributions of RMSE–CC pairs of Types 1, 2, and 4 appeared to be clearly better than those of Types 3, 5, and 6 for different three methods. In addition, Table 3.1 showed that distributions of RMSE and CC of Types 2 and 4 were not significantly different for the proposed method and ICA + EMD. The reason for these was that multiple ICs were identified to be reflecting ocular artifacts for Types 3, 5, and 6, whereas almost one IC was identified for Types 1, 2, and 4. That is, ICA-only and ICA + EMD over-removed more ideal EEGs than the proposed method as the number of identified ICs increased.

The example waveforms of ICs cleaned by the proposed method and ICA + EMD in Figure 3.7 showed that with more ICs identified as reflecting ocular artifacts, more ideal EEGs were removed by ICA + EMD. The amplitude of the EEG waveforms cleaned by ICA-only for Type 6 (as shown in Figure 3.8 (b)) was visually observed as being much smaller than those cleaned by the proposed method and ICA + EMD. Practically, the mean amplitudes of all electrodes obtained by the ICA only for Type 6 (3.45 ± 0.38 μV among trials) were smaller than those obtained for ideal EEGs (3.98 ± 0.19μV among trials). This may be because one IC was identified as reflecting ocular artifacts for Type 1, whereas three ICs were identified for Type 6 (Figure 3.5 (b)).

These results indicated that the performance of ICA-based removal methods depend on the number of identified ICs reflecting ocular artifacts and the type of ocular artifacts, and have not been referred in previous assessments of removal methods that are based on ICA.

The proposed method described here is conceptually similar to ICA + EMD, which was recently proposed by Lindsen and Bhattacharya [6], who applied EMD to the ICs reflecting ocular artifacts at entire intervals in order to separate the blink artifacts from the EEGs and

attempted to retain ideal EEGs. However, ICA + EMD did not significantly prevent the removal of ideal EEGs because ICA + EMD applied EMD to entire interval containing no artifact. On the other hand, the proposed method estimated beforehand the duration of identified ICs for which ocular artifacts occurred, and applied EMD to only the estimated duration for each identified IC. Then, the proposed method removed a minimum number of ocular artifacts and retained ideal EEGs.

In addition, we employed Infomax algorithm for ICA in accordance with previous study [4]. Klemm et al. [22] compared a lot of ICA algorithms for source separation of EEG and indicated that Infomax algorithm delivered very good results but might be too slow for many applications. Then, if we have to deal with amount of EEG trials including ocular artifacts, we should employ another ICA algorithm in place of Infomax algorithm.

In this study, we carried out a quantitative assessment of information loss using pseudo-EEGs with simulated ocular artifacts. The simulated ocular artifacts were obtained by a single-sphere head model and two ECDs that represented right and left eyes, while a simulated ocular artifact made by Lindsen and Bhattacharya [6] assumed that one eye-blink artifact was contributed by only one IC and superimposed on the IC. The simulated ocular artifacts can assume not only multiple eye-blink but also some eye-movement artifacts, and assess both ICA-based and regression-based removal methods. However, in this case, the orientations of two equivalent dipoles were stationary, whereas the real orientations were not [23]. Then, the more realistic simulation of eye-blinks and eye-movements would accurately assess the removal methods.

Finally, the proposed method was applied to the measured EEGs containing ocular artifacts. Figure 3.9 shows the waveforms of the EEGs before and after the removal of ocular artifacts. As seen in the figure, ocular artifacts could be successfully removed for measured data, although we could not confirm information loss of measured EEG data.

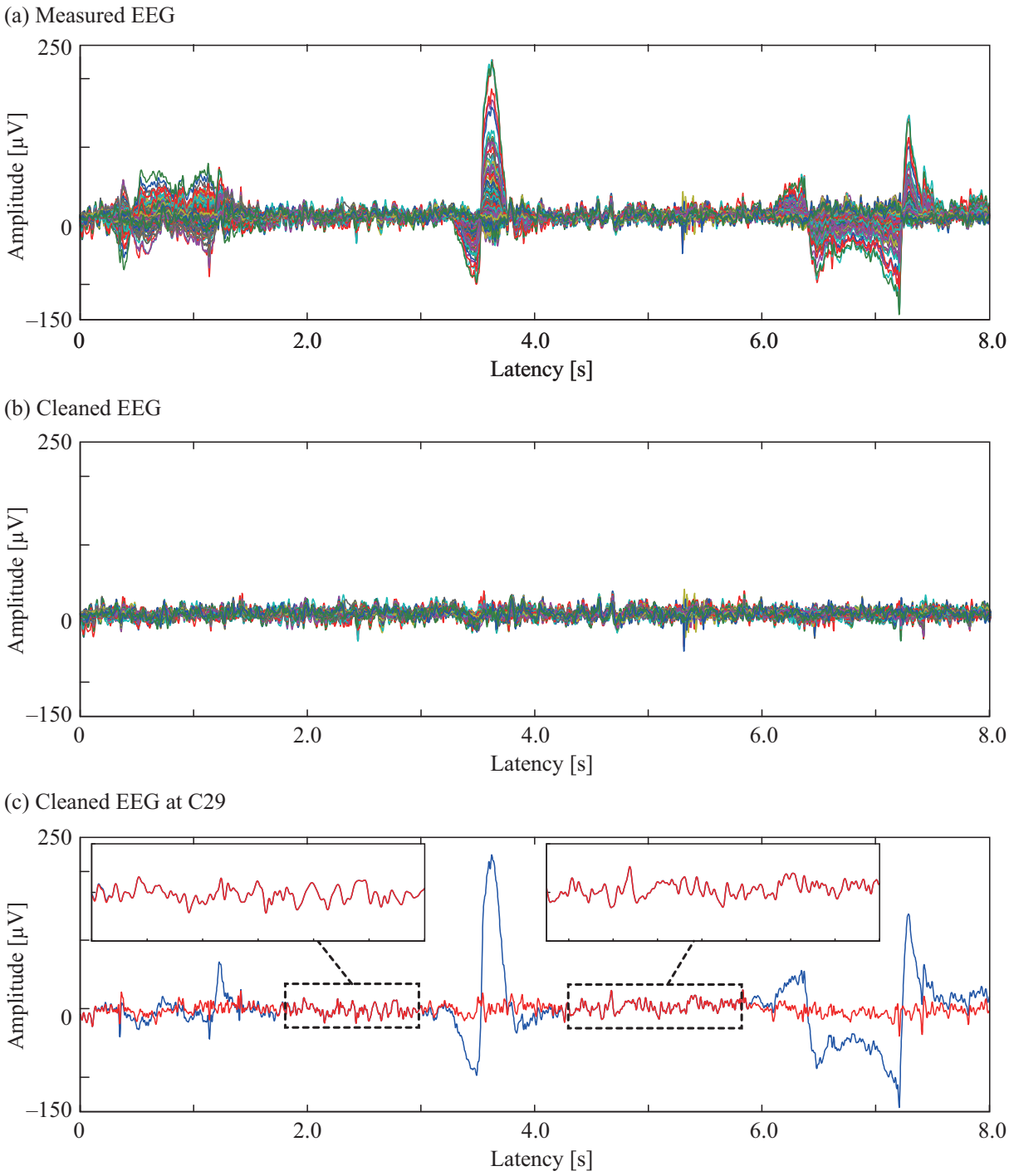

Figure 3.9: (a) Measured EEG waveforms containing three ocular artifacts for all 128 channels and (b) cleaned EEG waveforms obtained using the proposed method. (c) Blue and red lines indicate original and cleaned EEG waveforms at C29, respectively.

References

[1] Jung, T. P., Makeig, S., Humphries, C., Lee, T. W., Mckeown, M. J., Iragui, V., & Sejnowski, T. J. (2000). Removing electroencephalographic artifacts by blind source separation. Psychophysiology, 37(2), 163–178.

[2] Jung, T. P., Makeig, S., Westerfield, M., Townsend, J., Courchesne, E., & Sejnowski, T. J. (2000). Removal of eye activity artifacts from visual event-related potentials in normal and clinical subjects. Clinical Neurophysiology, 111(10), 1745–1758.

[3] Castellanos, N. P., & Makarov, V. A. (2006). Recovering EEG brain signals: artifact suppression with wavelet enhanced independent component analysis. Journal of neuroscience methods, 158(2), 300–312.

[4] Okada, Y., Jung, J., & Kobayashi, T. (2007). An automatic identification and removal method for eye-blink artifacts in event-related magnetoencephalographic measurements. Physiological Measurement, 28(12), 1523–1532.

[5] Gao, J. F., Yang, Y., Lin, P., Wang, P., & Zheng, C. X. (2010). Automatic removal of eye-movement and blink artifacts from EEG signals. Brain topography, 23(1), 105–114.

[6] Lindsen, J. P., & Bhattacharya, J. (2010). Correction of blink artifacts using independent component analysis and empirical mode decomposition. Psychophysiology, 47(5), 955–960.

[7] Joyce, C. A., Gorodnitsky, I. F., & Kutas, M. (2004). Automatic removal of eye movement and blink artifacts from EEG data using blind component separation. Psychophysiology, 41(2), 313–325.

[8] Jung, T. P., Humphries, C., Lee, T. W., Makeig, S., McKeown, M. J., Iragui, V., & Sejnowski, T. J. (1998). Extended ICA removes artifacts from electroencephalographic recordings. Advances in neural information processing systems, 894–900.

[9] Wallstrom, G. L., Kass, R. E., Miller, A., Cohn, J. F., & Fox, N. A. (2004). Automatic correction of ocular artifacts in the EEG: a comparison of regression-based and component-based methods. International journal of psychophysiology, 53(2), 105–119.

[10] Croft, R. J., Chandler, J. S., Barry, R. J., Cooper, N. R., & Clarke, A. R. (2005). EOG correction: A comparison of four methods. Psychophysiology, 42(1), 16–24.

[11] Pham, T. T., Croft, R. J., Cadusch, P. J., & Barry, R. J. (2011). A test of four EOG correction methods using an improved validation technique. International Journal of Psychophysiology, 79(2), 203–210.

[12] Huang, N. E., Shen, Z., Long, S. R., Wu, M. C., Shih, H. H., Zheng, Q., ... & Liu, H. H. (1998). The empirical mode decomposition and the Hilbert spectrum for nonlinear and non-stationary time series analysis. Proceedings of the Royal Society of London. Series A: Mathematical, Physical and Engineering Sciences, 454(1971), 903–995.

[13] Brown, S. A., & Hwang P. Y. C. (2012). Introduction to random signals and applied Kalman filtering: with MATLAB exercises. 4th ed. John Wiley & Sons, Inc.

[14] Chui, C. K., & Chen, G. (1999). Kalman filtering: with real-time applications. Springer.

[15] Tarvainen, M. P., Hiltunen, J. K., Ranta-aho, P. O., & Karjalainen, P. A. (2004). Estimation of nonstationary EEG with Kalman smoother approach: an application to event-related synchronization (ERS). Biomedical Engineering, IEEE Transactions on, 51(3), 516–524.

[16] Akaike, H. (1969). Fitting autoregressive models for prediction. Annals of the institute of Statistical Mathematics, 21(1), 243–247.

[17] Oikonomou, V. P., Tzallas, A. T., & Fotiadis, D. I. (2007). A Kalman filter based methodology for EEG spike enhancement. Computer methods and programs in biomedicine, 85(2), 101–108.

[18] BioSemi. Headcaps. Retrieved January 1st, 2014, from http://www.biosemi.com/headcap.htm

[19] Washizu, M., & Jones, T. B. (1996). Dielectrophoretic interaction of two spherical particles calculated by equivalent multipole-moment method. Industry Applications, IEEE Transactions on, 32(2), 233–242.

[20] Berg, P., & Scherg, M. (1991). Dipole models of eye movements and blinks. Electroencephalography and clinical Neurophysiology, 79(1), 36–44.

[21] Flandrin, P., Rilling, G., & Goncalves, P. (2004). Empirical mode decomposition as a filter bank. Signal Processing Letters, IEEE, 11(2), 112–114.

[22] Klemm, M., Haueisen, J., & Ivanova, G. (2009). Independent component analysis: comparison of algorithms for the investigation of surface electrical brain activity. Medical & biological engineering & computing, 47(4), 413–423.

[23] Iwasaki, M., Kellinghaus, C., Alexopoulos, A. V., Burgess, R. C., Kumar, A. N., Han, Y. H., ... & Leigh, R. J. (2005). Effects of eyelid closure, blinks, and eye movements on the electroencephalogram. Clinical Neurophysiology, 116(4), 878–885.

Chapter 4

A background EEG removal method for ERP

ERP is a neural response to an internal or external event, and can be obtained by averaging time-locked scalp potentials. The ERP measured in a single trial often has a low SNR because of the relatively large background due to the rhythmic EEG noise. This chapter proposes a novel method to enhance ERPs by combining PCA with MEMD. In the proposed method, PCA reduces the data dimensions, while MEMD removes the relatively large background EEGs. The performance of the method is evaluated with simulated and measured the P300 obtained from a visual oddball experiment. The results demonstrate that the proposed method can substantially reduce the background EEGs and improve the SNR of the P300.

4.1 Background

ERPs are transient scalp electric potentials elicited by neuronal activities, and often have a series of positive and negative wavelike components that are temporally induced by events such as visual stimulus presentations. A number of repetitions (trials) are required to detect ERPs because their amplitudes are smaller than those of the background EEGs. Because of the low SNR, ERPs cannot be readily seen in a raw EEG tracing. Therefore, a number of single trials that are time-locked to a specific event, such as a stimulus presentation, are required to be averaged to enhance the ERP.

Although the SNR of the ERP increases with increase in the number of trials, a long recording time is required and fatigue is likely to be experienced by the subjects [1]. In particular, in the recordings with complex tasks that are related to higher brain functions, such as a memory task that elicits ERPs at relatively long latencies (>300 ms) such as P300 and N600 [2, 3], it is difficult to increase the number of trials without the subjects experiencing fatigue.

Therefore, a variety of methods have been reported to improve the SNR of ERPs with a smaller number of trials. These are divided into two groups, i.e. unichannel and multichannel methods. The unichannel method is based on model-based approaches using the AR models

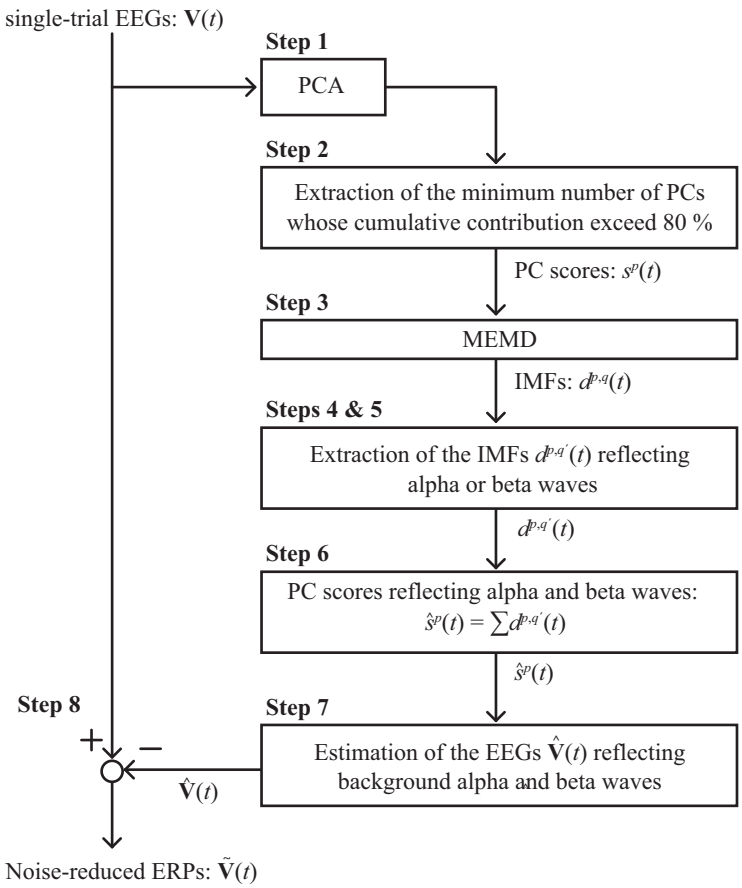

Figure 4.1: Flow chart of the proposed method.

and the autoregressive moving average models [4], the WT [5, 6], the KF [7], and EMD [1].

On the other hand, multichannel method is based on PCA [8], ICA [9, 10], and more BSS algorithms. However, these multichannel methods presuppose the existence of a sufficient number of trials because they need some information obtained from all trials for noise removal. In other words, these methods may fail to remove background EEGs if there is a small number of trials.

4.2 A background EEG removal method

The proposed method for enhancing multichannel-recorded ERPs consisted of the following eight steps (Figure 4.1). In the proposed method, the Halton sequence in 2.4.3 was used to generate a set of $I = 512$ direction vectors for taking signal projections. In addition, for MEMD shifting process, we employed the EMD sifting criterion, given in a previous study[11], that the sifting is stopped when the number of zero crossings and extrema is the same number for 2 successive sifting steps, and the maximum number of siftings is 100 to prevent the sifting

procedures from locking in a never-ending loop.

Step 1 The dimension of multivariate EEG data was reduced by PCA, because the performance of the signal projections along different directions in n-dimensional spaces may decrease with an increase in the number of dimensions in the MEMD process [12]. The minimum number of PCs, whose cumulative contribution exceeded 80%, which is known to adequately explain the original multivariate EEGs, was extracted. When $\mathbf{V}(t)$ is the multivariate EEG and $\mathbf{w}^p$ is the pth PC eigenvector, the pth PC score $s^p(t)$ is given by the following equation:

$$s^p(t) = \mathbf{V}(t)\mathbf{w}^p \tag{4.1}$$

Step 2 The minimum number P of PCs, of which the cumulative contribution of the PC number exceeded 80%, is determined.

Step 3 MEMD is applied to the matrix of P PC scores denoted by $\mathbf{s}(t) = [s^1(t), ..., s^p(t),..., s^P(t)]$ to obtain Q sets of IMFs denoted by $\mathbf{D}(t) = [\mathbf{d}^1(t), ..., \mathbf{d}^q(t), ..., \mathbf{d}^Q(t)]$, where $\mathbf{d}^q(t) = [d^{1,q}(t), ..., d^{p,q}(t), ..., d^{P,q}(t)]$.

Step 4 Amplitude spectra, $\mathbf{D}(f) = [\mathbf{d}^1(f), ..., \mathbf{d}^q(f), ..., \mathbf{d}^Q(f)]$, are derived by the fast Fourier transform of $\mathbf{D}(t)$, where $\mathbf{d}^q(f) = [d^{1,q}(f), ..., d^{p,q}(f), ..., d^{P,q}(f)]$.

Step 5 In the case where $d^{p,q'}(f)$ $(q' = 1, ..., Q')$ has a peak at a frequency range of 8–35 Hz, $\mathbf{d}^{q'}(t)$ is treated as an IMF reflecting background alpha or beta waves, and its number is determined as Q'.

Step 6 PC scores reflecting the alpha and beta waves, denoted by $\hat{\mathbf{s}}(t) = [\hat{s}^1(t), ..., \hat{s}^p(t), ..., \hat{s}^P(t)]$ are reconstructed by summing all Q' sets of IMFs with a spectrum peak at 8–35 Hz, as follows:

$$\hat{s}^p(t) = \sum_{q'=1}^{Q'} d^{p,q'}(t) \tag{4.2}$$

Step 7 Then, EEGs reflecting background alpha and beta waves, denoted by $\hat{\mathbf{V}}(t)$, are calculated as

$$\hat{\mathbf{V}}(t) = \sum_{p=1}^{P} \hat{s}^p(t)(\mathbf{w}^p)^{\mathrm{T}} \tag{4.3}$$

Step 8 Finally, noise-reduced ERPs $\tilde{\mathbf{V}}(t)$ are estimated to subtract $\hat{\mathbf{V}}(t)$ from $\mathbf{V}(t)$ as follows:

$$\tilde{\mathbf{V}}(t) = \mathbf{V}(t) - \hat{\mathbf{V}}(t) \tag{4.4}$$

4.3 Application to pseudo-EEG and measured EEG

To validate the performance of the proposed method, we applied the method to pseudo-measured simulated and measured ERP data. The simulated ERP data were made by the superposition of measured background EEGs and simulated P300 ERP. Here, we described the measurement and simulation methods. As quantitative criterions, we employed RMSE, amplitude deviation and latency deviation. Hereinafter, the detail of pseudo-EEGs and the quantitative assessment methods will be described.

4.3.1 Subjects

Two healthy male subjects (ages: 22 and 28 years, right-handed) participated in an ERP experiment. This study was approved by the Ethics Committee, Graduate School of Engineering, Kyoto University, and informed consent was obtained from the subjects after they were given a complete explanation of the study.

4.3.2 EEG measurement

Experiment 1 The subjects sat in a comfortable chair approximately 50 cm from a display in a dark room. EEGs were recorded from 128 locations (extended 10–20 system) using a 128-channel digital EEG system (BioSemi Inc., The Netherlands) and sampled at 1024 Hz. Locations of the 128 electrodes, a referenced to CMS electrode and a grounded to DRL electrode are shown in Figure 4.2. The subjects performed an oddball paradigm task with both target and non-target visual stimuli (Figure 4.3). Each stimulus consisted of one Chinese character, and subtended a visual angle of $3.5^\circ \times 3.5^\circ$. The target stimulus was ‘midori’ for green and the non-target stimuli was ‘aka’ for red on a black background. The duration of the stimulus presentation was 200 ms with 1800–2200 ms inter stimulus interval. There were four blocks, each of which contained a random mix of 80 non-target stimuli and 20 target stimuli. In total, the subjects received 80 target and 320 non-target stimuli in a random order. The subjects were instructed to silently count the number of target stimuli.

Experiment 2 EEGs with eyes-open were recorded about 2 minutes for one healthy male subject (22 years old) who joined **Experiment 1**. The EEGs were used as background noise superimposed on ERPs to make pseudo-measured simulated ERP data.

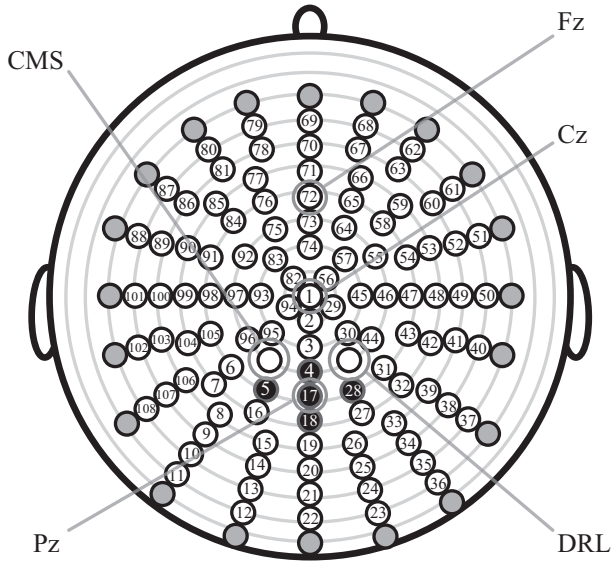

Figure 4.2: 128-channel EEG electrode, CMS, and DRL locations on a scalp (top view)

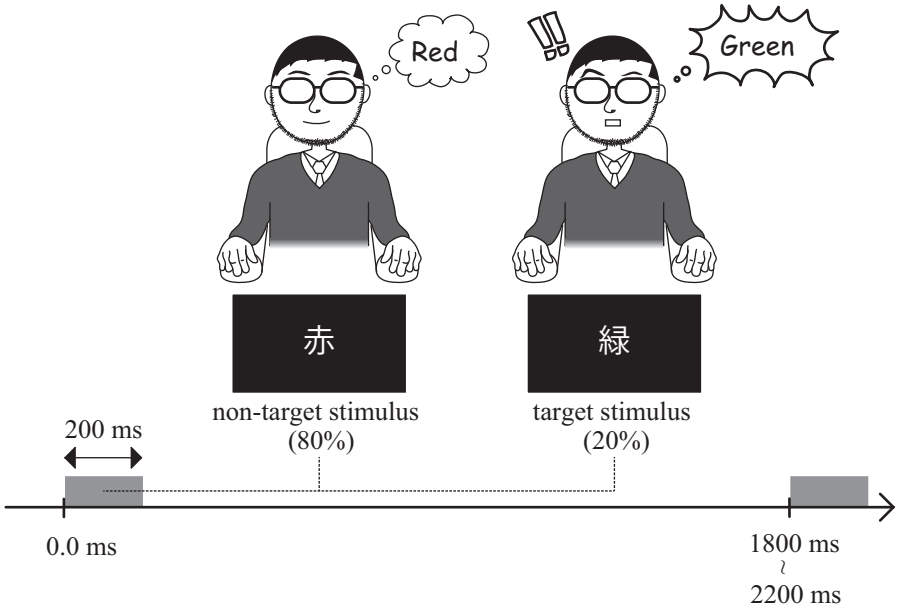

Figure 4.3: Oddball paradigm in **Experiment 1**.

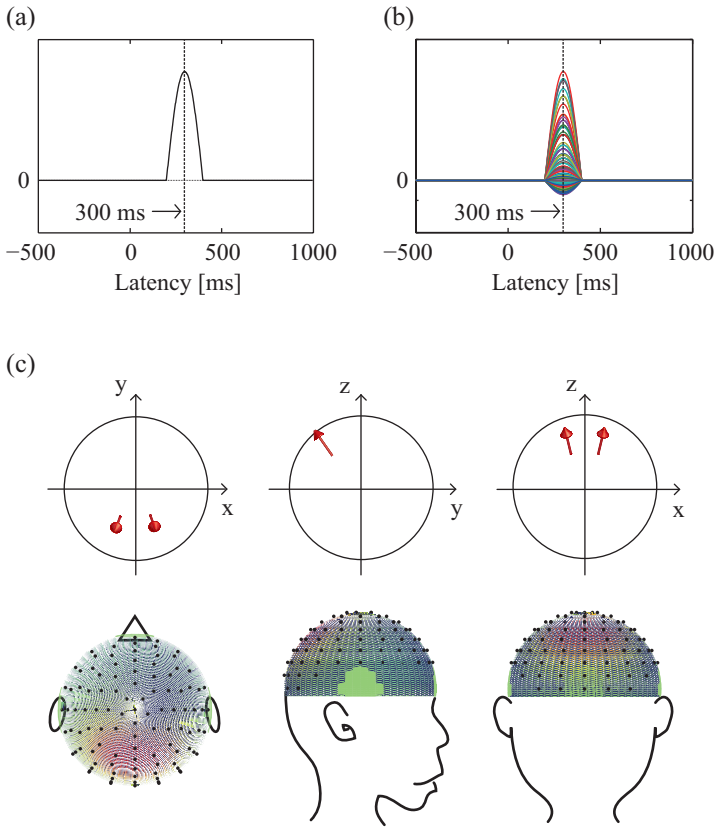

Figure 4.4: (a) An ERP template which was a 2.5-Hz half-wave and had a peak at 300 ms. (b) Superposition of ERP waveforms at 108 electrodes obtained by solving forward problem. (c)Two equivalent current dipoles representing sources of P300 with a single-layer sphere head model (upper row) and scalp topographies obtained by solving a forward problem at 300 ms (lower row).

4.3.3 EEG pre-processing

First, the EEGs measured in **Experiment 1** were re-referenced to the left mastoid and digitally filtered with a zero-phase shift band-pass from 0.5 Hz to 35 Hz. Subsequently, the filtered EEGs were segmented as epochs with a 1500 ms time interval from −500 ms to 1000 ms following the onset of the stimulus. The interval between −500 ms and 0 ms was regarded as a pre-stimulus (control) period $t_{\mathrm{pre}} \subseteq t$, while that between 0 ms and 1000 ms was regarded as a post-stimulus (task) period $t_{\mathrm{pos}} \subseteq t$. Trials of which eye-movement artifact was larger than 100 μV were omitted from the analyses. Because EEGs at the outermost electrodes (gray electrodes in Figure 4.2) contained large noise signals, the outermost electrodes were excluded from the analyses.

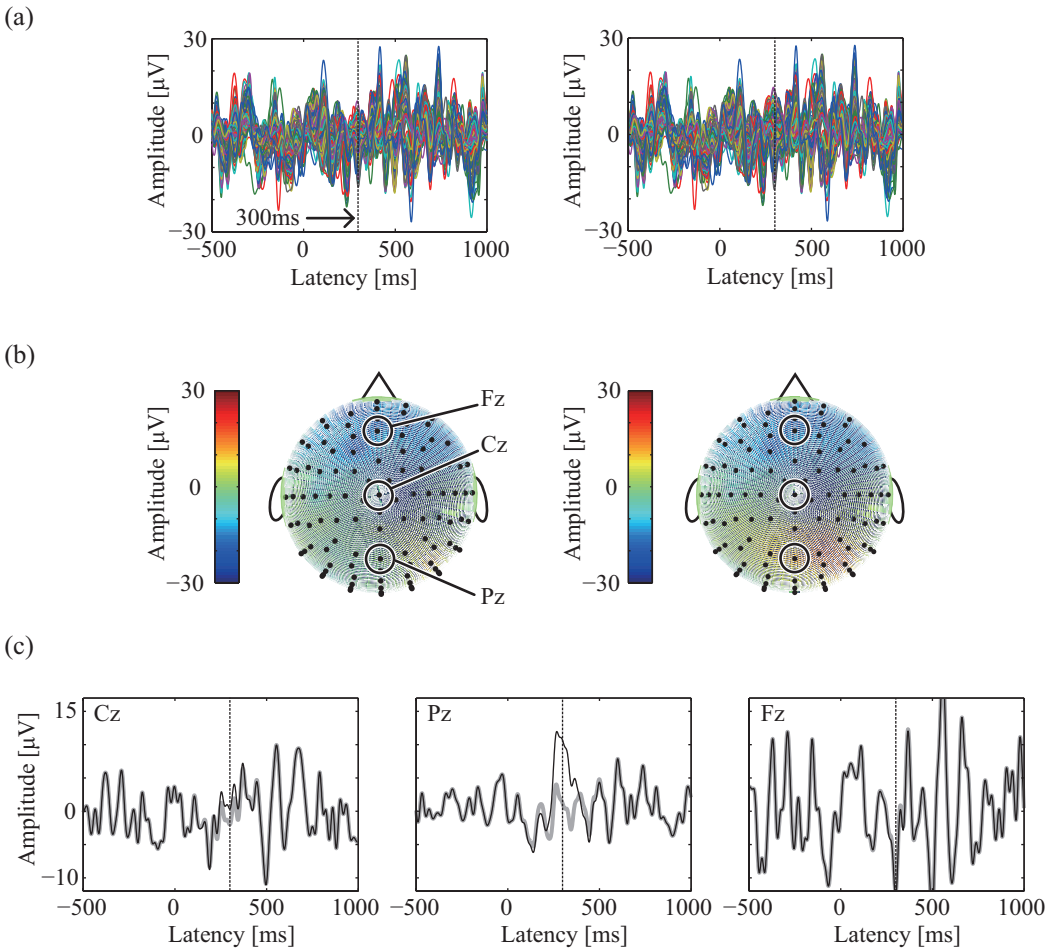

Figure 4.5: (a) Superposition of representative waveforms of background EEGs at 108 electrodes (left) and of simulated EEGs at 108 electrodes (right). (b) Scalp topographies of background EEGs at 300 ms in (a) (left) and of simulated EEGs at 300 ms in (a) (right). (c) Waveforms of ERP (black) superimposed with background EEG (gray) at Cz, Pz and Fz (in the case where $\alpha = 12.0$).

4.3.4 Creation of pseudo-EEGs with ERP

P300 is a typical ERP component that reflects cognitive brain activities and its observations are mainly centered at the midline parietal scalp area [13]. P300 is elicited largely for target stimulus in visual and/or auditory oddball experiments. We made a template of a dipole moment for P300, which was a half sinusoidal wave of 2.5 Hz and had its peak at $T_{\mathrm{P300}} = 300$ ms (Figure 4.4 (a)). Here, P300 measured by 108-channels was simulated by two equivalent current dipoles, which were perpendicular to electrodes ♯5 and ♯32 (Figure 4.2), and with a single-layer sphere head model (center: [0.0 mm, 0.0 mm, 0.0 mm], radius: 80 mm, electric conductivity: 0.35 S/m, see Figure 4.4 (c)). The two dipoles were located at [-13.5 mm, -32.6 mm, 42.2 mm] and [13.5 mm, -32.6 mm, 42.2 mm], and their orientations were [-0.25, -0.59, 0.77] and [0.25,

-0.59, 0.77], respectively.

First, 108-channel scalp potentials $\mathbf{V}_{\mathrm{ERP}}(t)$, which was a true ERP, were obtained by solving a forward problem and that example waveforms were shown in Figure 4.4 (b). $\mathbf{V}_{\mathrm{ERP}}(t)$ had its maximum value at an electrode Pz (electrode ♯17 in Figure 4.2). Second, segmented background EEGs $\mathbf{V}^m_{\mathrm{EEG}}(t)$ as 80 trials ($m = 1, ..., M$, here, $M = 80$) of 1500 ms were randomly extracted from EEGs described in **Experiment 2**. Finally, a simulated 108-channel scalp potential $\mathbf{V}^m_{\mathrm{SIM}}(t)$ was made using $\mathbf{V}_{\mathrm{ERP}}(t)$ and $\mathbf{V}^m_{\mathrm{EEG}}(t)$, as follows:

$$\mathbf{V}^m_{\mathrm{SIM}}(t) = \underset{0.5-35}{\mathrm{BPF}} \left\{ \mathbf{V}^m_{\mathrm{EEG}}(t) + \frac{\alpha}{v_{\mathrm{ERP/Pz}}(T_{\mathrm{P300}})} \cdot \mathbf{V}_{\mathrm{ERP}}(t) \right\} \tag{4.5}$$

where $v_{\mathrm{ERP/Pz}(t)}$ denotes the ERP at a Pz of $v_{\mathrm{ERP}(t)}$ and $\underset{0.5-35}{\mathrm{BPF}}$ denotes digital filtering with a zero-phase shift band-pass from 0.5 Hz to 35 Hz. α was set to 4.0, 6.0, 8.0, 10.0, and 12.0 (μV), and SNR was defined by

$$\mathrm{SNR} = \frac{1}{M} \sum_{m=1}^{M} \frac{\mathrm{std}\left(\alpha \cdot v_{\mathrm{ERP/Pz}}(t_{\mathrm{pos}})\right)}{\mathrm{std}\left(v^m_{\mathrm{EEG/Pz}}(t_{\mathrm{pos}})\right)} \tag{4.6}$$

where std calculates the standard deviation and $v^m_{\mathrm{EEG/Pz}}(t_{\mathrm{pos}})$ denotes the scalp potential at Pz. The example waveforms and the scalp potentials at 300 ms of $\mathbf{V}^m_{\mathrm{EEG}}(t)$ and $\mathbf{V}^m_{\mathrm{SIM}}(t)$ were shown in Figures 4.5 (a) and (b). Figure 4.5 (c) showed the example waveforms of $\mathbf{V}^m_{\mathrm{EEG}}(t)$ and $\mathbf{V}^m_{\mathrm{SIM}}(t)$ ($\alpha = 12.0$) at Cz (electrode ♯1 in Figure 4.2), Pz and Fz (electrode ♯72 in Figure 4.2). The SNRs were 0.44, 0.65, 0.87, 1.09, and 1.31 for $\alpha = 4.0$, 6.0, 8.0, 10.0, and 12.0, respectively.

4.3.5 Evaluation of removal methods by simulated ERP data

The proposed method was applied to an 80-trial $\mathbf{V}_{\mathrm{SIM}}(t)$ to obtain noise-reduced ERPs $\mathbf{V}_{\mathrm{CLE}}(t)$ for each α. For the index that evaluated the performance of the proposed method, we employed the RMSE, amplitude deviation and latency deviation as we know the time course of the simulated ERP. Each value at the nth channel was given as

RMSE:

$$\psi_n = \sqrt{\frac{1}{M} \sum_{m=1}^{M} \frac{1}{1024} \sum_{t \in t_{\mathrm{pos}}} \left(v^m_n(t) - v_{\mathrm{ERP}/n}(t)\right)^2} \tag{4.7}$$

where 1024 is the number of samples among t_{pos}.

Amplitude deviation:

$$\sigma^v_n = \left| \frac{1}{M} \sum_{m=1}^{M} v^m_n(T_{\mathrm{P300}}) - v_{\mathrm{ERP}/n}(T_{\mathrm{P300}}) \right| \tag{4.8}$$

Latency deviation:

$$\sigma_n^t = \left| t_n^{\text{peak}} - T_{\text{P300}} \right| \tag{4.9}$$

where $v_n^m(t)$ denotes the scalp potential at the nth channel of $\mathbf{V}_{\text{CLE}}^m(t)$ or $\mathbf{V}_{\text{SIM}}^m(t)$, and t_n^{peak} denotes the peak latency at the nth channel of 80-trial averaged $\mathbf{V}_{\text{CLE}}^m(t)$ or $\mathbf{V}_{\text{SIM}}^m(t)$. In this simulation, we selected five electrodes (Pz and four electrodes, ♯4, ♯5, ♯18, and ♯28, shown as black electrodes in Figure 4.2), which had a relatively large amplitude of ERP (see Figure 4.5), for calculating ψ_n, σ_n^v and σ_n^t. Distributions of ψ_n, σ_n^v and σ_n^t corresponding to $\mathbf{V}_{\text{CLE}}^m(t)$ or $\mathbf{V}_{\text{SIM}}^m(t)$ obtained by the removal methods of all five electrodes and all SNRs were compared using Wilcoxon signed-rank test. Lower ψ_n, σ_n^v and σ_n^t indicate a better time course estimation of ERP. In addition, to evaluate the proposed method, we obtained ERPs that were normalized by their standard deviations at pre-trigger periods as follows:

$$\gamma_n(t) = \frac{\frac{1}{M}\sum_{m=1}^{M} v_n^m(t)}{\text{std}\left(\frac{1}{M}\sum_{m=1}^{M} v_n^m(t_{\text{pre}})\right)} \tag{4.10}$$

$\gamma_n(t)$ for all electrodes was visualized by a channel–latency plot which has been used for examining trial-to-trial similarities and differences in EEG dynamics at one electrode [14]. Furthermore, PCEM (principal component elimination method), which was a previous denoising method based on PCA [8], was also applied to simulated ERP data to evaluate the proposed method.

4.3.6 Evaluation of removal methods by measured ERP data

The proposed method and PCEM were applied to 80-trial measured ERP data measured in **Experiment 1** for both target and non-target conditions, and noise-reduced ERPs were estimated. For the evaluation of the proposed method, we obtained the normalized ERPs using Equation (4.10).

4.4 Results

4.4.1 Simulated ERP data

Figure 4.6 shows example waveforms of a simulated ERP $\mathbf{V}_{\text{ERP}}^m(t)$ and a channel–latency plot of $\gamma_n(t)$ for $\mathbf{V}_{\text{ERP}}^m(t)$. The y-axis of the channel–latency plot represents the channel number (1–108 in Figure 4.2), and data in error channels were removed and shown as white lines. In this figure, a denominator of $\gamma_n(t)$ was set to 1.0. Then, Figure 4.6 became the ideal plot for this simulation.

Figure 4.7 (a) shows the waveforms of conventional averaging ERPs $\bar{\mathbf{V}}_{\text{SIM}}(t) = \sum_{m=1}^{M} \mathbf{V}_{\text{SIM}}^m(t) / M$ and channel–latency plots of $\gamma_n(t)$ for $\bar{\mathbf{V}}_{\text{SIM}}(t)$. $\bar{\mathbf{V}}_{\text{SIM}}(T_{\text{P300}})$ became invisible and some

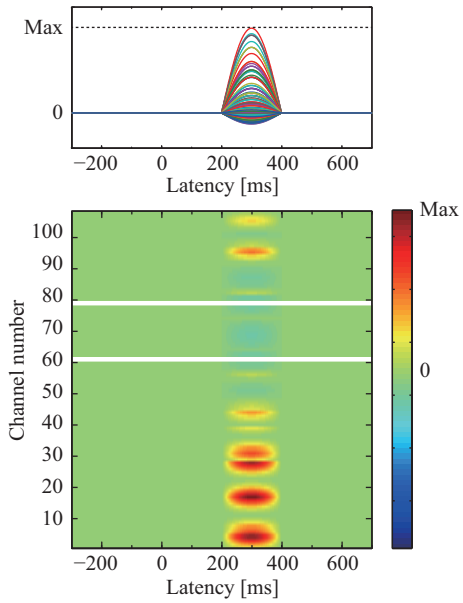

Figure 4.6: Superposition of ERP waveforms at 108 electrodes obtained by solving the forward problem (upper) and their channel–latency plot of time courses sorted by channel number.

vertical stripes representing alpha and beta waves were enhanced with decreased SNR of these simulated EEGs. In other word, the P300 could be detected clearly with increase of SNR.

Figures 4.7 (b) and (c) show the waveforms of trial-averaged noise-reduced ERPs $\bar{\mathbf{V}}_{\mathrm{CLE}}(t) = \sum_{m=1}^{M} \mathbf{V}^m_{\mathrm{CLE}}(t)/M$ and channel–latency plots of $\gamma_n(t)$ for $\bar{\mathbf{V}}_{\mathrm{CLE}}(t)$, which were obtained by both the proposed method and PCEM, respectively. As the SNR of these simulated EEGs increased, both removal methods emphasize the peaks of $\bar{\mathbf{V}}_{\mathrm{CLE}}(T_{\mathrm{P300}})$ more than those of $\bar{\mathbf{V}}_{\mathrm{SIM}}(T_{\mathrm{P300}})$. Although both removal methods appeared to remove noisy background EEGs in waveforms, channel–latency plots showed that the proposed method removed more background EEGs than PCEM, especially for a lower SNR.

Figure 4.8 shows the RMSE, amplitude deviation and latency deviation of $\mathbf{V}^m_{\mathrm{SIM}}(t)$ and $\mathbf{V}^m_{\mathrm{CLE}}(t)$ obtained by a conventional averaging, the proposed method, and PCEM. Statistical analysis showed that the proposed method performed significantly better than the others for all values. As shown in Figure 4.8 (a), the proposed method (mean = 3.08, std = 1.14) had a significantly lower RMSE than that obtained with conventional averaging (mean = 4.15, std = 1.67), $p < 0.001$, and PCEM (mean = 3.71, std = 1.37), $p < 0.001$. In Figure 4.8 (b), the proposed method (mean = 0.26, std = 0.20) had a significantly lower amplitude deviation than that obtained with conventional averaging (mean = 0.36, std = 0.24), $p < 0.001$, and PCEM (mean = 0.47, std = 0.32), $p < 0.001$. In Figure 4.8 (c), the proposed method (mean = 12.85, std = 8.19) had a significantly l ower latency deviation than that obtained with conventional averaging (mean = 17.62, std = 6.47), $p < 0.001$, and PCEM (mean = 15.90, std = 8.09), $p < 0.001$.

Figure 4.7: Superposition of trial-averaged ERP waveforms and channel–latency plots of their $\gamma_n(t)$ for all five SNRs obtained by a conventional averaging, the proposed method, and PCEM. (a) Conventional averaging. (b) Proposed method. (c) PCEM.

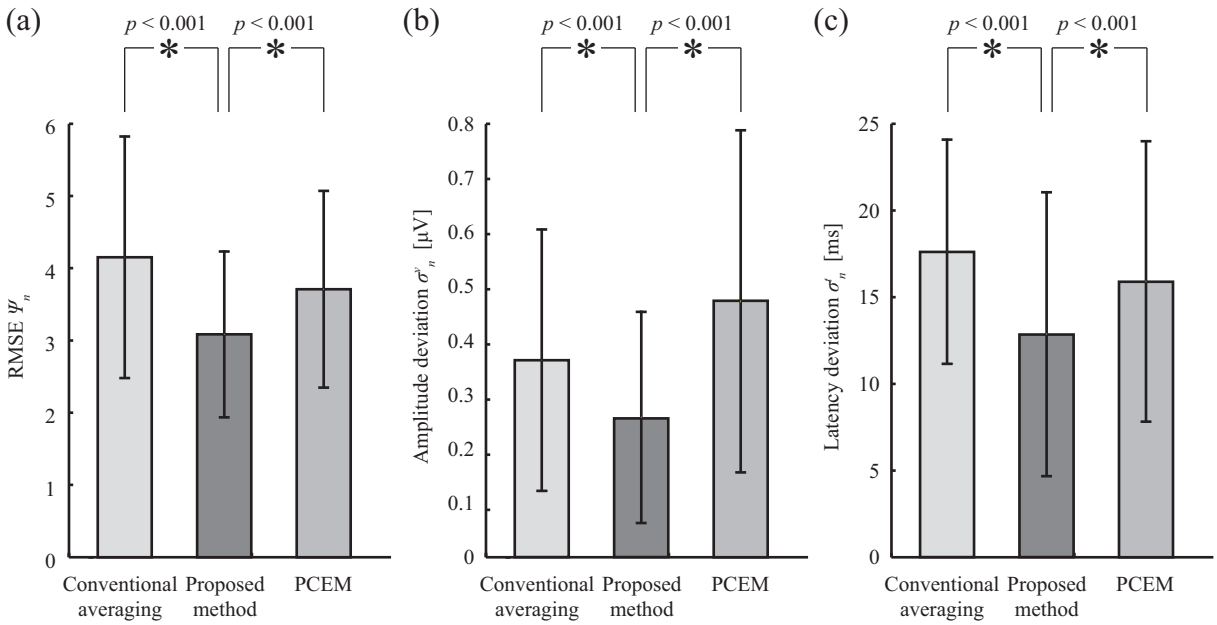

Figure 4.8: The RMSE, amplitude deviation, and latency deviation of the ERPs obtained by conventional averaging, the proposed method, and PCEM. (a) RMSE. (b) Amplitude deviation. (c) Latency deviation.

4.4.2 Measured ERP data

Figure 4.9 (a) shows waveforms of conventional averaging ERPs and channel–latency plots of their $\gamma_n(t)$ for target and non-target conditions for two subjects, while the waveforms of conventional averaging ERPs showed that the amplitude of ERP peaks appeared to be larger than that of control period t_{pre}. However, in channel–latency plots of $\gamma_n(t)$ for conventional averaging ERPs, several prominent vertical stripes, which were considered to be reflected alpha and beta waves, were also seen. These results indicated that background EEGs were not thoroughly removed by the conventional averaging process.

Figures 4.9 (b) and (c) show waveforms of trial-averaged noise-reduced ERPs obtained by both the proposed method and PCEM and channel–latency plots of their $\gamma_n(t)$ of both target and non-target conditions for two subjects. In the waveforms, while PCEM appeared to remove some of the low frequency components of the ERPs and adversely enhance alpha-like waves in both subjects, the proposed method appeared to remove prominent rhythmic activities representing alpha and beta waves, and retain P300, which was a main component of ERPs. In contrast, the waveforms showed that the amplitudes of ERPs obtained by the proposed method were smaller than those of conventional averaging ERPs. Channel-latency plots indicated that the proposed method enhanced the ERP components, especially after 200 ms, when compared with a conventional averaging in both subjects. On the other hand, some of the information of the early components, such as N100 and P200, appeared to be removed in both subjects. How-

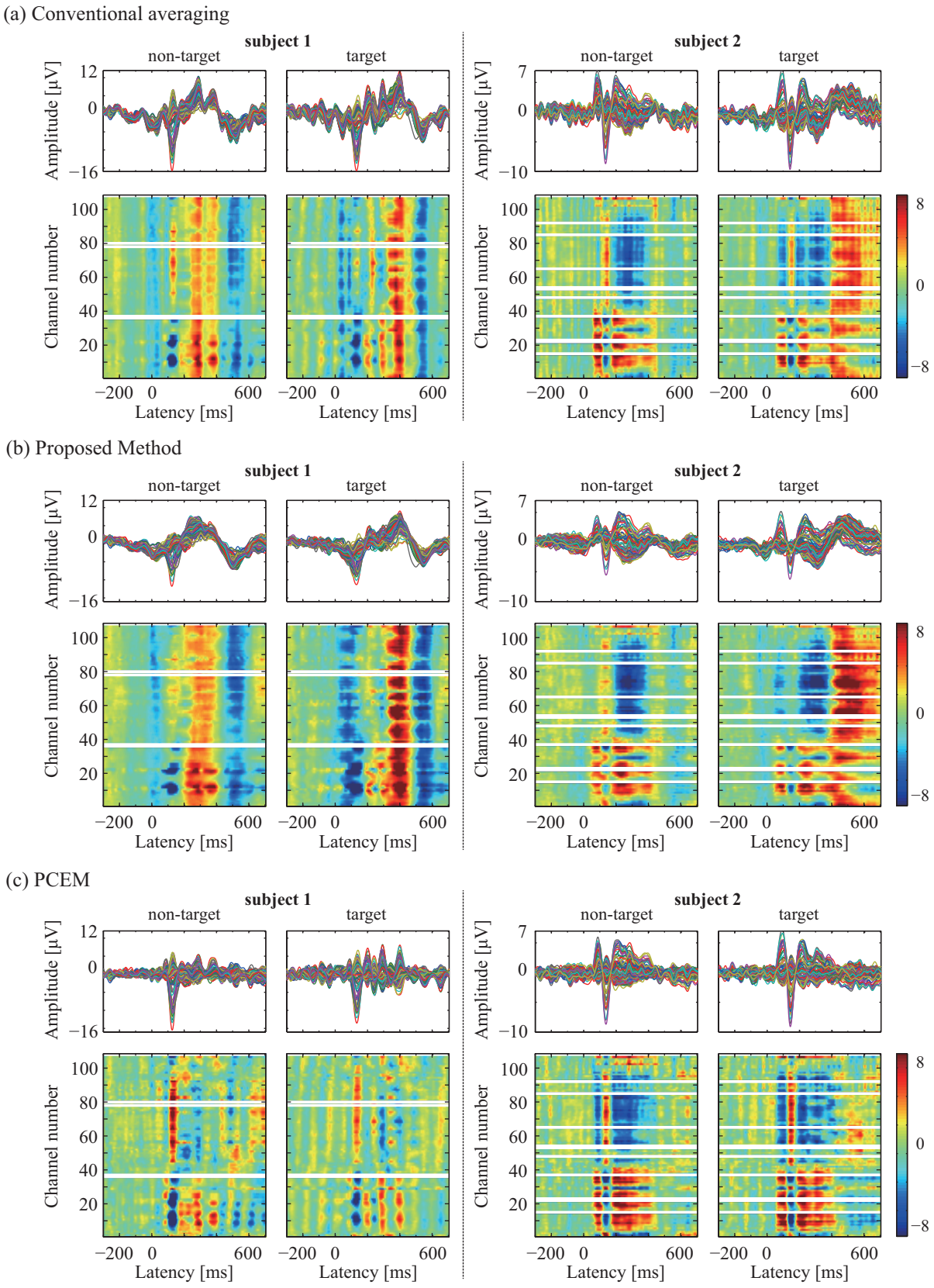

Figure 4.9: Superposition of trial-averaged ERP waveforms and channel-latency plots of their $\gamma_n(t)$ obtained by a conventional averaging, the proposed method, and PCEM of target and nontarget conditions in subjects 1 and 2. (a) Conventional averaging. (b) Proposed method. (c) PCEM.

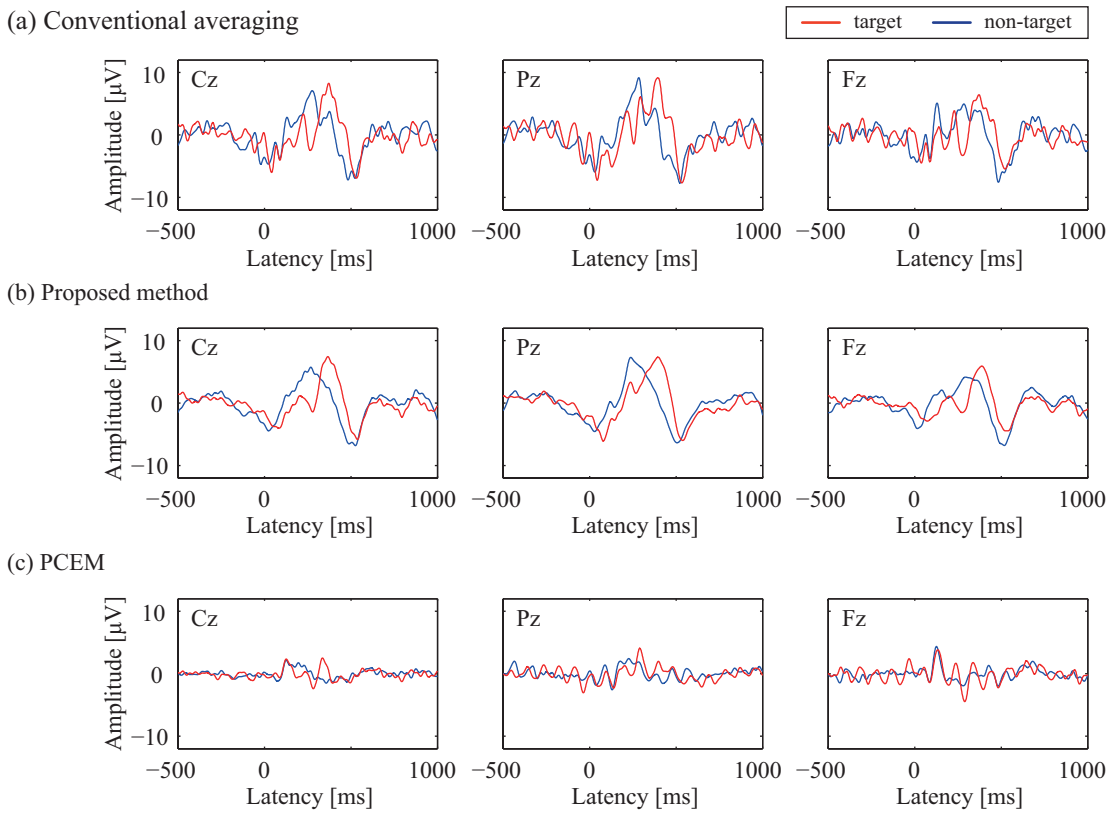

Figure 4.10: Waveforms of conventional averaging ERPs and noise-reduced ERPs obtained by the proposed method and PCEM at Cz, Pz, and Fz in subject 1. Red and blue lines represent target and nontarget conditions, respectively. (a) Conventional averaging. (b) Proposed method. (c) PCEM.

ever, the ERPs on which we focused were late components, and the early components were visible and retained by applying the proposed method.

Figures 4.10 and 4.11 show waveforms of conventional averaging ERPs and noise-reduced ERPs that were obtained by both the proposed method and PCEM at Pz, Cz , and Fz in both subjects. As seen in these figures, oscillatory noises were still superimposed on both conventional averaging ERPs and those obtained by PCEM. Furthermore, noise-reduced ERPs obtained by PCEM lost mainly low frequency components, and the difference between the two conditions was unobservable. On the other hand, noise-reduced ERPs obtained by the proposed method retained P300, and we were able to easily identify the difference between the two conditions because oscillatory noises were substantially removed.

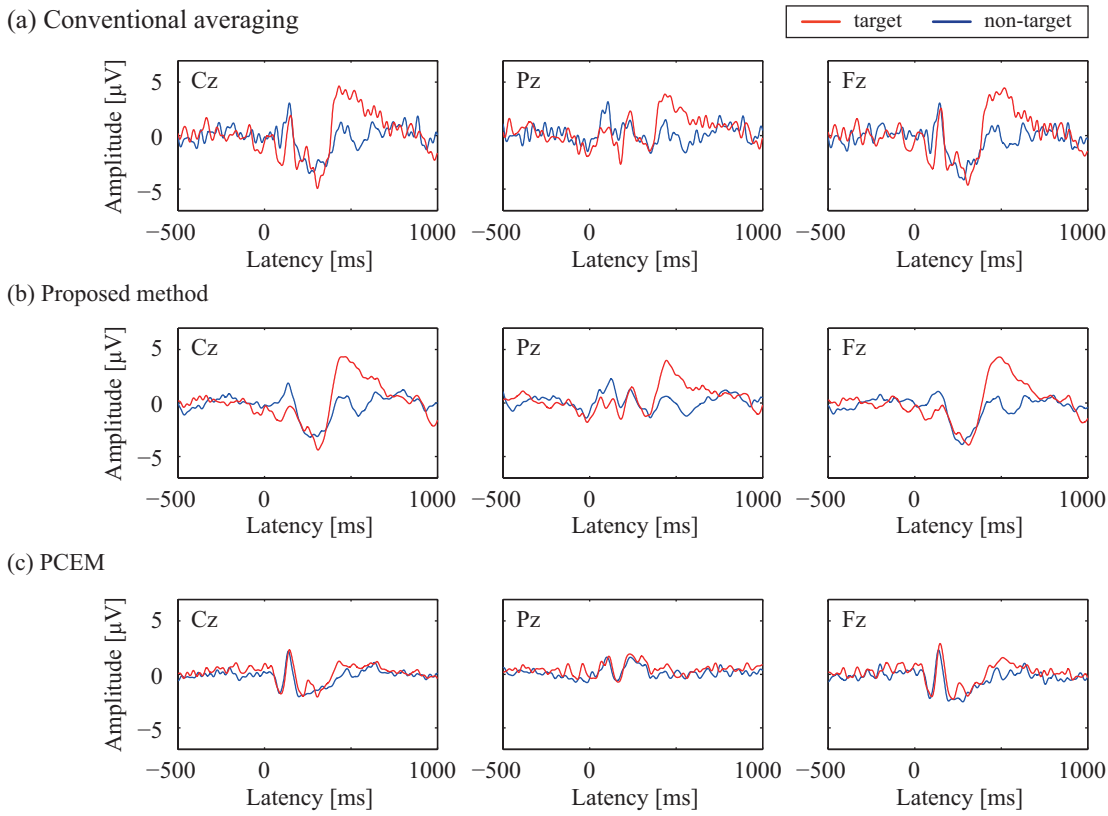

Figure 4.11: Waveforms of conventional averaging ERPs and noise-reduced ERPs obtained by the proposed method and PCEM at Cz, Pz, and Fz in subject 2. Red and blue lines represent target and nontarget conditions, respectively. (a) Conventional averaging. (b) Proposed method. (c) PCEM.

4.5 Discussion

In this study, we proposed a novel method to remove background EEGs and to enhance ERPs based on a combination of PCA and MEMD. PCA reduced the dimensions of multichannel EEGs, whereas MEMD was used as a frequency filter [15] to separate ERP components and noisy background EEGs. Although the simulation was relatively simple, it demonstrated that the proposed method had the best performance when compared with conventional averaging and PCEM for all SNRs. In addition, the proposed method appeared to remove noisy background EEGs and retain ERP components according to the results for measured ERPs.

On the other hand, although PCEM showed good results for simulated data, it also significantly reduced the ERP information for the measured data. This is believed to be due to the difference between MEG and EEG recordings because PCEM was proposed to improve the SNR of evoked fields measured by MEG [8], In other words, MEG directly measures magnetic fields generated by the electric activities of neurons, whereas EEG measures scalp electric potentials via volume conduction. It was therefore difficult for PCEM to separate ERPs from

alpha and beta waves because of their similar scalp distributions. These results demonstrated the advantage of the proposed method over conventional averaging and PCEM methods.

In the measured EEG data, the amplitudes of early ERP components were decreased by applying the proposed method. The proposed method may concurrently remove several early ERP components with noisy background EEGs, because early ERP components appeared to include components that were about 10 Hz, which is similar to the frequency of alpha waves. However, it is still not clear whether such early ERP components are generated by synchronization of spontaneous EEG rhythms such as alpha waves, or if they are independent [16, 17, 18, 19], because the previous reported results are not consistent. The validity of the denoising of early ERP components using the proposed method is therefore a subject of future investigation.

Williams et al. [1] applied EMD to a single channel EEG with a priori knowledge that ERP had a frequency less than 10 Hz. However, their method requires the selection of threshold frequencies which represent ERP components. In contrast, the proposed method requires only simple a priori knowledge that the noisy background EEGs had a peak that was mainly at 8–35 Hz. In other words, Williams et al. [1] focused on extracting ERP, whereas we focused on denoising background EEGs. This is the reason why simple a priori knowledge is sufficient in the proposed method.

Previous methods that were based on other frequency filters mainly used a wavelet transform to denoise ERPs which required specific a priori knowledge for denoising, e.g., accurate peak latencies of ERP and conventional averaging ERP waveforms [20, 21, 22]. The a priori knowledge may lead to the enhancement of untrue components that are not ERPs, if the background EEGs are much bigger than ERPs, or if the number of trials is inadequate and the waveforms of conventional averaging ERPs are noisy. On the other hand, the proposed method requires the simple a priori knowledge given above, and is a robust approach when compared with the other denoising methods that are based on wavelet transform.

In conclusion, although further improvement of the proposed method is necessary, results for simulated and measured data in this study indicated that the proposed method with only simple a priori knowledge (regardless of the subject) is promising for the denoising of multichannel-recorded ERPs, especially late components.

References

[1] Williams, N., Nasuto, S. J., & Saddy, J. D. (2011). Evaluation of empirical mode decomposition for event-related potential analysis. EURASIP Journal on Advances in Signal Processing, 2011, 11 pages.

[2] Kutas, M., & Hillyard, S. A. (1980). Reading between the lines: Event-related brain potentials during natural sentence processing. Brain and Language, 11(2), 354–373.

[3] Olofsson, J. K., Nordin, S., Sequeira, H., & Polich, J. (2008). Affective picture processing: an integrative review of ERP findings. Biological psychology, 77(3), 247–265.

[4] Cerutti, S., Baselli, G., Liberati, D., & Pavesi, G. (1987). Single sweep analysis of visual evoked potentials through a model of parametric identification. Biological cybernetics, 56(2-3), 111–120.

[5] Celka, P., Le, K. N., & Cutmore, T. R. (2008). Noise reduction in rhythmic and multitrial biosignals with applications to event-related potentials. Biomedical Engineering, IEEE Transactions on, 55(7), 1809–1821.

[6] Abootalebi, V., Moradi, M. H., & Khalilzadeh, M. A. (2009). A new approach for EEG feature extraction in P300-based lie detection. Computer methods and programs in biomedicine, 94(1), 48–57.

[7] Georgiadis, S. D., Ranta-aho, P. O., Tarvainen, M. P., & Karjalainen, P. A. (2005). Single-trial dynamical estimation of event-related potentials: a Kalman filter-based approach. Biomedical Engineering, IEEE Transactions on, 52(8), 1397–1406.

[8] Kobayashi, T., & Kuriki, S. (1999). Principal component elimination method for the improvement of S/N in evoked neuromagnetic field measurements. Biomedical Engineering, IEEE Transactions on, 46(8), 951–958.

[9] Lemm, S., Curio, G., Hlushchuk, Y., & Muller, K. R. (2006). Enhancing the signal-to-noise ratio of ICA-based extracted ERPs. Biomedical Engineering, IEEE Transactions on, 53(4), 601–607.

[10] Hu, L., Mouraux, A., Hu, Y., & Iannetti, G. D. (2010). A novel approach for enhancing the signal-to-noise ratio and detecting automatically event-related potentials (ERPs) in single trials. NeuroImage, 50(1), 99–111.

[11] Huang, N. E., Wu, M. L. C., Long, S. R., Shen, S. S., Qu, W., Gloersen, P., & Fan, K. L. (2003). A confidence limit for the empirical mode decomposition and Hilbert spectral analysis. Proceedings of the Royal Society of London. Series A: Mathematical, Physical and Engineering Sciences, 459(2037), 2317–2345.

[12] Rehman, N., & Mandic, D. P. (2010). Multivariate empirical mode decomposition. Proceedings of the Royal Society A: Mathematical, Physical and Engineering Science, 466(2117), 1291–1302.

[13] Johnson, R. (1993). On the neural generators of the P300 component of the event ‐ related potential. Psychophysiology, 30(1), 90–97.

[14] Onton, J., Westerfield, M., Townsend, J., & Makeig, S. (2006). Imaging human EEG dynamics using independent component analysis. Neuroscience & Biobehavioral Reviews, 30(6), 808–822.

[15] Flandrin, P., Rilling, G., & Goncalves, P. (2004). Empirical mode decomposition as a filter bank. Signal Processing Letters, IEEE, 11(2), 112–114.

[16] Barry, R. J., Rushby, J. A., Johnstone, S. J., Clarke, A. R., Croft, R. J., & Lawrence, C. A. (2004). Event-related potentials in the auditory oddball as a function of EEG alpha phase at stimulus onset. Clinical neurophysiology, 115(11), 2593–2601.

[17] Klimesch, W., Schack, B., Schabus, M., Doppelmayr, M., Gruber, W., & Sauseng, P. (2004). Phase-locked alpha and theta oscillations generate the P1–N1 complex and are related to memory performance. Cognitive Brain Research, 19(3), 302–316.

[18] Gruber, W. R., Klimesch, W., Sauseng, P., & Doppelmayr, M. (2005). Alpha phase synchronization predicts P1 and N1 latency and amplitude size. Cerebral Cortex, 15(4), 371–377.

[19] Risner, M. L., Aura, C. J., Black, J. E., & Gawne, T. J. (2009). The Visual Evoked Potential is independent of surface alpha rhythm phase. Neuroimage, 45(2), 463–469.

[20] Bartnik, E. A., Blinowska, K. J., & Durka, P. J. (1992). Single evoked potential reconstruction by means of wavelet transform. Biological Cybernetics, 67(2), 175–181.

[21] Quiroga, R. Q., & Garcia, H. (2003). Single-trial event-related potentials with wavelet denoising. Clinical Neurophysiology, 114(2), 376–390.

[22] Iyer, D., & Zouridakis, G. (2007). Single-trial evoked potential estimation: comparison between independent component analysis and wavelet denoising. Clinical Neurophysiology, 118(3), 495–504.

Chapter 5

An extraction of EEG rhythmic activities

Neural activations can be measured based on modulation of EEG rhythmic activities within specific frequency bands. In this study, we propose a method that combines MEMD with the Hilbert transform, rather than a wavelet transform, to extract rhythmic activities more precisely and to visualize them more clearly. The performance of the method was validated using measured EEG data obtained by a wrist movement experiment. The results demonstrated that the proposed method can extract and visualize multi-channel EEG rhythmic activities with higher resolution than a method employing the STFT and the wavelet transform.

5.1 Background

Several efficient methods of analysis have been used to quantify or visualize event-related power changes (ERD and ERS) in the frequency or time–frequency domain. Previous studies have typically extracted EEG rhythmic activities using conventional Fourier based methods [1, 2]. However, for use of Fourier based methods, e.g. the STFT, the data must be assumed to be piecewise stationary since the method relies on traditional Fourier decomposition in which signals are represented by infinite length sine waves. This assumption is not always justified for non-stationary data such as EEGs. For wavelet analysis, the problem is its non-adaptive nature. Once the basic wavelet function has been selected, all data must henceforth be analyzed by it. Additionally, since the most commonly used Morlet wavelet is Fourier based, the method also suffers the many shortcomings of Fourier spectral analysis. Thus, these longstanding traditional methods inherit the well-known problem of poor time–frequency localization associated with standard spectrum estimations [3].

To overcome the problems outlined, Huang et al. [3] presented the HHT and compared the HHT with wavelet analysis and showed that the Hilbert representation gives a much sharper frequency resolution and a more precise location in time than that of wavelet analysis. While wavelet analysis gives a uniform frequency resolution, the resolution is also uniformly poor. However, the HHT is mainly applicable to univariate signals because EMD is a univariate de-

composition method. Although MEMD has recently been used to analyze EEGs [4, 5], little research using MEMD for EEG analysis has been conducted, especially for ERD/ERS analysis.

In addition, while numerous methods using the HHT to observe EEG rhythmic activities exist, there is no coincident method to visualize the Hilbert–Huang spectrum. One of the basic features of ERD/ERS measurements in conjunction with Fourier based spectrum visualization is that the EEG power within identified fixed frequency bands is displayed relative to the power of the same EEG derivations recorded during the reference or baseline period several hundred ms before the event occurs [6]. However, it is well established that complex biological systems, like the brain, do not produce oscillations within fixed frequency bands [5] Because the Hilbert spectrum from the IMF visualizes those intrawave frequency modulations, it is simply not possible to conduct ERD/ERS measurements with Hilbert spectrum visualization to visualize the increase and decrease of the power in the same manner as is done for Fourier based spectrum visualization.

5.2 Precise extraction of alpha rhythms

We propose a novel method using MEMD and Hilbert spectrum analysis to extract and visualize ERD/ERS within an alpha frequency band. The proposed method can extract ERD/ERS more precisely and visualize changes more clearly than that using wavelet analysis. The proposed method consists of the following six steps:

Step 1 MEMD decomposes N channel EEG data $\mathbf{V}(t) = [v_1(t), ..., v_n(t), ..., v_N(t)]$ (for $n = 1, ..., N$) to obtain Q sets of IMFs $\mathbf{D}(t) = [\mathbf{d}_1(t), ..., \mathbf{d}_q(t), ..., \mathbf{d}_Q(t)]$, where $\mathbf{d}_q(t) = [d_{1,q}(t), ..., d_{n,q}(t), ..., d_{N,q}(t)]$ (for $q = 1, ..., Q$, and Q varies by trials).

Step 2 With the Hilbert transform, we can get the Hilbert transform of IMF $d_{n,q}(t)$, $\underline{d}_{n,q}(t)$ as

$$\underline{d}_{n,q}(t) = \frac{1}{\pi} C \int_{-\infty}^{\infty} \frac{d(t')}{t - t'} \mathrm{d}t', \tag{5.1}$$

where C indicates the Cauchy principal value. Then, the analytic signal $z_{n,q}(t)$ of extracted IMF $d_{n,q}(t)$ is defined as

$$z_{n,q}(t) = d_{n,q}(t) + j\underline{d}_{n,q}(t) = a_{n,q}(t)e^{j\theta_{n,q}}(t) \tag{5.2}$$

where $a_{n,q}(t) = \left(d_{n,q}^2(t) + \underline{d}_{n,q}^2(t)\right)^{1/2}$, and $\theta_{n,q} = \arctan\left(\underline{d}_{n,q}(t)/d_{n,q}(t)\right)$. Here $a_{n,q}(t)$ is the instantaneous amplitude, and the instantaneous frequency is simply denoted as $f_{n,q}(t) = \mathrm{d}\theta_{n,q}(t)/\mathrm{d}t$.

Step 3 The ordinary Hilbert spectrum $H_{n,q}(t, f)$ of the IMF is calculated as

$$H_{n,q}(t, f) = \begin{cases} a_{n,q}(t) & f_{n,q}(t) = f \\ 0 & \text{otherwise.} \end{cases} \tag{5.3}$$

With the Hilbert spectrum defined, the marginal spectrum $h_{n,q}(f)$ is also defined as [2]

$$h_{n,q}(t, f) = \int_T^0 H_{n,q}(t, f)\mathrm{d}t. \tag{5.4}$$

where T is a total data length of 2800 ms. The marginal spectrum provides a measure of total amplitude contribution from each frequency f [3].

Step 4 All P sets ($P \leq Q$) of IMFs for which the peak frequencies obtained from the marginal spectrum $h_{n,q}(f)$ of all $d_{n,q}(t)$ are between 8 Hz to 13 Hz were extracted from Q sets of IMFs $\mathbf{D}(t)$ as reflecting alpha oscillations and denoted as $\mathbf{d}_p(t) = [d_{1,p}(t), ..., d_{n,p}(t), ..., d_{N,p}(t)]$ (for $p = 1, ..., P$, and P varies by trials). Here, the peak frequency is calculated from the marginal spectrum.

Step 5 The calculated Hilbert spectrum of IMF $d_{n,p}(t)$ reflecting alpha oscillation is corrected by subtracting the baseline amplitude from the entire amplitude as

$$\hat{H}_{n,q}(t, f) = \begin{cases} a_{n,q}(t) - \text{mean}\left(a_{n,q}(t_{\text{base}})\right) & f_{n,q} = f \\ 0 & \text{otherwise,} \end{cases} \tag{5.5}$$

where the function mean( ) calculates the time average.

Step 6 **Steps 1**–**5** were applied to each trial. Finally, the trial-averaged EEG oscillations were obtained by

$$\overline{\hat{H}_n(t, f)} = \frac{1}{M} \sum_{m=1}^{M} \sum_{p=1}^{P} \hat{H}_{n,p}(t, f), \tag{5.6}$$

where $m = 1, ..., M$ is the trial number. After **Step 6**, the obtained spectra $\overline{\hat{H}_n(t, f)}$ were visualized as a time–frequency map.

5.3 Extraction of EEG rhythmic activities by using the short time Fourier analysis

To validate the proposed method, the short time Fourier analysis was applied to the same EEG data and the results were compared to those of the proposed method. Then, the extraction methods using the Fourier transform is composed of the following three steps:

Step 1 The STFT of the uni-channel EEG data $v_n(i_t)$ (i_t is a sampling index in t) is defined as

$$V_n(t', \omega_k) = e^{-j\omega_k t' R} \sum_{i=-D/2}^{D/2-1} v_n(i_t + t'R) w(i_t) e^{-j\omega i_t}, \tag{5.7}$$

where $w(i)$ is a window function, R is a hop size between successive window functions, D is the number of discrete Fourier transform samples, $\omega_k = 2\pi k/D$ ($k = 0, 1, ..., D-1$), and k is a discrete index of frequencies. The power was calculated from the complex result as

$$X_n(t', \omega_k) = |V_n(t', \omega_k)|^2. \tag{5.8}$$

Step 2 The spectrum calculated by the STFT (STFT spectrum) is then corrected by subtracting the baseline amplitude from the entire amplitude as follows.

$$\hat{X}_n(t', f_k) = X_n(t', f_k) - \text{mean}(X_n(t'_{\text{base}}, f_k)), \tag{5.9}$$

where f_k is a frequency corresponding to the discrete index k, $t'_{\text{base}} = \{1, 2, ..., t''\}$ which $t''R$ was the largest value in $t'_{\text{base}}R$ and less than the number of samples in t'_{base}.

Step 3 Baseline corrected STFT spectra were calculated for all 30 channels of all trials. Finally, trial-averaged EEG oscillations were obtained by

$$\overline{\hat{X}_n(t', f_k)} = \frac{1}{M} \sum_{m=1}^{M} \hat{X}_n(t', f_k). \tag{5.10}$$

After **Step 3**, the obtained spectra were visualized as a time–frequency map and we only have to observe (f_α = 8–13 Hz) If we would like to extract alpha rhythms.

Here, we employed 1000 ms Gaussian window (Equation (2.34) described in 2.3.1, and its standard deviation was $\sigma = 50$) as a window function $w(i_t)$ with overlap 0.9 of its length, e.g. window length is 256 samples and $R = 26$ samples. In addition, we set D to 512 samples to interpolate the frequency data.

5.4 Extraction of EEG rhythmic activities by using wavelet analysis

To validate the proposed method, standard wavelet analysis was applied to the same EEG data and the results compared to that of the proposed method. For the wavelet analysis, a family of Morlet wavelets was constructed with 0.5 Hz frequency intervals ranging from 5 Hz to 25 Hz to compute the time varying energy in a frequency band. The complex Morlet wavelet is given by the following function

$$\psi(t, f) = \frac{1}{\sqrt{\sigma_t}\pi^{1/4}} \cdot \exp\left(-\frac{t^2}{2{\sigma_t}^2}\right) \cdot \exp(2\pi j f t), \tag{5.11}$$

where σ_t is a scaling parameter, and $f = f_0/\sigma t$ ($2\pi f_0 = 7$). Then, the extraction methods based on wavelet analysis consists of the following three steps:

Step 1 To compute time varying energy in a frequency band, the uni-channel EEG data $v_n(t)$ is convolved with the corresponding complex wavelet, and the power calculated from the complex result as done using Fourier analysis

$$E_n(t, f) = |\psi(t, f) * v_n(t)|^2 . \tag{5.12}$$

Step 2 The calculated wavelet spectrum is then corrected by subtracting the baseline amplitude from the entire amplitude and trial averaged as follows.

$$\hat{E}_n(t, f) = E_n(t, f) - \text{mean}\,(E_n(t_{\text{base}}, f)) . \tag{5.13}$$

Step 3 Baseline corrected wavelet spectra were calculated for all 30 channels of all trials. Finally, trial-averaged EEG oscillations were obtained by

$$\overline{\hat{E}_n(t, f)} = \frac{1}{M} \sum_{m=1}^{M} \hat{E}_n(t, f). \tag{5.14}$$

After **Step 3**, the obtained spectra were visualized as a time–frequency map and we only have to observe (f_α = 8–13 Hz) if we would like to extract alpha rhythms.

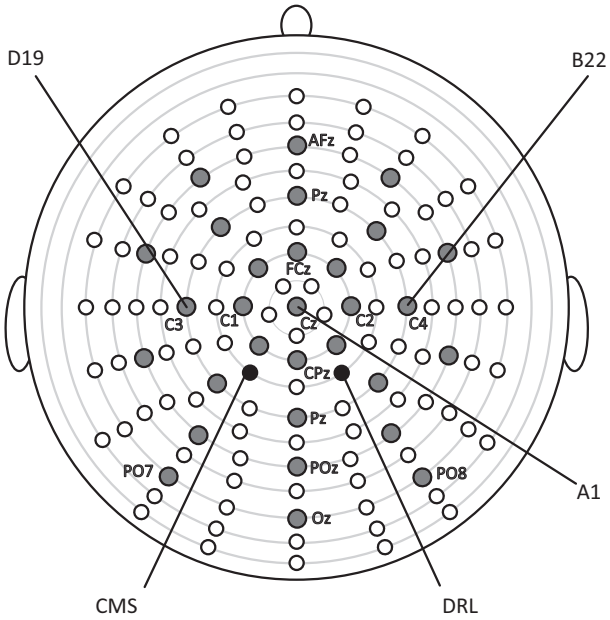

Figure 5.1: Location of the 128 electrodes. Data collected from the 30 gray colored electrodes were used for analysis.

5.5 Application to measured EEG

We applied both methods described in 5.2, 5.3 and 5.4 to measured EEG data recorded from 5 subjects during left wrist movement and compared both performances.

5.5.1 Subjects

Five healthy male subjects (ages: 22–24 years, right-handed) participated in a simple motor task consisting of a self-paced wrist movement. This study was approved by the Ethics Committee, Graduate School of Engineering, Kyoto University, and informed consent was obtained from the subjects after they were given a complete explanation of the study.

5.5.2 EEG measurement

The subjects sat in a comfortable chair approximately 50 cm from a display in a dark room. EEGs were recorded from 128 locations (extended 10–20 system) using a 128-channel digital EEG system (BioSemi Inc., The Netherlands) and sampled at 1024 Hz. Locations of the 128 electrodes, a referenced to CMS electrode and a grounded to DRL electrode are shown in Figure 5.1. The subjects were exposed to two different experimental conditions (Figure 5.2), which were given as *wait* and *move* conditions. Subjects sat passively and observed a fixation visual cue ‘W’ for 3000 ms in the *wait* condition and performed self-paced left wrist movement for 3000 ms following the visual cue ‘L’ in the ‘move’ condition. Each stimulus was presented

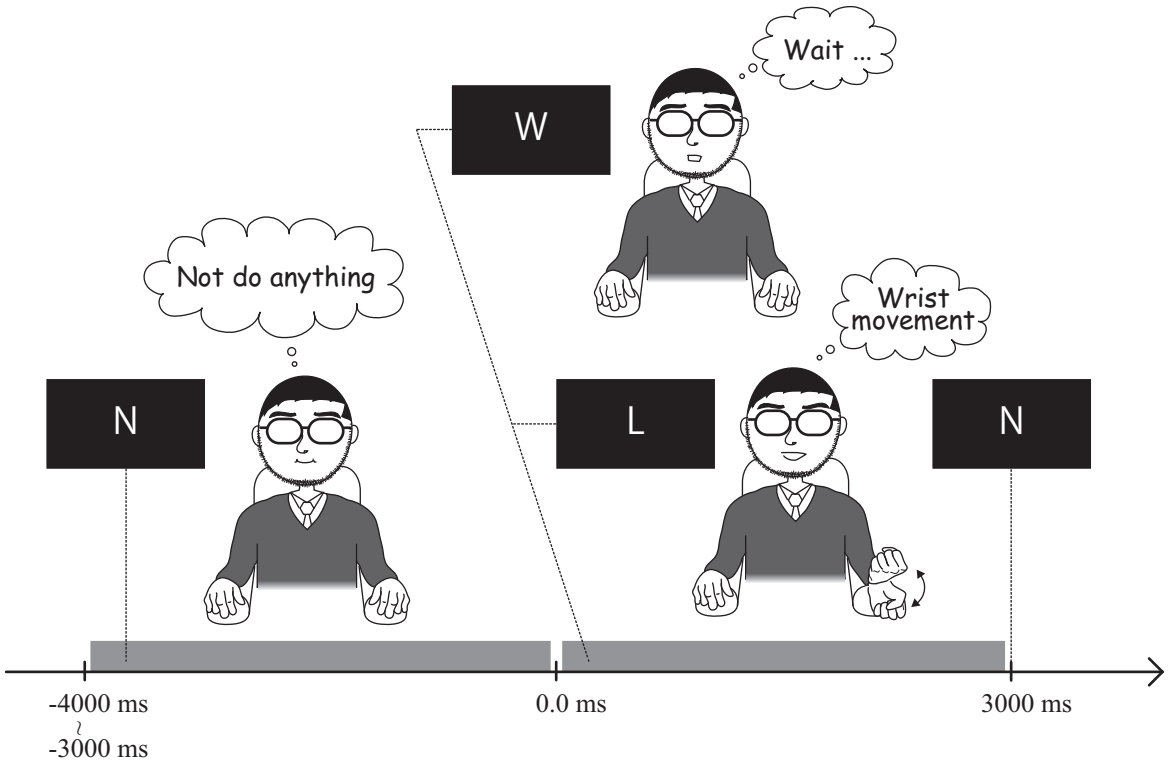

Figure 5.2: Experimental paradigm.

on a black background and subtended a visual angle of $3.5^\circ \times 3.5^\circ$. Subjects sat passively and observed a fixation visual cue 'N' during a 3000–4000 ms interstimulus interval. In total, the subjects executed 200 trials of wait (100 trials) and move (100 trials) conditions.

5.5.3 EEG pre-processing

First, the recorded EEGs in 5.5.2 were re-referenced to the left mastoid and digitally filtered with a zero-phase-shift band-pass from 0.5 Hz to 35 Hz. Subsequently, the filtered EEGs were segmented as epochs using a 2800 ms time interval from −300 ms to 2500 ms following the onset of the visual cue 'L'. The interval between −300 ms and 0 ms was regarded as a baseline period $t_{\text{base}} \subseteq t$. Note that the outermost electrodes that would have exceeded ± 100 μV were excluded from the analysis. In addition, the number of electrodes was limited in the analysis to 30 (the gray colored electrodes in Figure 5.1) because the MEMD performance may diminish with an increase in the number of dimensions [7]. For the 30 electrodes selection, at first, we selected 14 electrodes (the gray color named electrodes in Figure 5.1) whose locations were according to the international 10–20 system. Subsequently, we interpolated 16 electrodes which covered over the whole head in a manner equivalent to 128 electrodes.

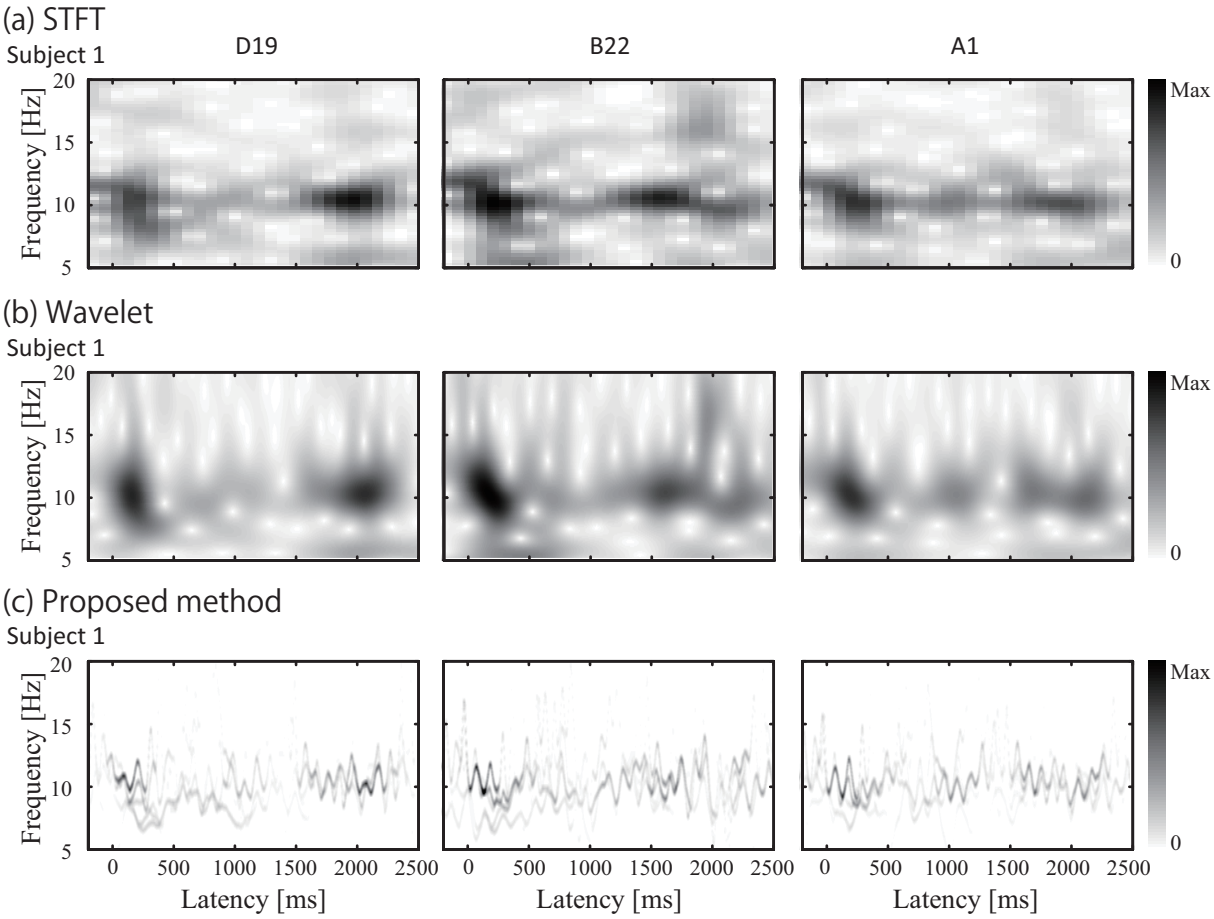

Figure 5.3: Comparison of the proposed method with the short time Fourier and wavelet analyses for EEGs obtained from one trial in subject 1. (a) The STFT spectrum (not subtracting the baseline amplitude), (b) the wavelet spectrum (not subtracting the baseline amplitude) and (c) the ordinary Hilbert spectrum (not subtracting the baseline amplitude) calculated by the proposed method. Gray color coding was normalized by the maximum intensity at B22 electrode.

5.6 Results

Figures 5.3(a) and (b) respectively show examples of the STFT spectrum of EEG oscillations $X_n(t', f_k)$ (not subtracting the baseline amplitude) and the wavelet spectrum of EEG oscillations $E_n(t, f)$ (not subtracting the baseline amplitude) at the three electrodes (D19, B22, and A1 respectively corresponding to C3, C4, and Cz in the international 10–20 system shown in Fig. 1 5.1) from one trial in subject 1 when he was performing left wrist movement. In the wavelet spectrum, neither the energy density nor the frequency is well localized. When the same data are treated by the ordinary Hilbert spectrum of EEG oscillations $H_{n,q}(t, f)$ calculated by the proposed method (not subtracting the baseline amplitude) in Figure 5.3(c), the energy distributions in alpha band are similar to those of wavelet spectrum but well localized in both frequency and time domains. In particular, the Hilbert spectrum captured the intrawave frequency modulation

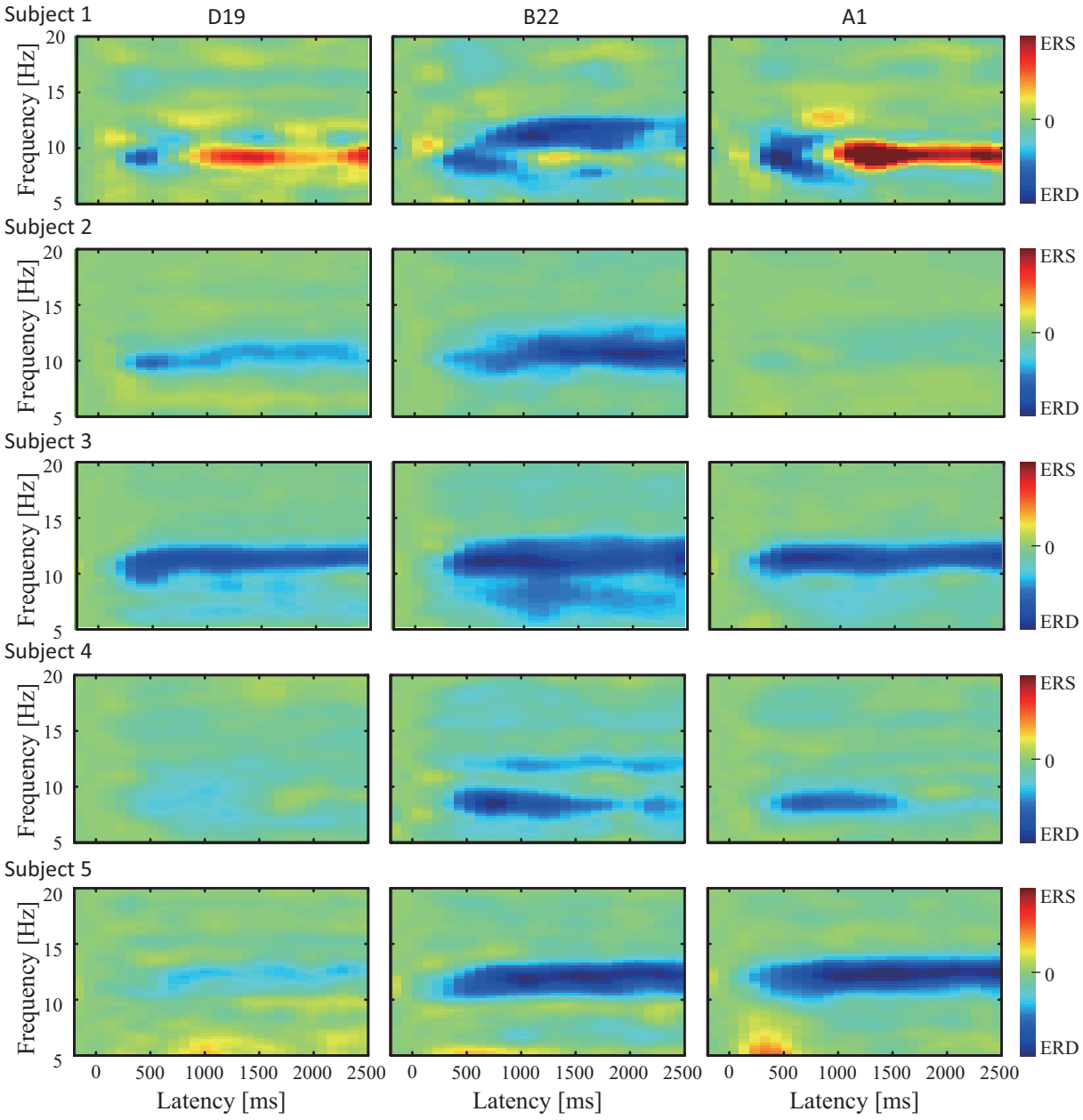

Figure 5.4: The STFT spectrum calculated by the short time Fourier analysis for trial-averaged EEGs obtained from all subjects. In each subject, color coding was normalized by the maximum intensity at B22 electrode.

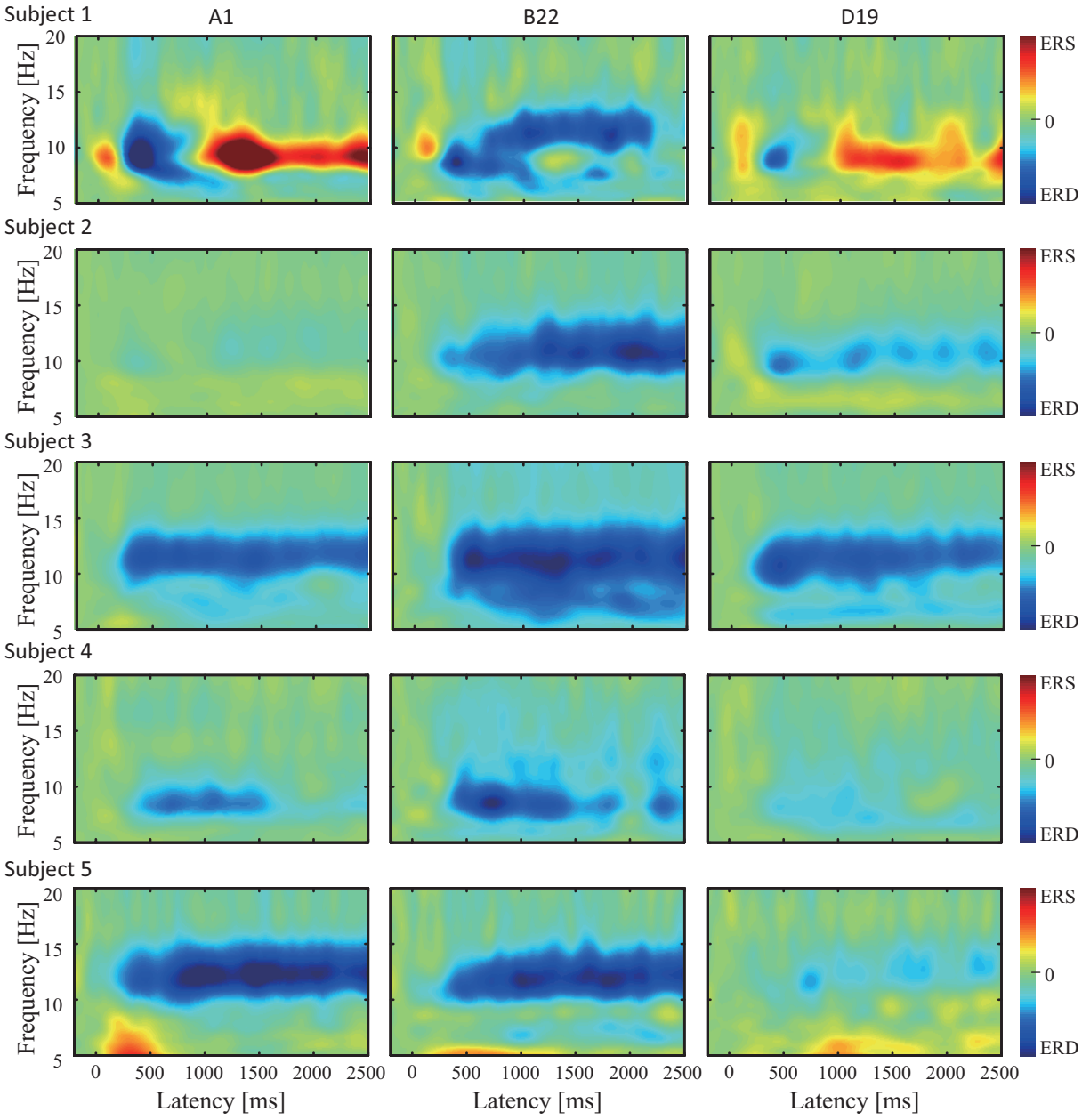

Figure 5.5: The wavelet spectrum calculated by the wavelet analysis for trial-averaged EEGs obtained from all subjects. In each subject, color coding was normalized by the maximum intensity at B22 electrode.

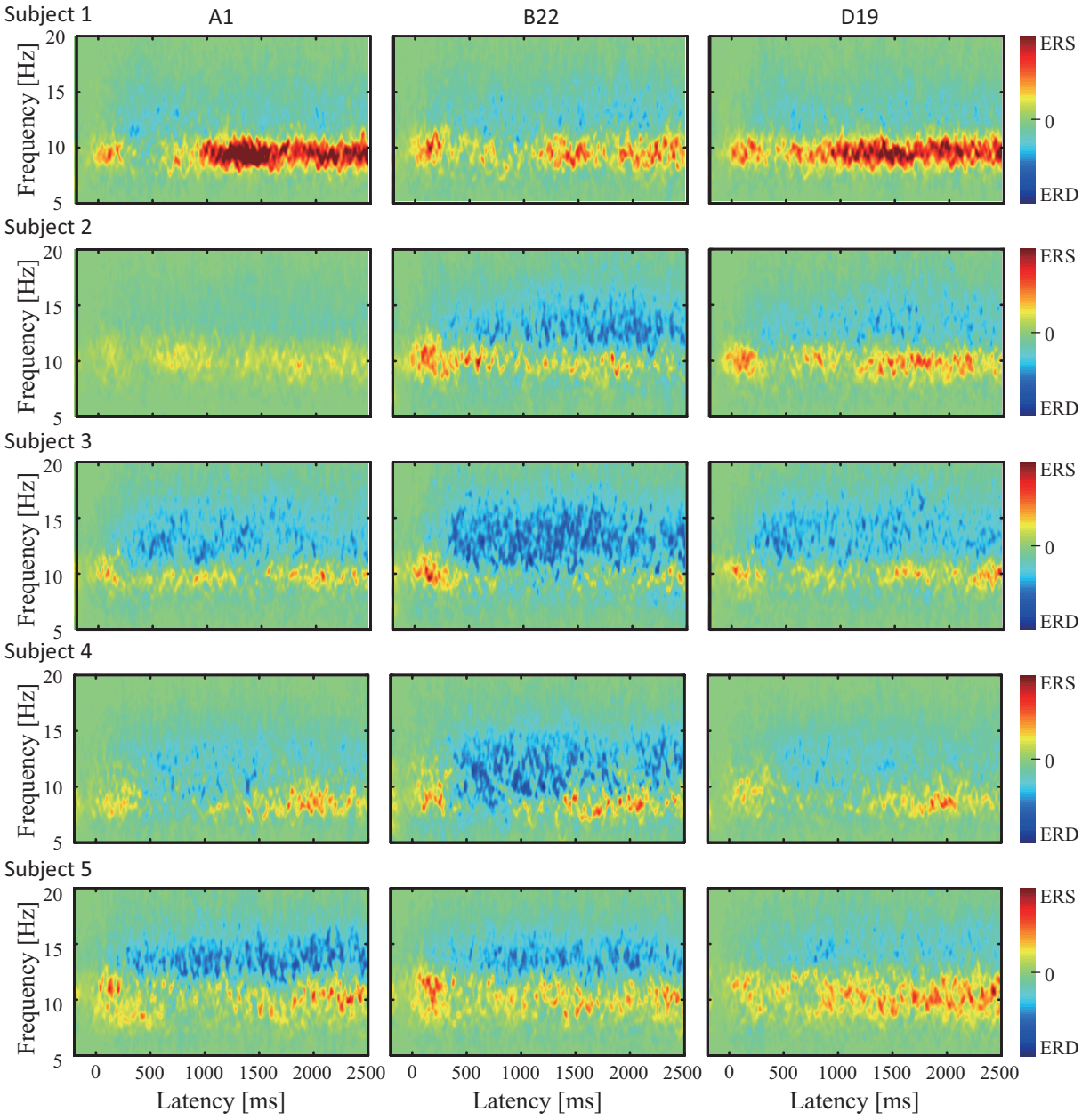

Figure 5.6: The Hilbert spectrum calculated by the proposed method for trial-averaged EEGs obtained from all subjects. In each subject, color coding was normalized by the maximum intensity at B22 electrode.

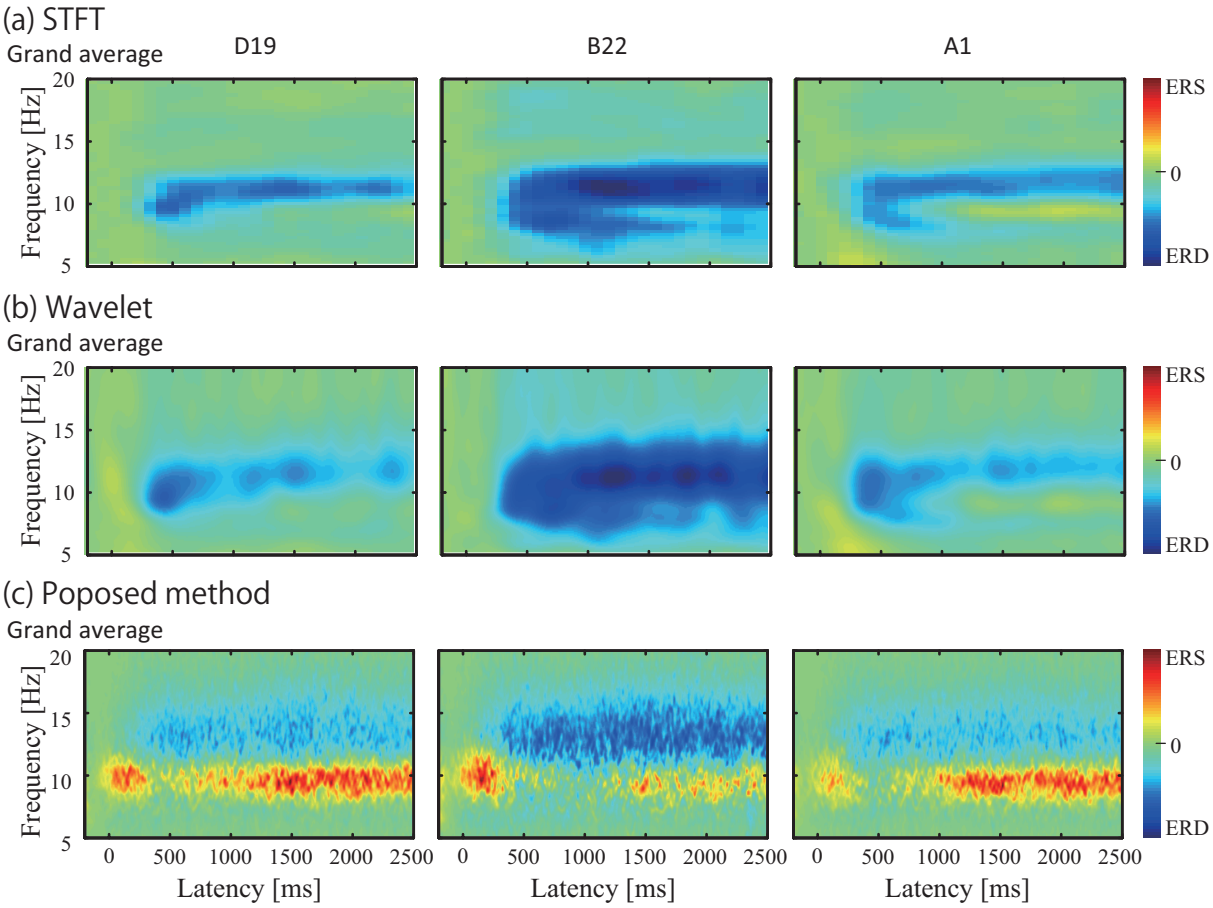

Figure 5.7: Comparison of the proposed method with the short time Fourier and wavelet analyses for EEGs of the grand averaged spectrum. (a) The STFT spectrum, (b) the wavelet spectrum and (c) the Hilbert spectrum calculated by the proposed method. Color coding was normalized by the maximum intensity at B22 electrode.

from 10 Hz to 12 Hz shortly (0–250 ms) after the onset of the visual cue 'L'.

The trial-averaged STFT spectrum of EEG oscillations $\overline{X_n(t', f_k)}$ recorded at the three electrodes (D19, B22, and A1) obtained from all 5 subjects are shown in Figure 5.4. The trial-averaged wavelet spectrum of EEG oscillations $\overline{\hat{E}_n(t, f)}$ and those of the Hilbert spectrum of EEG oscillations $\overline{\hat{H}_n(t, f)}$ recorded at same data in Figure 5.4 are shown in Figures 5.5 and 5.6, respectively. While there are some differences between subjects in the energy distributions shown in Figures 5.4, 5.5 and 5.6, alpha rhythm suppressions (ERDs) during left wrist movement is observed in STFT, wavelet and Hilbert spectra. Figures 5.4 and 5.5 show that the alpha band ERD at about 250 ms after onset of the visual cue 'L' are more significant from STFT, wavelet and Hilbert spectra at B22, located above the contralateral right sensorimotor cortex, than those at D19 located above the ipsilateral left sensorimotor cortex. The alpha band ERD can also be seen not only at two electrodes located in the vicinity of the sensorimotor cortices

but also at A1, located above the parietal cortex, in all subjects except subject 2. The alpha band detected in Hilbert spectra is slightly shifted commonly to higher frequency to compare with that in both the STFT and wavelet spectra. Alpha rhythm increases (ERSs) can be observed for 1000–2500 ms after onset of the visual cue 'L' at all three electrodes in all subjects in Hilbert spectra, whereas they can be observed in only subjects 1 in both the STFT and wavelet spectra. These results indicate that the Hilbert spectrum of EEG oscillations calculated by the proposed method could separate and identify more precise energy distributions in adjacent frequency bands than both the STFT and wavelet spectra.

Interestingly, the alpha rhythm instantaneously increased like ERS shortly (0–250 ms) after the onset of the visual cue 'L'. This instantaneous alpha rhythm increase can be seen in all subjects in Hilbert spectra and in only subject 1 in both the STFT and wavelet spectra. However, in subject 1, both the STFT spectrum and the wavelet spectrum do not clearly illustrate this instantaneous power change in Figure 5.5 while the Hilbert spectrum captures the intrawave frequency modulation from 8 Hz to 12 Hz in Figure 5.6.

Figures 5.7(a), 5.7(b) and 5.7(c) show the grand averaged STFT spectrum, the wavelet spectrum and the Hilbert spectrum shown in Figure 5.4, 5.5 and 5.6, respectively. The alpha band ERD during left wrist movement can also be observed in the two grand averaged spectrum as well as in Figures 5.4, 5.5 and 5.6. In contrast, the Hilbert spectrum can clearly detect the alpha band ERS for 1000–2500 ms after onset of the visual cue 'L'. Furthermore the instantaneously increased alpha rhythm recorded at 0–250 ms can be detected in Hilbert spectrum as well.

5.7 Discussion

This study proposed a novel method to extract and visualize ERD/ERS within an alpha frequency band for multichannel recorded EEGs. The results obtained by applying the method to EEGs from 5 subjects during left wrist movement demonstrate that the proposed method works well in extracting the alpha band ERD/ERS and is capable of capturing precise features of the ERD/ERS that is difficult based on the conventional STFT spectrum and the wavelet spectrum. A major difference between the proposed method and both the short time Fourier and wavelet analyses is that MEMD used by the proposed method aligns common modes present across multiple channels in same-index IMFs which allows the time–frequency features among different channels to be compared with standard EMD, the short time Fourier analysis and the wavelet analysis [8].

There are a lot of studies to analyze EEGs by the combination of EMD or MEMD and the Hilbert transform. However, few study visualized time–frequency energy distributions of the Hilbert spectrum in spite of that high time–frequency resolution. For example, Chang et al. [4] analyzed beta band ERS/ERD by using MEMD and the Hilbert transform, however, they employed the conventional Fourier spectrum to compare the power spectrum of IMF of

reference period with that of task period. Because the Hilbert spectrum is unable to detect the power changes within fixed frequency bands between reference and task periods in the same way as in done for the Fourier based spectrum, we directly subtract baseline amplitude from the entire amplitude as Equation (5.5) for each IMF to extract and visualize ERS/ERD in time–frequency map in a way comparable to the wavelet spectrum. This concept is along with the definition that IMF represents the oscillation mode imbedded in the data and not restricted to a narrow band signal, and can be modulated both for amplitude and frequency [3]. Therefore, the proposed method can clearly capture simultaneous ERD and ERS in time–frequency map.

In this experiment, subjects were instructed to move their left wrist, thus the contralateral dominant alpha band ERD should be observed [6] and the STFT spectrum, the wavelet spectrum and the Hilbert spectrum calculated by the proposed method can extract the contralateral alpha band ERD. In addition, the alpha band ERS recorded at electrode D19 at between about 1000–2500 ms after onset of the visual cue 'L' could be seen in the Hilbert spectrum. Such ipsilateral ERS was interpreted as a correlate of deactivated or actively inhibited motor area neurons by Pfurtscheller and Neuper [9]. However, both the STFT spectrum and the wavelet spectrum were scarcely able to detect the ipsilateral ERS. The proposed method revealed the alpha band ERS at between 1000–2500 ms after onset of the visual cue 'L' at not only the ipsilateral D19 but also the central A1 for all subjects, as shown in Figure 5.6, and in grand averaged Hilbert spectrum shown in Figure 5.7. Pfurtscheller and Lopes da Silva [6] also reported that these parietal cortex alpha band ERS were simultaneously recorded with ERD in the hand area sensorimotor cortex during voluntary hand movement and could be interpreted as a correlate of deactivated or actively inhibited motor area neurons.

By comparison with the STFT and wavelet spectra, the sharpness of the Hilbert spectrum is evident in that it can track minute variations of the energy and frequency. Indeed, the grand averaged wavelet spectrum could not extract instantaneous power changes like ERS shortly (0–250 ms) after the onset of the visual cue 'L' while the Hilbert spectrum can illustrate these frequency fluctuations, as shown in Figures 5.4, 5.5, 5.6 and 5.7.

One of the reasons such differences occurred among the three algorithms is the difference of their temporal and frequency resolutions. The time-frequency resolutions of the STFT and wavelet spectra are measured in the mean squares sense and are represented as the Heisenberg box of side lengths $2\delta_t$ by $2\delta_f$ [10, 11]. δ_t and δ_f are the time resolution and the frequency resolution, respectively. They are defined by the following functions [10, 12].

$$\delta_t^2 = \frac{\int_{-\infty}^{\infty} i_t^2 w^2(i_t)\mathrm{d}i_t}{\int_{-\infty}^{\infty} w^2(i_t)\mathrm{d}i_t}, \quad \delta_f^2 = \frac{\int_{-\infty}^{\infty} f_k^2 W^2(f_k)\mathrm{d}f_k}{\int_{-\infty}^{\infty} W^2(f_k)\mathrm{d}f_k}, \tag{5.15}$$

where $W(f_k)$ is the Fourier transform of $w(i_t)$. The product $\delta_t\delta_f$ must be greater than or equal to $1/4\pi$ due to the uncertainty principle. For a detailed STFT spectrum using the Gaussian function, $\delta_t = \sigma/\sqrt{2}$ and $\delta_f = \sqrt{2}/4\pi\sigma$. The STFT spectrum allows only a fixed time-frequency

resolution due to the constant length window function. As in the case of the STFT spectrum, in the wavelet spectrum, δ_t and δ_f could be calculated by the replacement i_t, f_k, $w(i_t)$ and $W(f_k)$ by t, f, $\psi(t)$ and $\Psi(f)$ in Equation (5.15), $\Psi(f)$ is the Fourier transform of $\psi(t)$. Temporal and frequency resolutions were variable for each scale and were defined by δ_t and δ_f, respectively. For a detailed wavelet transform using the Morlet wavelet, $\delta_t = \sigma_t/\sqrt{2}$ and $\delta_f = \sqrt{2}/4\pi\sigma_t$. Contrary to both the STFT and wavelet spectra, in the Hilbert spectrum, the time-frequency resolution is free from the uncertainty principle. Temporal resolution is equal to a sampling frequency. The frequency resolution depends on the total time [3] and is equal to $1/2.8 = 0.36$ Hz, 2.8 s is a total time at each trial.

As a result, it is difficult for both the STFT and wavelet spectra to exactly localize oscillatory events with high resolution in time and frequency. Meanwhile, the observed instantaneous event-related power increase seemed to be related to event-related potential, e.g. P300, which may reflect some cognitive process for visual cue 'L'. However, this must be the subject of in-depth consideration because numerous interpretations for ERS exist. For example, Klimesch et al. [13] strongly suggested that increased oscillatory alpha activity reflects an inhibition to retrieve stored motor memory traces.

However, there is a disadvantage that the proposed method requires the huge computation in MEMD. The computation complexity of MEMD depends on the characteristic of EEG time course, the stoppage criterion and the number of sets of direction vectors. In this study, each trial has 716 samples (2800 ms) and 30 channels for MEMD with $I = 512$ sets of direction vectors, and the computation of MEMD for each trial requires about 18.6 minutes on PC (Intel(R) Core(TM) i7–960 CPU @3.20 GHz 3.20 GHz, 6.00 GB RAM). Chang et al. [4] reported that the computation time of MEMD with $I = 64$ for each trial (7000 samples and 28 channels) was about 4.3 minutes on their PC (Intel(R) Core(TM) i7–2600 CPU @3.40 GHz 3.40 GHz, 3.00 GB RAM). Therefore, we recalculated the computation time of MEMD with $I = 64$ for each trial, and it took about 3.3 minutes. In spite of such a huge computation, increasing number of studies attempts to use MEMD in BCI [5, 14]. Both the number of samples and channels depend on recorded EEGs, fewer number of direction vectors could shorten computation time of MEMD, hence the number of direction vector should be assessed. However, there is few assessments of how many direction vectors is appropriate for the application of MEMD to EEGs. Moreover, recently, a few studies have tried to developed EMD-based algorithms on hardware platforms for online analyses [15, 16, 17]. Taken together, we believe that it is not very difficult to overcome a drawback of the longer computation time required in the present MEMD.

References

[1] Żygierewicz, J., Durka, P. J., Klekowicz, H., Franaszczuk, P. J., & Crone, N. E. (2005). Computationally efficient approaches to calculating significant ERD/ERS changes in the time–frequency plane. Journal of neuroscience methods, 145(1), 267–276.

[2] Herman, P., Prasad, G., McGinnity, T. M., & Coyle, D. (2008). Comparative analysis of spectral approaches to feature extraction for EEG-based motor imagery classification. Neural Systems and Rehabilitation Engineering, IEEE Transactions on, 16(4), 317–326.

[3] Huang, N. E., Shen, Z., Long, S. R., Wu, M. C., Shih, H. H., Zheng, Q., ... & Liu, H. H. (1998). The empirical mode decomposition and the Hilbert spectrum for nonlinear and non-stationary time series analysis. Proceedings of the Royal Society of London. Series A: Mathematical, Physical and Engineering Sciences, 454(1971), 903–995.

[4] Chang, H., Lee, P., Lo, M., Wu, Y., Wang, K., & Lan, G. (2013). Inter-Trial Analysis of Post-Movement Beta Activities in EEG Signals Using Multivariate Empirical Mode Decomposition. Neural Systems and Rehabilitation Engineering, IEEE Transactions on, 21(4), 607–615.

[5] Park, C., Looney, D., Rehman, N., Ahrabian, A., & Mandic, D. (2013). Classification of Motor Imagery BCI Using Multivariate Empirical Mode Decomposition. Neural Systems and Rehabilitation Engineering, IEEE Transactions on, 21(1), 10–22.

[6] Pfurtscheller, G., & Lopes da Silva, F. H. (1999). Event-related EEG/MEG synchronization and desynchronization: basic principles. Clinical neurophysiology, 110(11), 1842–1857.

[7] Rehman, N., & Mandic, D. P. (2010). Multivariate empirical mode decomposition. Proceedings of the Royal Society A: Mathematical, Physical and Engineering Science, 466(2117), 1291–1302.

[8] Rehman N., & Mandic, D. P. (2011). Filter bank property of multivariate empirical mode decomposition. Signal Processing, IEEE Transactions on, 59(5), 2421–2426.

[9] Pfurtscheller, G., & Neuper, C. (1997). Motor imagery activates primary sensorimotor area in humans. Neuroscience letters, 239(2), 65–68.

[10] Addison, P. S. (2002). The illustrated wavelet transform handbook: introductory theory and applications in science, engineering, medicine and finance. CRC Press.

[11] Tse, N. C., & Lai, L. L. (2007). Wavelet-based algorithm for signal analysis. EURASIP Journal on Applied Signal Processing, 2007(1), 169–169.

[12] Najmi, A. H., & Sadowsky, J. (1997). The continuous wavelet transform and variable resolution time–frequency analysis. Johns Hopkins APL Technical Digest, 18(1), 134–140.

[13] Klimesch, W., Sauseng, P., & Hanslmayr, S. (2007). EEG alpha oscillations: the inhibition–timing hypothesis. Brain research reviews, 53(1), 63–88.

[14] Bell, A. J., & Sejnowski, T. J. (1995). An information-maximization approach to blind separation and blind deconvolution. Neural computation, 7(6), 1129–1159.

[15] Pan, S. T., & Li, X. Y. (2012). An FPGA-based embedded robust speech recognition system designed by combining empirical mode decomposition and a genetic algorithm. Instrumentation and Measurement, IEEE Transactions on, 61(9), 2560–2572.

[16] Hong, Y. Y., & Bao, Y. Q. (2012). FPGA Implementation for Real-Time Empirical Mode Decomposition. Instrumentation and Measurement, IEEE Transactions on, 61(12), 3175–3184.

[17] Eftekhar, A., Toumazou, C., & Drakakis, E. M. (2013). Empirical Mode Decomposition: Real-Time Implementation and Applications. Journal of Signal Processing Systems, 73(1), 43–58.

Chapter 6

Clinical data application

There have been increased necessity for the signal and noise separation in clinical EEG studies so that this chapter focused attention on the EEG measurement, of schizophrenic patients (SZ). First, we applied the proposed ocular artifacts removal methods described in Chapter 3 to pseudo-EEGs consisting of the ideal artifacts-free EEGs and five types of ocular artifacts (an eye-blink and four eye-movements: up, down, left, and right) simulated by two equivalent current dipoles with a single-sphere head model (these pseudo-EEGs were not same as those described in Chapter 3) to assess the performance relative to an ocular artifacts removal method implemented in EEGLAB [1]. Secondly, the proposed method was applied to the EEGs recorded from 30 subjects (10 healthy controls; HC, 10 ultra high-risk psychosis; UHR and 10 first-episode schizophrenic patients; FES) during an auditory task and to demonstrate its feasibility for clinical application of schizophrenia severity. All clinical EEG data were measured by a doctor at the University of Tokyo Hospital.

6.1 Background

Recently, EEGs in the gamma band have been revealed to be sensitive to cortical circuit abnormalities in schizophrenia. Light et al. [2] suggested that chronic schizophrenic patients have frequency-specific deficits in the generation and maintenance of coherent synchronous neural oscillations in the gamma band that reflect a fundamental degradation of basic integrated neural network activity. In addition, Spencer [3] found that baseline 40Hz power at the left auditory cortex in SZ was higher than that in HC by using continuous click sound stimuli. However, there is no consensus view on deficits of the power in the gamma band for UHR and FES.

In EEG studies to reveal those gamma power deficits in schizophrenia, ocular artifacts should be removed because the amplitude of EEGs in gamma band is much smaller than those of the artifacts. Therefore, various removal methods have been proposed [3, 4, 5] including the one with ICA used in EEGLAB [1], which is a popular open source toolbox of EEG analysis. However, there is a possibility that those previous removal methods remove some information

of ideal EEGs together with ocular artifacts as I have pointed out in Chapter 3.

6.2 EEG measurement

6.2.1 Subjects

30 subjects (10 HC, 10 UHR, and 10 FES) participated in this experiment. This study was approved by the Ethics Committee of the University of Tokyo (approval No. 629-3, 2226-3), and informed consent was obtained from the subjects after they were given a complete explanation of the study. The UHR subjects and FES patients were recruited from the University of Tokyo Hospital. All subjects were between 15 and 40 years of age.

The Structured Interview for Prodromal Symptoms (SIPS) were used to select UHR subjects. Subjects who met criteria for attenuated psychotic symptoms (APS), brief intermittent psychotic symptoms (BIPS), and genetic risk and deterioration (GRD) were selected for the study [6, 7]. FES patients were diagnosed using DSM-IV [8] criteria, and were included in the present study if they demonstrated continuous psychotic symptoms within the past 24 months, without previously demonstrating psychotic symptoms. Healthy control subjects were screened with the Mini-International Neuropsychiatric Interview [9] to rule out psychiatric disorders. Healthy subjects were excluded from the study if they had a history of psychiatric illness, or a history of axis I disorders in their first-degree relatives.

For all subjects, the exclusion criteria were as follows: 1) neurological illness at any point in their lifetime, 2) traumatic brain injury with any cognitive consequences or loss of consciousness for more than 5 min, 3) a history of electroconvulsive therapy, 4) low estimated premorbid intelligence quotient (IQ) (below 70), and 5) previous alcohol abuse or addiction. Prior to entering the study, we confirmed that all participants could detect 1000 Hz tones at 30 dB using the audiometric testing. No difference was observed among the 3 groups in sex ratio, age, and estimated IQ, as measured with the Japanese version of the National Adult Reading Test [10].

6.2.2 Experimental paradigm

The subjects sat in a comfortable chair in a quiet shielded room (Figure 6.1) and were instructed to relax with their eyes opened. EEGs were recorded from 64 locations (extended 10–20 system, see Figure 6.2) using the Geodesic Sensor Net (Electrical Geodesics Inc., the U.S.) and sampled at 250 Hz. Locations of the 64 electrodes, a referenced to the vertex and a grounded to a right ear lobe. The electrode impedances were kept below 50 kΩ. The data were sampled at 250 Hz using a system acquisition filter (0.1–100 Hz). Note that, five electrodes (♯23, ♯35, ♯59, ♯63 and ♯64 shown in Figure 6.2) were removed from the following analysis because these contained large noises that were not ocular artifacts in most subjects.

The ASSR (auditory steady state response) paradigm [2, 11] were used in each subject

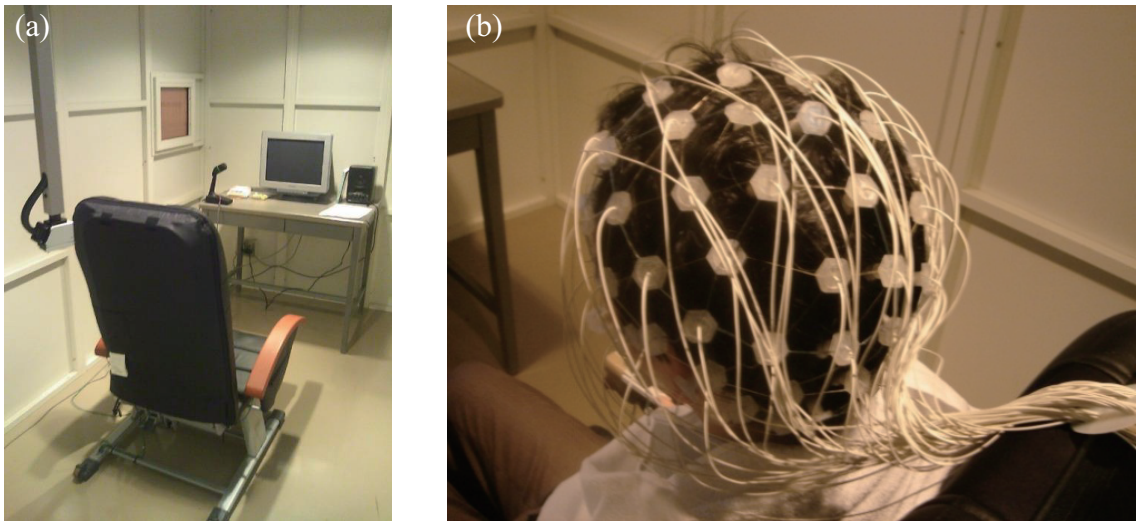

Figure 6.1: Condition of EEG measurement. (a) experiment environment, (b) Geodesic Sensor Net.

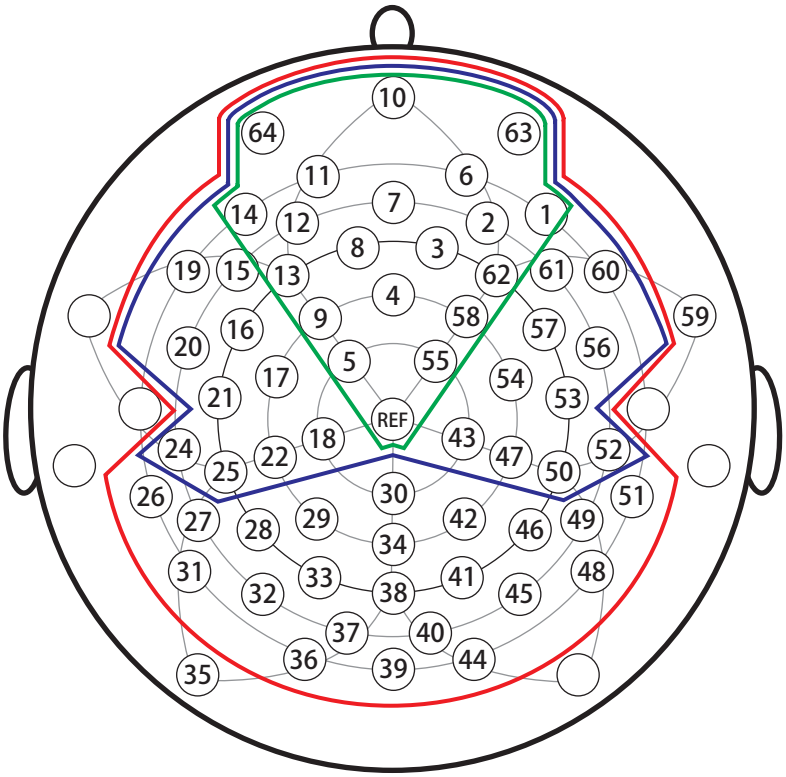

Figure 6.2: 64-channel EEG electrode locations on a scalp (top view): Red, blue and green solid lines indicate the scopes of 59-ch, 31-ch and 21-ch, respectively.

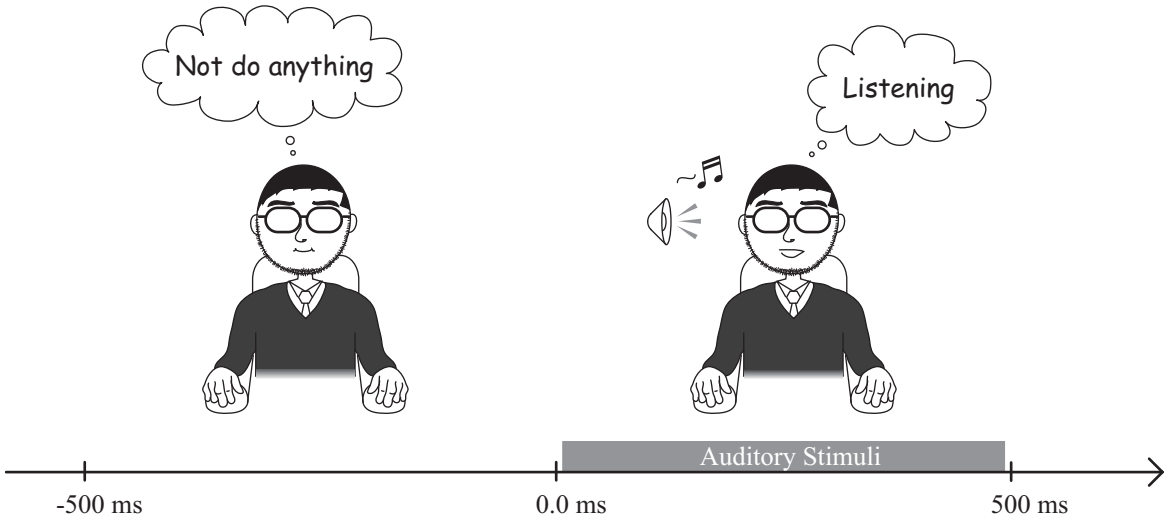

Figure 6.3: ASSR paradigm.

(Figure 6.3). Subjects received auditory stimuli presented binaurally through inserted earphones (Multi Trigger System, Medical Try System, Tokyo, Japan). The auditory stimuli were click sounds (80 dB, 1 ms) presented in 500 ms trains at 20 Hz, 30 Hz, and 40 Hz. The click sound trains were presented at each of these frequencies in a single block containing 200 trains, and each subject was presented with 3 blocks. The intertrain interval was 500 ms.

6.3 Application to pseudo-EEG

To compare the performance of the proposed method with the conventional ICA based removal method in EEGLAB (here, termed EL-ICA), we made pseudo-EEGs consisting of the ideal artifacts-free EEGs recorded from a subject and five types of simulated ocular artifacts (an eyeblink and four eye-movements: up, down, left, and right). In addition, we used three types of data which differed in the number of electrodes (59-ch, 31-ch and 21-ch shown in Figure 6.2). As evaluation indexes, we employed not only CC and RMSE of waveforms (described in Chapter 3) but also RMSE of power spectrum in the gamma band.

6.3.1 Creation of pseudo-EEGs with ocular artifacts

First, we prepared the same five dipole sets with a single-sphere head model and same five types of templates for five types of ocular activities: ‘Blink,’ ‘Up,’ ‘Down,’ ‘Left,’ and ‘Right’ as described in 3.3.4. Then, we calculated the five sets of 59-ch (inside of a red solid line in Figure 6.2) scalp potentials for a 2.0 s duration: $\mathbf{V}_{\mathrm{EYE}}(t)$ [‘Blink:’ $\mathbf{V}_{\mathrm{BL}}(t)$; ‘Up:’ $\mathbf{V}_{\mathrm{UP}}(t)$; ‘Down:’ $\mathbf{V}_{\mathrm{DO}}(t)$; ‘Left:’ $\mathbf{V}_{\mathrm{LE}}(t)$; ‘Right:’ $\mathbf{V}_{\mathrm{RI}}(t)$] was obtained from the five dipole sets by

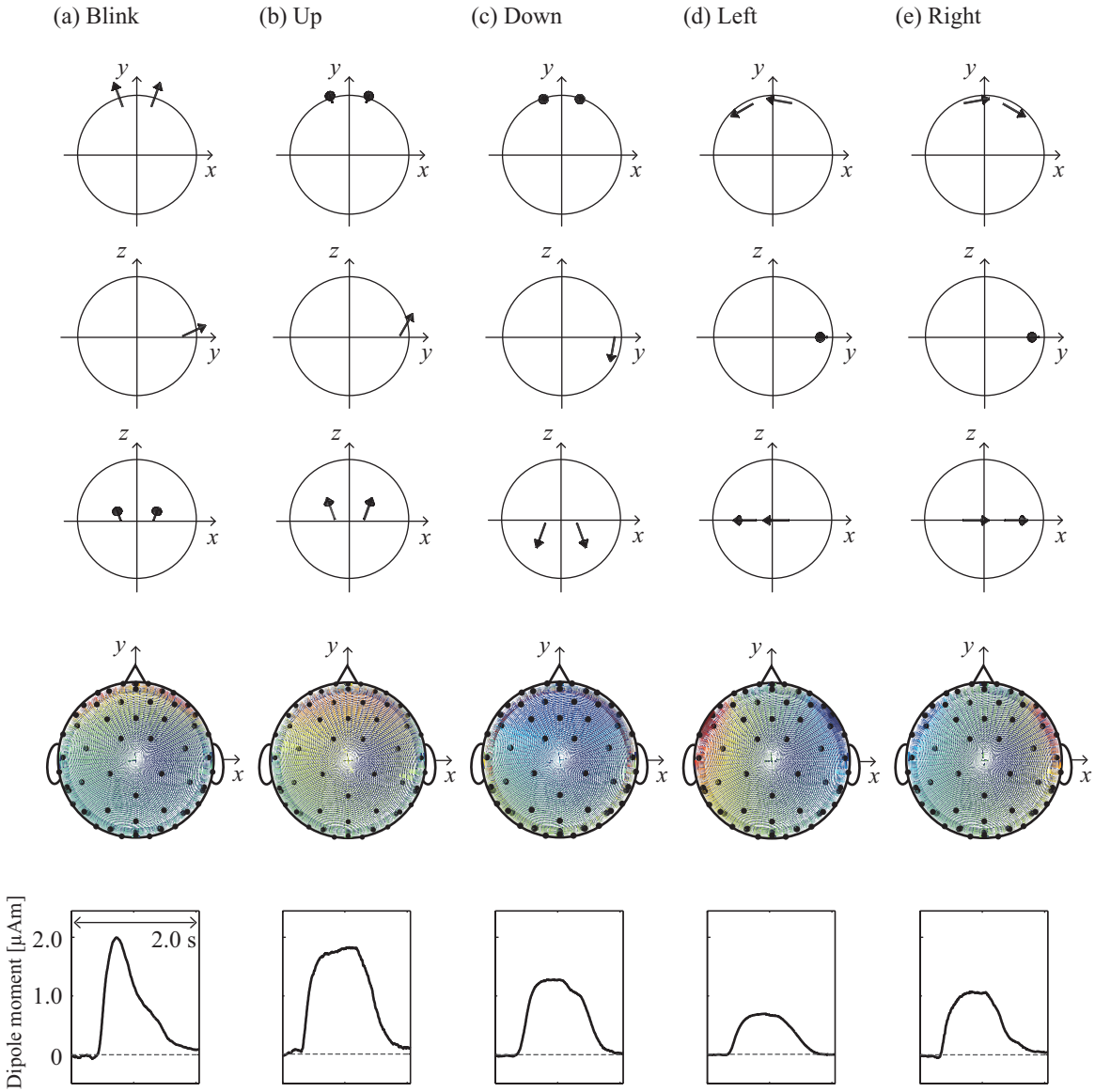

Figure 6.4: Locations of two dipoles, a single-sphere head model, and scalp distribution obtained by solving forward problems and template waveforms with 2 s duration for five types of ocular artifacts: (a) 'Blink,' (b) 'Up,' (c) 'Down,' (d) 'Left,' and (e) 'Right'.

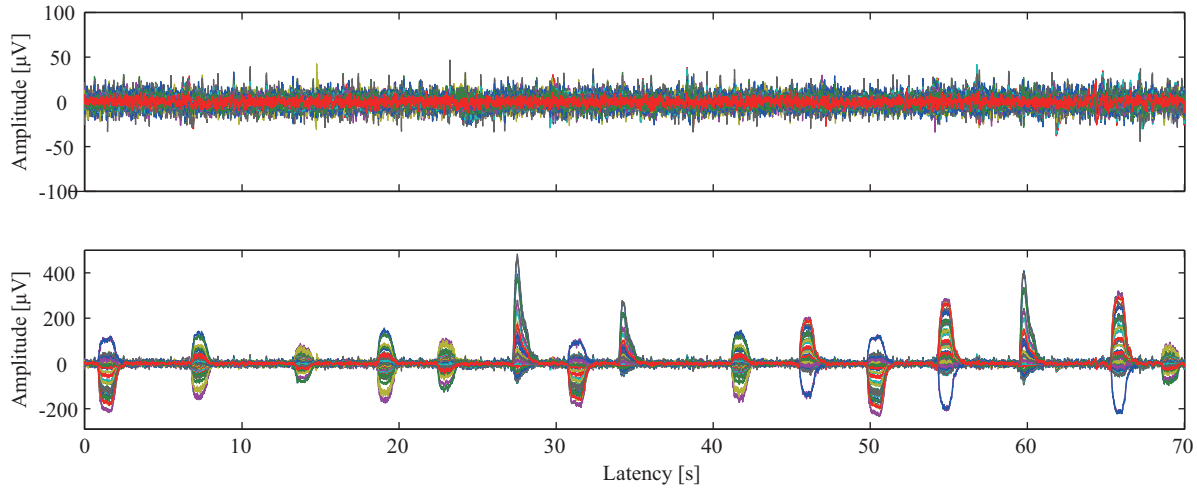

Figure 6.5: Superposition of representative waveforms of background 59-ch EEGs (Upper row) and of simulated 59-ch EEGs (Lower row).

solving forward problems. Distribution of the calculated scalp potentials are shown in Figure 6.4.

Next, ideal artifacts-free EEGs for duration 70.0 s (Figure 6.5) were extracted from EEGs recorded from one HC during the ASSR paradigm (40 Hz stimuli) described in 6.2.2 and digitally filtered with a zero-phase-shift band-pass from 0.5 Hz to 49 Hz. The filtered artifacts-free EEGs were denoted by $\mathbf{V}_{\mathrm{EEG}}(t)$. Fifteen $\mathbf{V}_{\mathrm{EYE}}(t)$ ($\mathbf{V}_{\mathrm{BL}}(t)\times 3$, $\mathbf{V}_{\mathrm{UP}}(t)\times 3$, $\mathbf{V}_{\mathrm{DO}}(t)\times 3$, $\mathbf{V}_{\mathrm{LE}}(t)\times 3$ and $\mathbf{V}_{\mathrm{RI}}(t)\times 3$) were superimposed onto $\mathbf{V}_{\mathrm{EEG}}(t)$ over a random period of time. ♯6 was a criterial electrode location of $\mathbf{V}_{\mathrm{BL}}(t)$, $\mathbf{V}_{\mathrm{UP}}(t)$, and $\mathbf{V}_{\mathrm{DO}}(t)$; ♯19 was that of $\mathbf{V}_{\mathrm{LE}}(t)$; and ♯60 was that of $\mathbf{V}_{\mathrm{RI}}(t)$. The peak amplitude of $\mathbf{V}_{\mathrm{EYE}}(t)$ was normally distributed with mean and standard deviation described in 3.3.4. Then, we prepared 70s long-term pseudo-EEGs $\mathbf{V}_{\mathrm{PSE}}(t)$ as shown in Figure 6.5. In addition, we prepared three types of data: Type i, 59-ch EEGs $\mathbf{V}_{\mathrm{PSE/i}}(t)$ inside of a red line; Type ii, 31-ch EEGs $\mathbf{V}_{\mathrm{PSE/ii}}(t)$ inside of a blue line; Type iii, 21-ch EEGs $\mathbf{V}_{\mathrm{PSE/iii}}(t)$ inside of a green line as shown in Figure 6.2. Finally, $\mathbf{V}_{\mathrm{EEG}/l}(t)$ and $\mathbf{V}_{\mathrm{PSE}/l}(t)$ (l refers to a type of data, i, ii or iii) were segmented to 70 trials EEGs, $\mathbf{V}^{m}_{\mathrm{EEG}/l}(t)$ and $\mathbf{V}^{m}_{\mathrm{PSE}/l}(t)$ ($m = 1, ..., M$, $M = 70$), with 1000 ms time interval from -500 to 500 ms following the onset of the stimulus.

6.3.2 Evaluation of removal methods

The proposed method and EL-ICA were applied to pseudo-EEGs. Note that there is a great difference between two methods; In EL-ICA, we applied ICA to pre-segmented EEGs $\mathbf{V}_{\mathrm{PSE}/l}(t)$. ICs accounting for ocular activities were visually identified and subtracted from $\mathbf{V}_{\mathrm{PSE}/l}(t)$ to calculate cleaned pre-segmented EEGs $\tilde{\mathbf{V}}_{\mathrm{PSE}/l}(t)$. Subsequently, $\tilde{\mathbf{V}}_{\mathrm{PSE}/l}(t)$ were segmented to 70 trials cleaned EEGs $\tilde{\mathbf{V}}^{m}_{\mathrm{PSE}/l}(t)$. In the proposed method, on the other hand, we applied ICA to segmented EEGs $\mathbf{V}^{m}_{\mathrm{PSE}/l}(t)$. ICs accounting for ocular activities were automatically identified in

each trial and $\tilde{\mathbf{V}}^m_{\mathrm{PSE}/l}(t)$ were calculated as described in 3.2.

In this validation, we focused mainly on the extent to which not only the true EEGs (mentioned in Chapter 3) but the true gamma oscillations were retained. For comparison of two methods, CC, RMSE of waveforms (RMSE-W) and RMSE of power spectrum (RMSE-P) in the gamma band were calculated at ♯4 (Figure 6.2) which located front-central region and represented maximal ASSR [11]. As same described in 3.3.5, RMSE-W and CC at ♯4 were given as

RMSE-W:

$$\psi^m_{\mathrm{W}/l} = \sqrt{\frac{1}{250}\sum_t \left(\tilde{v}^m_{\sharp 4\mathrm{P}/l}(t) - v^m_{\sharp 4\mathrm{E}/l}(t)\right)^2}, \tag{6.1}$$

where 250 is the number of samples among 1000 ms.

CC:

$$r^m_l = \frac{\sum_t \left(\tilde{v}^m_{\sharp 4\mathrm{P}/l}(t) - \overline{\tilde{v}^m_{\sharp 4\mathrm{P}/l}(t)}\right)\left(v^m_{\sharp 4\mathrm{E}/l}(t) - \overline{v^m_{\sharp 4\mathrm{E}/l}(t)}\right)}{\sqrt{\sum_t \left(\tilde{v}^m_{\sharp 4\mathrm{P}/l}(t) - \overline{\tilde{v}^m_{\sharp 4\mathrm{P}/l}(t)}\right)^2}\sqrt{\sum_t \left(v^m_{\sharp 4\mathrm{E}/l}(t) - \overline{v^m_{\sharp 4\mathrm{E}/l}(t)}\right)^2}}, \tag{6.2}$$

where $v^m_{\sharp 4\mathrm{E}/l}(t)$ and $\tilde{v}^m_{\sharp 4\mathrm{P}/l}(t)$ denote the scalp potential at the ♯4 of $\mathbf{V}^m_{\mathrm{EEG}/l}(t)$ and $\tilde{\mathbf{V}}^m_{\mathrm{PSE}/l}(t)$ each other, the overbar represents the trial average. The fast Fourier-transformation (FFT) using a Hamming window was applied to $v^m_{\sharp 4\mathrm{E}/l}(t)$ and $\tilde{v}^m_{\sharp 4\mathrm{P}/l}(t)$, and these power spectra (0.98 Hz frequency resolution) were calculated as $e^m_{\sharp 4\mathrm{E}/l}(f)$ and $\tilde{e}^m_{\sharp 4\mathrm{P}/l}(f)$ respectively. RMSE-P in 36 Hz – 45Hz at ♯4 were given as

RMSE-P:

$$\psi^m_{\mathrm{P}/l} = \sqrt{\frac{1}{10}\sum_{f\in 36-45Hz} \left(\tilde{e}^m_{\sharp 4\mathrm{P}/l}(f) - e^m_{\sharp 4\mathrm{E}/l}(f)\right)^2}, \tag{6.3}$$

where 10 is the number of samples among 36–45 Hz. As a result, 210 pairs of CC and two RMSEs (70 trials $\times$ 3 types of data) were calculated. Distributions of CC, and two RMSEs obtained by the proposed method were compared to those obtained by EL-ICA using the Wilcoxon signed-rank test because CC and RMSEs did not have Gaussian distributions. Furthermore, within each method, the three data types (i, ii, and iii) were compared using the Kruskal-Wallis test. Additionally, post hoc pairwise tests were performed using the Tukey's Honestly Significant Difference (Tukey's HSD) method to adjust for multiple comparisons. Note that A higher CC and lower RMSEs indicate better estimations of ideal EEGs.

6.4 Application to measured EEG

We applied the proposed methods described in Chapter 3 to measured EEG data from 30 subjects during ASSR paradigm described in 6.2.2. Furthermore, time/frequency inter-trial coherence (ITC) analyses were performed to assess ITC of the stimulus-driven EEG signals.

6.4.1 EEG pre-processing

First, the recorded EEGs in 6.2 were re-referenced to the left mastoid and digitally filtered with a zero-phase-shift band-pass from 0.5 Hz to 100 Hz and a 50 Hz notch filter. Subsequently, the filtered EEGs were segmented as epochs using a 2000 ms time interval from −1000 ms to 1000 ms, relative to the stimulus onset. Finally, totally 200 trials were available in each subjects.

6.4.2 Application of the proposed method

The proposed method was applied to all 200 trials in each subject. Afterward, trials exceeding ±100 μV at frontal electrodes were rejected. In addition, time/frequency ITC analyses were carried out to assess ITC of the stimulus-driven EEG signals [1, 12]. ITC is a frequency domain measure of the partial or exact synchronization of activity at a particular latency and frequency to a set of experimental events to which EEG data trials are time locked. The normalized complex time-varying energy at ♯4 is defined by

$$P = \frac{1}{M} \sum_{m=1}^{M} \frac{\psi(t, f) * v_{\sharp 4}^{m}(t)}{|\psi(t, f) * v_{\sharp 4}^{m}(t)|} \tag{6.4}$$

where $\psi(t, f)$ is a complex wavelet and we employed a complex Morlet wavelet described in 2.3.2. P is a complex value related to the phase distribution of each time–frequency region around t and f and its modulus is the phase-locking factor. It ranges from 0 (purely nonphase-locked activity) to 1 (strictly phase-locked activity). In addition, post hoc pairwise tests were performed using the two-sample t-test to comparisons among three group of patients.

6.5 Results

6.5.1 Pseudo-EEG

Density distributions of RMSE-W–CC pairs were visualized by RMSE-W–CC plots for three different data types and two different removals methods in Figure 6.6. Density distributions of RMSE-W–CC pairs obtained by EL-ICA appeared to spread more widely, and worse than that obtained by the proposed method at all three data types. On the other hand, density distributions of RMSE-W–CC pairs obtained by the proposed method appeared to be well localized at near zero of RMSE-W values and 1.0 of CC values although there were some outliers. The results of

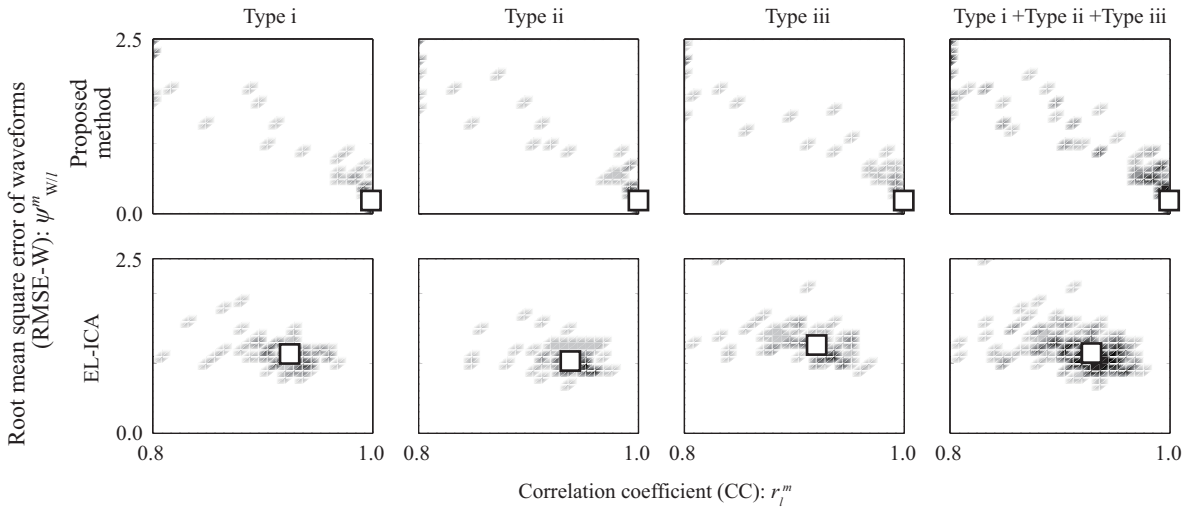

Figure 6.6: Density distributions of RMSE-W–CC pairs for three types of dataset (Type i, ii and iii) and two different removal methods. Density is represented by darkness and an open square indicates median value in each plot.

Table 6.1: p-values of Wilcoxon test comparing CC and RMSE-W of the proposed method with EL-ICA.

	Type i	Type ii	Type iii	Type i + Type ii + Type iii
CC	*	0.004	*	*
RMSE-W	*	*	*	*

* the significance with $p < 0.001$.

the Wilcoxon signed-rank test (p-value) of RMSE-W and CC for three different data types are shown in Table 6.1 and showed that the performance of the proposed method was significantly better than that of EL-ICA. The asterisks mean significant differences with $p < 0.001$.

When the channel number differences of RMSE-W and CC were examined for the proposed method and EL-ICA by using the Kruskal-Wallis test, a significant difference was found for three different data types within EL-ICA (RMSE-W; $\chi^2 = 37.86$, $p < 0.001$, CC; $\chi^2 = 22.75$, $p < 0.001$), whereas no significant difference was found within the proposed method. Figure 6.7 (a) and (b) illustrated the RMSE-W and CC obtained by the proposed method and EL-ICA for the different three data types based on boxplots. The Tukey's HSD method indicated that RMSE-W obtained by EL-ICA for data Types ii and iii were significantly smaller ($p < 0.001$) than that for data Type i (Figure 6.7 (a)), and CC obtained by EL-ICA for data Type ii were significantly larger ($p < 0.001$) than that for data Types i and iii (Figure 6.7 (b)).

Figure 6.8 (a) illustrated the RMSE-P and CC obtained by the proposed method and EL-ICA for the mixed all three data types on boxplots, and showed that RMSE-P was also significantly

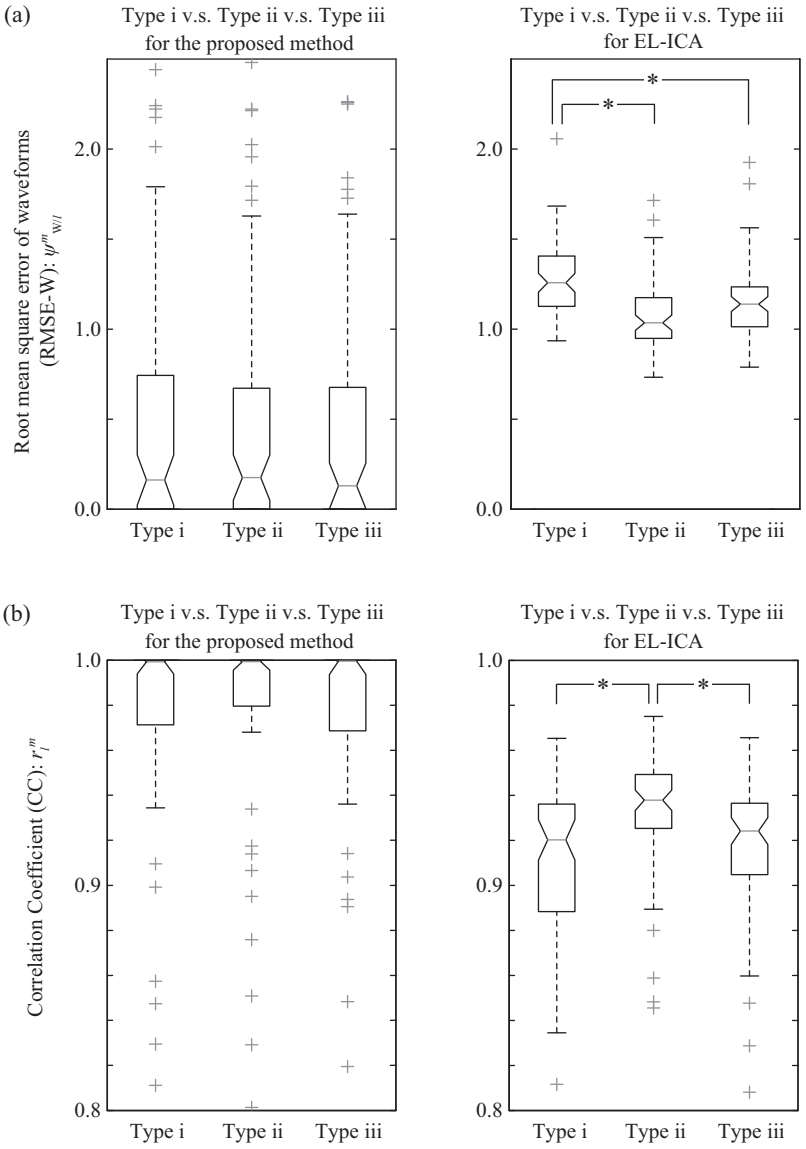

Figure 6.7: The RMSE-W and CC obtained by the proposed method and EL-ICA. (a) RMSE-W. (b) CC. On each box, the central mark is the median, the edges of the box are the 25th and 75th percentiles, the whiskers extend to the most extreme data points not considered outliers, and outliers are plotted by gray marks '+'. * indicates the significance with $p < 0.001$.

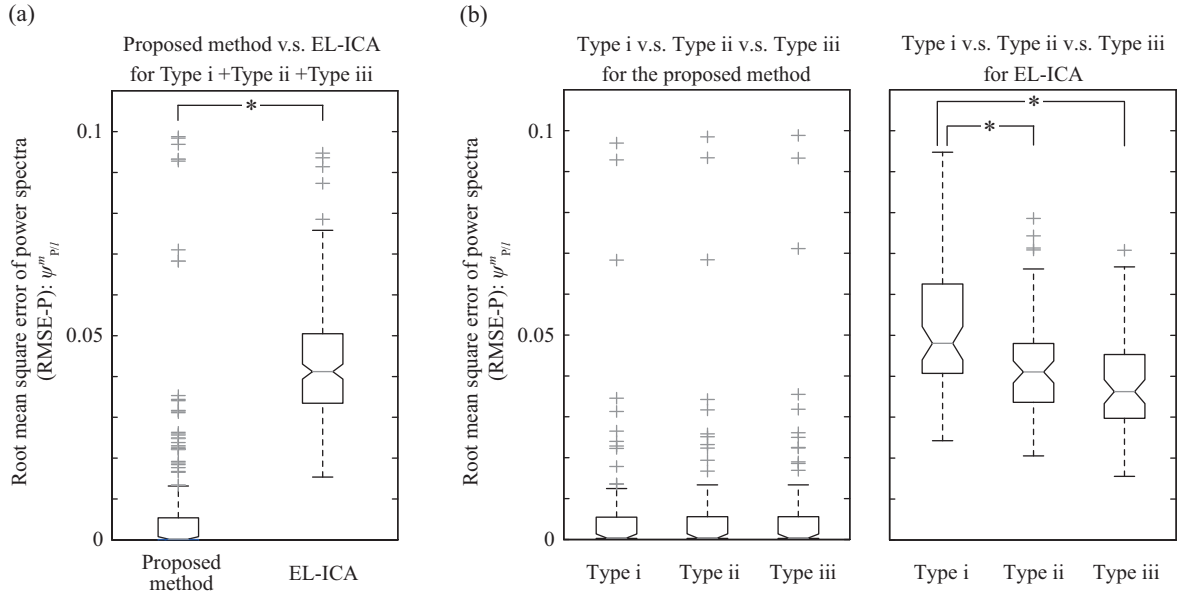

Figure 6.8: The RMSE-P obtained by the proposed method and EL-ICA. On each box, the central mark is the median, the edges of the box are the 25th and 75th percentiles, the whiskers extend to the most extreme data points not considered outliers, and outliers are plotted by gray marks '+'. * the significance with $p < 0.001$.

difference, $p < 0.001$, between the proposed method (mean = 0.008, std = 0.020) and EL-ICA (mean = 0.046, std = 0.016) by the Wilcoxon signed-rank test. The asterisks indicate significant differences with $p < 0.001$. Moreover, Figure 6.8 (b) showed RMSE-P obtained by the proposed method and EL-ICA for the different three different data types on boxplots as with Figure 6.7. The Kruskal-Wallis test showed that a significant difference was found for three different data types within EL-ICA ($\chi^2 = 29.17$, $p < 0.001$) whereas no significant difference was found within the proposed method. The Tukey's HSD method indicated that RMSE-P obtained by EL-ICA for data Types ii and iii were significantly smaller ($p < 0.001$) than that for data Type i (Figure 6.8 (b)) in common with RMSE-W in Figure 6.7 (a).

6.5.2 Measured EEG

After application of the proposed ocular artifacts removal method to measured EEGs, the mean number of analyzable trials (not exceeding ±100 μV at frontal electrode) among 30 subjects was 195.2 trials (min: 179, max: 200). Because before this removal process the mean number of analyzable trials among 30 subjects is 106.0 trials (min: 1, max: 195), the proposed method seemed to remove ocular artifacts effectively. Fig. 6.9 (a) shows a representative successful example of the artifact removal. However, a few trials were not analyzable and Fig. 6.9 (b) shows a failed example of removal. These trials clearly included artifacts with high frequency

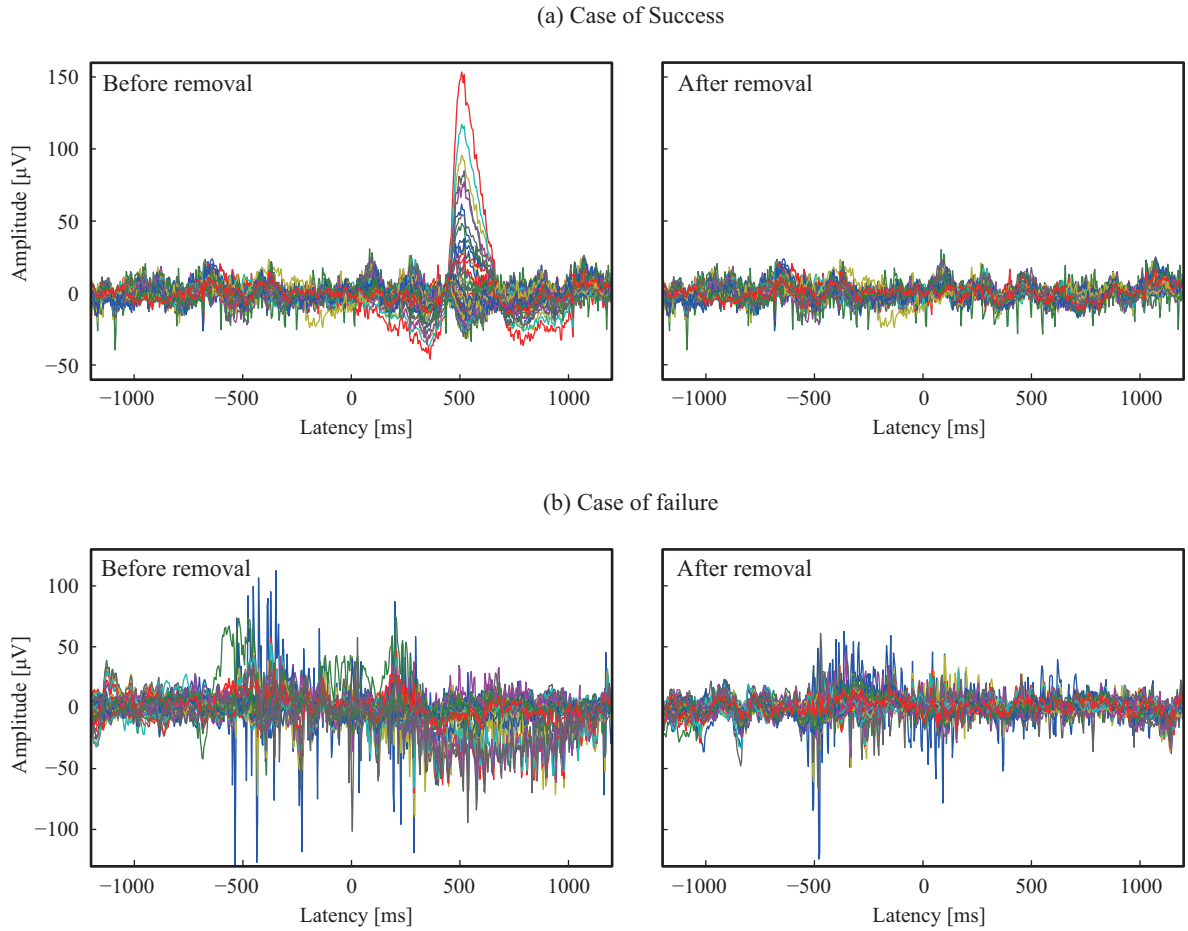

Figure 6.9: Measurement EEG waveforms, for all 59 channels, containing ocular artifacts and to which the proposed removal method is applied. (a) A successful example of removal, and (b) a failed example of removal.

activities like muscle activities and the artifacts mainly occurred around eyes. These artifacts might be elicited by squeezing his or her eyes shut. Nonetheless, as a results, we could acquire 179 trials for all subjects by using the proposed method, assuming that most ocular artifacts are something like the template waveforms with relatively low frequency shown in Fig 6.4.

Fig. 6.10 shows the subject-averaged time–frequency phase-locking factor at ♯4 in three groups of patients ((a) HC, (b) UHR and (c) FES), and Fig. 6.11 shows the results from the two-sample *t*-test ((a) HC v.s. UHR, (b) HC v.s. FES, and (c) UHR v.s. FES) at ♯4. In the time–frequency distribution of statistical results, the extents of gray and black color indicate significantly difference $p < 0.05$ and $p < 0.01$, respectively, between two groups of patients. Across the 500 ms stimulation block, the time–frequency distributions of phase-locking factor are obviously different between HC and both UHR and FES. The two-sample *t*-test shows that the phase-locking factors, after a stimulation start, are significantly difference ($p < 0.01$) between HC and UHR in a frequency band higher than 45 Hz, and between HC and FES in

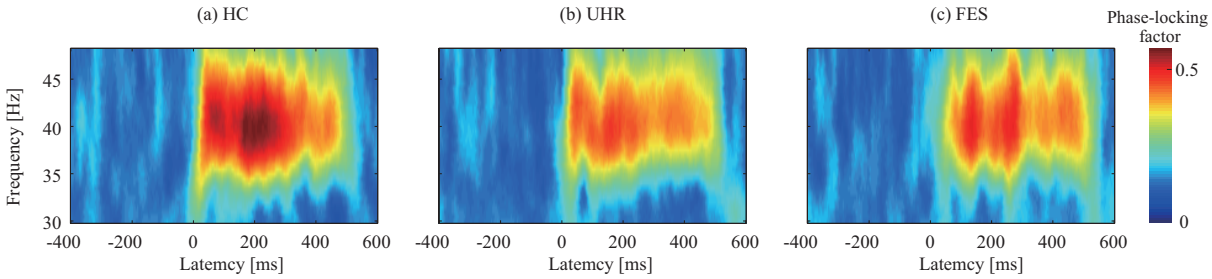

Figure 6.10: Time–frequency phase-locking factor in (a) HC, (b) UHR, and (c) FES averaged over all subjects.

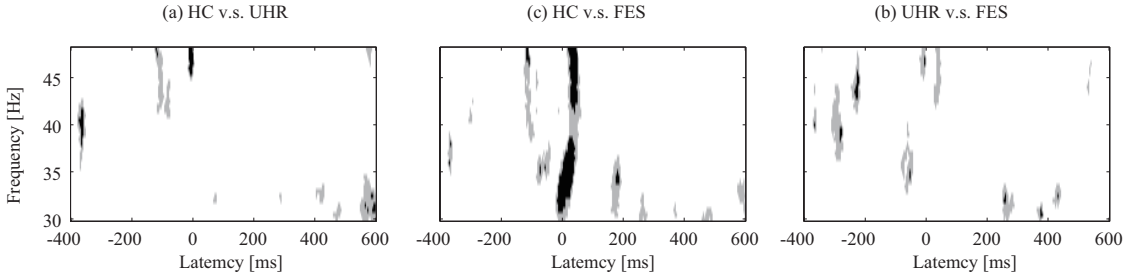

Figure 6.11: The results from the two-sample t-test to phase-locking factors between (a) HC and UHR, (b) HC and FES, and (c) UHR and FES. Areas drawn with gray and black indicate $p < 0.05$ and $p < 0.01$, respectively.

a frequency band higher than 30 Hz. Similarly, there is a significantly difference ($p < 0.05$) between UHR and FES after the stimulation start in a frequency band higher than 42 Hz. In contrast, during the stimulation, there is few significance among patients in the gamma band. In baseline duration (-400 – 0 ms and 500 – 600 ms), the phase-locking factors around 40 Hz approximately 100 ms prior to the stimulation start are significantly difference ($p < 0.05$) between HC and UHR, and between HC and FES, and the time–frequency distributions of both differences are similar. In addition, several gamma band activities differ significantly between HC and UHR, and between UHR and FES.

6.6 Discussion

In this study, first, we again applied the proposed ocular artifacts removal method to simulated EEGs with ocular artifacts following Chapter 3 to compare the performance with EL-ICA. Because we have applied EL-ICA to clinical EEGs before a segmentation process, non-segmented pseudo-EEGs different from those in Chapter 3 were needed for the comparison. In addition, we employed a new criteria, RMSE-P, to assess the performance of the removal methods in frequency domain how the gamma band activities unrelated to ocular artifacts were retained

in the removal process. In Figure 6.6, density distributions of RMSE-W–CC pairs argued that the proposed method retained more ideal EEGs than EL-ICA. This result was reasonable because EL-ICA was basically similar to ICA-only which is used in Chapter 3. Although EL-ICA applied ICA to non-segmented EEGs while ICA-only applied ICA to segmented EEGs, both methods likewise subtracted identified ICs reflecting ocular artifacts from original EEGs. Figure 6.8 (a) also confirmed superiority of the proposed method relative to EL-ICA in terms of retention of the gamma band activities.

Considering results for these EEG data with different EEGs of the number of channels, it was very interesting that the performance of EL-ICA in CC and RMSE-W was sensitive to the number of channels and was the best by using data Type ii (31 channels) whereas the best performance in RMSE-P was by using data Type iii (21 channels). The cause of these results were considered that CC and RMSE-W assessed the similarity and the coincidence between the two signal waves in time domain while RMSE-P assessed the coincidence between the two signal spectra in frequency domain. In addition, EL-ICA removed ocular artifacts without frequency information contrary to the proposed method. It is well known that the performance of ICA decomposition sometimes suffer from the overlearning [13, 14]. Therefore, CC and RMSE-W obtained by EL-ICA for data Type i (59-ch) were the worst among all data types because of the overlearning. By contrast, CC and RMSE-W obtained by EL-ICA for data Type iii (21-ch) seemed to be worse than those for data Type ii (31-ch) due to too few number of channels of data Type iii.

On the other hand, the proposed method kept the consistency of the performance in CC, RMSE-W and RMSE-P even if the number of channels changed. This was because we applied ICA after reducing the dimensions by applying PCA to EEGs to avoid overlearning. In addition, the proposed method could retain the gamma band activities because EMD embedded in the proposed method was available as a frequency filter [15], and the frequency of most prominent ocular artifacts was lower than the gamma band.

Next, we applied the proposed ocular artifacts removal method to the clinical EEGs recorded from HC, UHR and FES. The proposed method could remove ocular artifacts successfully and make almost all trials with ocular artifacts available to analyses. The results demonstrated that the proposed method perform well for not only simulated EEGs but also clinical EEGs. However, some artifacts having a relatively high frequency band were left in spite of the application of the proposed method. One of the reasons may due to the identification process of ocular-related IMFs in **Step 2** of the proposed method (Equation (3.4) described in 3.2). In this study, the multiplication factor u, which determines the upper limit of acceptable standard deviations in the classification of IMFs, is a rule-of-thumb value of 1.25 which is an efficient value for slow ocular artifacts such as template waveforms. However, a standard deviation of a signal with a constant and high frequency, e.g. a muscle artifact, is generally much smaller than that of a signal with a slow frequency and a prominent waveform, e.g. an eye-blink artifact. Therefore,

if we want to remove such signals with a constant and high frequency, we set the multiplication factor u lower value than 1.25. Because the lower value of u may remove noise-free EEGs, further consideration will be needed for it.

In addition, the ITC and statistical analysis were applied to the clinical EEGs, of which the proposed method removed ocular artifacts. Parts of the results obtained by the ITC analysis were consistent with those of a previous research [2] that the phase-locking factor just after starting stimulation in the gamma band was significantly different between HT and both UHR and FES. On the other hand, during the stimulation, there was few difference in the gamma band that was observed by Light et al. [2]. In a baseline period, we could not obtain clear power increase in SZ compared with HC in the gamma band reported by the previous study [3]. Nevertheless, a few power changes could be obtained in baseline. Therefore, for further study, the number of subjects should be increased and the number of channels for analyses should also to be increased to execute source analyses.

In this chapter, we compared the performance of the proposed method and EL-ICA, which we had employed for clinical EEGs, depending on variation in the number of channels. The number of channels is very important to clinical EEGs in practice because some occipital channels sometimes record noisy signals due to coming off a head during EEG recording. Moreover, doctors have to check and remove those channels with visual judgment for each recorded EEG. However, if the ocular artifacts removal method consistently demonstrates superior performance regardless of changing the number of channels, only a few frontal electrodes, e.g. 21-ch in data Type iii, are available for analyses with the removal method. In this chapter, we focused on a frontal channel (♯4) and the proposed method was certainly useful to analyze EEGs recorded from any number of channels.

References

[1] Delorme, A., & Makeig, S. (2004). EEGLAB: an open source toolbox for analysis of single-trial EEG dynamics including independent component analysis. Journal of neuroscience methods, 134(1), 9–21.

[2] Light, G. A., Hsu, J. L., Hsieh, M. H., Meyer-Gomes, K., Sprock, J., Swerdlow, N. R., & Braff, D. L. (2006). Gamma band oscillations reveal neural network cortical coherence dysfunction in schizophrenia patients. Biological psychiatry, 60(11), 1231–1240.

[3] Spencer, K. M. (2011). Baseline gamma power during auditory steady-state stimulation in schizophrenia. Frontiers in human neuroscience, 5, 1–7.

[4] Hong, L. E., Summerfelt, A., Mitchell, B. D., O'Donnell, P., & Thaker, G. K. (2012). A shared low-frequency oscillatory rhythm abnormality in resting and sensory gating in schizophrenia. Clinical Neurophysiology, 123(2), 285–292.

[5] Krishnan, G. P., Hetrick, W. P., Brenner, C. A., Shekhar, A., Steffen, A. N., & O'Donnell, B. F. (2009). Steady state and induced auditory gamma deficits in schizophrenia. Neuroimage, 47(4), 1711–1719.

[6] Miller, T. J., McGlashan, T. H., Woods, S. W., Stein, K., Driesen, N., Corcoran, C. M., ... & Davidson, L. (1999). Symptom assessment in schizophrenic prodromal states. Psychiatric Quarterly, 70(4), 273–287.

[7] Kobayashi, C., Glover, G. H., & Temple, E. (2007). Children's and adults' neural bases of verbal and nonverbal 'theory of mind'. Neuropsychologia, 45(7), 1522–1532.

[8] American Psychiatric Association, & American Psychiatric Association. Task Force on DSM-IV. (1994). Diagnostic and statistical manual of mental disorders: DSM-IV. Amer Psychiatric Pub Inc.

[9] Sheehan, D. V., Lecrubier, Y., Sheehan, K. H., Amorim, P., Janavs, J., Weiller, E., ... & Dunbar, G. C. (1998). The Mini-International Neuropsychiatric Interview (MINI): the development and validation of a structured diagnostic psychiatric interview for DSM-IV and ICD-10. Journal of clinical psychiatry, 59, 22–33.

[10] Matsuoka, K., Uno, M., Kasai, K., Koyama, K., & Kim, Y. (2006). Estimation of premorbid IQ in individuals with Alzheimer's disease using Japanese ideographic script (Kanji) compound words: Japanese version of National Adult Reading Test. Psychiatry and Clinical Neurosciences, 60(3), 332–339.

[11] Kwon, J. S., O'Donnell, B. F., Wallenstein, G. V., Greene, R. W., Hirayasu, Y., Nestor, P. G., ... & McCarley, R. W. (1999). Gamma frequency-range abnormalities to auditory stimulation in schizophrenia. Archives of General Psychiatry, 56(11), 1001–1005.

[12] Tallon-Baudry, C., Bertrand, O., Delpuech, C., & Pernier, J. (1996). Stimulus specificity of phase-locked and non-phase-locked 40 Hz visual responses in human. The Journal of Neuroscience, 16(13), 4240–4249.

[13] Vigário, R., Sarela, J., Jousmiki, V., Hamalainen, M., & Oja, E. (2000). Independent component approach to the analysis of EEG and MEG recordings. Biomedical Engineering, IEEE Transactions on, 47(5), 589–593.

[14] Särelä, J., & Vigário, R. (2003). Overlearning in marginal distribution-based ICA: analysis and solutions. The Journal of Machine Learning Research, 4, 1447–1469.

[15] Flandrin, P., Rilling, G., & Goncalves, P. (2004). Empirical mode decomposition as a filter bank. Signal Processing Letters, IEEE, 11(2), 112–114.

Chapter 7

Discussion

In Chapter 3, we set brain-derived (uncontaminated) EEGs and not-brain-derived artifacts as 'Signal' and 'Noise', respectively, and proposed a novel noise reduction method targeted to ocular artifacts. We focused mainly on the extent to which the true EEGs are retained and proposed a novel hybrid method, based on the combination of ICA, EMD, and the KF, to remove the ocular artifacts. The proposed removal method is clearly different from any previous methods based on ICA in terms of identifying an ocular duration and noise-free duration at each contaminated IC reflecting ocular artifacts (3.2: **Step 1**). Therefore, the proposed method could locally remove ocular artifacts and achieved the suppression of information loss from noise-free duration at contaminated ICs. In addition, we proposed a novel quantitative assessment method with a single-sphere head model, two ECDs representing two eyes and practically multichannel recorded EEGs to evaluate the performance of 'Signal' loss suppression and 'Noise' reduction. This assessment method demonstrated that the proposed method could provide better performance than the previous methods based on ICA for 'Signal' loss suppression and 'Noise' reduction.

There are two new ideas of the proposed removal method described in Chapter 3; 1) Separating contaminated ICs into artifacts-related parts and artifacts-free parts (3.2: **Step 1**), 2) Connecting cleaned artifacts-related parts and artifacts-free parts and, estimating cleaned contaminated ICs by using the KF (3.2: **Step 3**). These ideas enabled the proposed method to inhibit loss of interested EEGs associated with removal of ocular artifacts. Using these two ideas, in other words, it will be possible to inhibit loss of interested EEGs by using other signal processing methods instead of ICA, EMD, and the KF. For example, MEMD might be capable of substituting for the combination of ICA and EMD, and the particle filter might be alternative estimating method of the KF.

Next, we attempted to remove brain-derived background EEGs for multichannel ERP analysis in Chapter 4. Following Chapter 3, we focused on 'Signal' loss suppression and proposed a novel method combined PCA with MEMD to increase SNR of ERPs. The proposed method utilized only a priori knowledge of frequency band of background EEGs, whereas previous

methods required specific a priori knowledge obtained from trial-averaged ERPs, which may give misleading information to ERP analysis if the background EEGs were not suppressed by trial averaging. In addition, we employed the quantitative assessment method resembling that used in Chapter 3 in that it consisted of a single-sphere head model and ECDs. The proposed method was assessed by comparison of the previous multivariate methods aimed at increasing SNR of ERPs, and increased SNR higher than previous methods and had the best performance among them.

The general ideas of the proposed method mentioned in Chapter 4 was how to enhance ERP without losing its information. In other words, we attempted to highlight ERP by removing not-ERP-related components from EEGs according to the physiological frequency information of not-ERP-related components. In contrast, because most previous methods which tried to enhance ERP to extract ERP-related components from EEGs according to the arbitrarily-set information of ERP, their methods might fail to extract ERP. Nevertheless, unremoved artifacts could be suppressed by trial averaging, whereas unextracted ERP never comes back. In short, the proposed methods had the weak constraint for removing not-ERP-related components, but certainly retained ERP-related components. However, we confirmed that the proposed method worked well for P300. Thus, it is anxious about whether the proposed method could retain the other ERPs, e.g. N100 and P200, etc. by removing background EEGs. Therefore, it must be considered to employ not only frequency information but also spatial information for removing background EEGs.

In Chapters 3 and 4, we employed a single-sphere head model and two ECDs which was the simplest way for a quantitative assessment. Although we did not perform the source localization of EEGs, the proposed removal methods expected to contribute to pre-processing before the source localization. Therefore, it must be used a realistic head model [1, 2] to validate the proposed methods for source localization. Moreover, if a realistic head model is employed, we should take into account tissue conductivity anisotropy of head model because recent studies reported influence of tissue conductivity anisotropy for solving forward problems and inverse problems with realistic head model [2].

In Chapter 5, we described ‘Signal extraction’ method to increase SNR of interested EEGs, different from Chapters 3 and 4 where we have referred to ‘Noise reduction’. To extract and visualize multichannel recorded ERD and ERS within the alpha band related to a motor task, we proposed a hybrid method based on MEMD and HHT. The proposed method could extract and visualize more precise ERD and ERS than conventional Fourier based analysis because MEMD was free from the uncertainty principle. However, Chapter 4 examined the performance of the proposed method by using only practical multichannel recorded EEGs different from Chapters 3 and 4. If we want to use a head model and ECDs, there should be well-known source information of ‘Signal’ or ‘Noise’. As for EEG oscillations, source setting by using ECDs are difficult because there is no consensus view on source of not only alpha but also the

other oscillations. Nevertheless, the results of the proposed method to recorded EEGs showed higher time–frequency resolution than those of the conventional Fourier based methods. If the signal source of EEG oscillations were clarified in the future, the availability of the proposed method certainly to be confirmed by the realistic simulated model with realistic head model and ECDs representing these oscillations.

In Chapter 6, we applied the proposed removal method for ocular artifacts described in Chapter 3 to clinical recorded EEGs to increase the SNR of the gamma oscillations. Before that, we again compared the proposed method with the other popular removal method installed into EEGLAB (EL-ICA) by using the quantitative assessment methods in common with, but little difference from that used in Chapter 3. Since EL-ICA has been applied to a lot of clinical EEGs, not to mention schizophrenic EEGs, the comparison was necessary to confirm the utility of the proposed method for gamma band analysis. The assessment demonstrated that the proposed method could retain not only the waveforms but also the gamma oscillations than EL-ICA. Subsequently, we applied the proposed removal method to clinical EEGs recorded from 30 subjects (10 HC, 10 UHR, and 10 FES), and applied the ITC analysis to reveal differences in the gamma band among three groups. As a results, the proposed method could remove ocular artifacts for clinical EEGs as well as simulated EEGs. However, the results underscored the vulnerability of the proposed removal method for high frequency artifacts, e.g. muscle activities. Then, this is the future topics of discussion. The main objective of the ITC analysis is to obtain trial-by-trial synchronizations and we employed the WT to calculate phase-locking factors. However, it is difficult for the conventional WT to capture precise features of the EEG oscillations discussed in Chapter 5, thus MEMD used in Chapter 4 and Chapter 5 could be alternative approach to calculate more precise phase-locking factor.

References

[1] Kybic, J., Clerc, M., Faugeras, O., Keriven, R., & Papadopoulo, T. (2006). Generalized head models for MEG/EEG: boundary element method beyond nested volumes. Physics in medicine and biology, 51(5), 1333–1346.

[2] Wolters, C. H., Anwander, A., Tricoche, X., Weinstein, D., Koch, M. A., & MacLeod, R. S. (2006). Influence of tissue conductivity anisotropy on EEG/MEG field and return current computation in a realistic head model: a simulation and visualization study using high-resolution finite element modeling. NeuroImage, 30(3), 813-826.

Chapter 8

Conclusion

In this dissertation, we have proposed several novel methods to improve SNR of EEGs and dealt with variety of interested EEG ‘Signal’ and uninterested EEG ‘Noise’. The ‘Signal’ often influenced by the variety of ‘Noise’ because EEGs consist a mixture of an unknown number of neural and non-neural activations. Although there have been various methods to improve SNR of EEGs, most of previous methods focused attention on only ‘Noise’ reduction and rarely focused attention on ‘Signal’ loss. In clinical studies, however, it has been desired to reduce ‘Signal’ loss to extract biomarkers targeting brain diseases.

In Chapter 3, we proposed an innovative method to remove ocular artifacts. We believe that the idea of locally-restricted removal would be widely-accepted, and various removal methods based on this idea would be suggested in future studies for the removal of ocular artifacts.

In Chapter 4, we proposed a novel method to increase SNR of the ERP especially P300. The idea removing background EEGs was a helpful concept to enhance P300. The proposed method removed background EEGs for P300 according to the frequency difference between P300 and background EEGs.

In Chapter 5, we proposed an advanced method of MEMD for ERD and ERS extraction. Here, MEMD used in Chapters 4 and 5 was a novel method for signal decomposition, and little research employed MEMD for EEG analysis, in particular for extraction and visualization of EEG oscillations. While there have been some studies to extract ERPs by using MEMD, Chapter 5 described the first instance of the precise extraction of ERD and ERS by using MEMD. We believe that there will be strong demand of MEMD for various EEG analyses in the future.

In Chapter 6, we applied the proposed ocular artifacts removal methods described in Chapter 3 to clinical recorded EEGs. There has been the certain consistent approach for ‘Signal’ extraction and ‘Noise’ reduction. We should identify ‘Signal’ and/or ‘Noise’ by using only the physiological knowledge: In Chapter 3, we attempted to remove ocular artifacts along with the assumption that the prominent ocular artifacts should be independent with respect to uncontaminated EEGs and occur for only a limited time, i.e. not always occur. In Chapters 4 and 5, we employed frequency information to remove background EEGs and extract alpha oscillations

respectively.

This consecutive concept was based on my consistent belief, ‘Everything happens for a reason’. Both ‘Signal’ and ‘Noise’ which we defined in each chapter have their physiological origins, and they have certain reasons to appear in EEGs. In spite of the facts, a large number of EEG studies focusing on the singal noise separation seemed to have interests only in one side either in ‘Signal’ or ‘Noise’. They extracted ‘Signal’ (or removed ‘Noise’) by using an arbitrary assumption not based on the physiological knowledge. However, the approach may not be reliable because ‘Signal extraction’ and ‘Noise reduction’ are inextricably. In fact, the same alpha oscillations defined as ‘Noise’ in Chapter 4 is ‘Signal’ in Chapter 5.

The method proposed in this dissertation performed well for ‘Signal extraction’ or ‘Noise reduction’. The proposed artifacts removal methods for ocular artifacts and background EEGs focus attention on suppression of ‘Signal’ loss. They are useful for the future diagnosis and disease progression monitoring. The advanced signal extraction method for ERD and ERS of alpha oscillations is a pioneer method for precise extraction of EEG oscillations. In conclusion, I believe that the proposed concept about ‘Signal’ and ‘Noise’ mentioned above would be reflected in future EEG studies.

Publication List

Full papers

1. Kawaguchi, H., & Kobayashi, T. (2011). Localized removal method for eye-blink-related artifacts in electroencephalogram measurements (in Japanese). Transactions of the Japanese Society for Medical and Biological Engineering, 49(4), 551–557.

2. Kawaguchi, H., Kume, T., & Kobayashi, T. (2013). A background EEG removal method combining PCA with multivariate empirical mode decomposition for event-related potential measurements. IEEJ Transactions on Electrical and Electronic Engineering, 8(S-1), S53–S60.

3. Kawaguchi, H., & Kobayashi, T. (2014). A Method for Precise Extraction of EEG Rhythmic Activities using Multivariate Empirical Mode Decomposition and the Hilbert Transform. Neuroscience and Biomedical Engineering, Manuscript submitted for publication.

4. Kawaguchi, H., & Kobayashi, T. A locally restricted electroencephalogram ocular artifact removal method based on empirical mode decomposition with independent component analysis and Kalman filter. Medical and Biological Engineering and Computing. On peer review.

Proceedings (International conference)

1. Kawaguchi, H., Sasayama, T., Jung, J., Oida, T., & Kobayashi, T. (2009). Spatial Filtering of Steady-state Somatosensory Evoked Potentials toward the Development of Brain-machine Interface. Proceedings of 18^{th} International Congress on Brain Electromagnetic Topography, 175–178.

2. Kawaguchi, H., Kume, T., & Kobayashi, T. (2012). A Locally-Restricted Method for Removal of Eye-Blink Artifacts in Electroencephalogram Measurements. Proceedings of the 2012 International Conference on Complex Medical Engineering.

3. Okuahata, S, Kusanagi, T., Kawaguchi, H., & Kobayashi, T. (2012). Sequential Memory Scanning during Sternberg Memory Task Regardless of the Different Presentation Style. Proceedings of the 2012 International Conference on Complex Medical Engineering.

Proceedings (Domestic conference)

1. Kawaguchi, H., & Kobayashi, T. (2011). Attention quantification based on steady-state somatosensory evoked potentials. The Technical Report of The Proceeding of The Institute of Electronics, Information and Communication Engineers, 111, 77–80.

2. Kawaguchi, H., Kume, T., & Kobayashi, T. (2012). An identification and removal method of background EEG rhythms for event-related potential analyses. Proceedings of The 27^{th} Symposium on Biological and Physiological Engineering, 351–354.

3. Kawaguchi, H., Sasayama, T., Jung, J., Oida, T., & Kobayashi, T. (2009). Measurements and analyses of neural activities in the somatosensory cortex toward the development of BMI: An fMRI/EEG study (in Japanese). The Technical Report of The Proceeding of The Institute of Electronics, Information and Communication Engineers, 109, 51–56.

4. Kawaguchi, H., Sasayama, T., Hamada, S., & Kobayashi, T. (2010). Brain-computer interface based on steady-state somatosensory evoked potentials : A basic study by simulations and high-density EEG measurements (in Japanese). The Technical Report of The Proceeding of The Institute of Electronics, Information and Communication Engineers, 110, 39–44.

5. Sasayama, T., Iida, T., Kawaguchi, H., Hamada, S., & Kobayashi, T. (2010). A Prewhitening EEG Beamforming with Linear Constraint in a Realistic Head Model (in Japanese). The Technical Report of The Proceeding of The Institute of Electronics, Information and Communication Engineers, 110, 33–38.

6. Izuoka, D., Kawaguchi, H., Sasayama, T., & Kobayashi, T. (2011). Brain-computer interface based on steady-state visually evoked potentials : Fundamental study on classification of attended stimulus based on amplitude change (in Japanese). The Technical Report of The Proceeding of The Institute of Electronics, Information and Communication Engineers, 111, 91–96.

7. Izuoka, D., Kawaguchi, H., & Kobayashi, T. (2011). A fundamental study on coding of steady-state visually evoked potentials by stimuli with different luminance (in Japanese). The Technical Report of The Proceeding of The Institute of Electronics, Information and Communication Engineers, 111, 13–18.